FACULDADE DE ENGENHARIA DA UNIVERSIDADE DO PORTO

Auto-tuned, data-driven predictive controller for satellite-to-ground Free Space Optics Communication systems

Ana Margarida de Freitas

U.PORTO

FEUP FACULDADE DE ENGENHARIA UNIVERSIDADE DO PORTO

Master in Mechanical Engineering - Automation

Supervisor: Prof. Carlos Correia

Co-Supervisor: Prof. António Mendes Lopes

October 2, 2025

Auto-tuned, data-driven predictive controller for satellite-to-ground Free Space Optics Communication systems

Ana Margarida de Freitas

Master in Mechanical Engineering - Automation

October 2, 2025

Resumo

Comunicações Ópticas em Espaço Livre (FSOC) entre satélites em órbita terrestre baixa (LEO) e estações terrestres são altamente sensíveis à turbulência atmosférica, a qual degrada a qualidade da frente de onda e limita a taxa de transmissão de dados alcançável. Esta tese investiga estratégias de controlo preditivo no âmbito de controlo Linear Quadratic Gaussian (LQG), com o objetivo de mitigar distorções induzidas pela turbulência e manter ligações ópticas estáveis, possibilitando taxas de transmissão até 40 vezes superiores às das comunicações típicas por radiofrequência (RF).

É utilizado um modelo atmosférico simplificado apenas de fase, e os coeficientes dos modelos autorregressivos (AR e VAR) são estimados usando as equações de Yule-Walker, empregando o mesmo método de estimação tanto para os modelos AR quanto para os VAR. Um modelo de atmosfera com uma única camada é adotado nas simulações FSOC para avaliar o desempenho da correção da frente de onda e a qualidade do sinal óptico, considerando variações tanto nos parâmetros atmosféricos (ex.: velocidade e direção do vento, parâmetro de Fried) como nos parâmetros de hardware (ex.: frequência de amostragem do sistema AO).

Os resultados indicam que o VAR(2) oferece o melhor equilíbrio entre robustez e sensibilidade, uma vez que modelos de ordem superior proporcionariam apenas melhorias marginais na correção da frente de onda, tornando-se simultaneamente mais vulneráveis a discrepâncias na direção do vento. Em contraste, o aumento da frequência de amostragem melhora significativamente o Strehl Ratio (SR). Outros parâmetros de hardware têm um impacto negligenciável dentro de gamas viáveis.

Estas conclusões fornecem orientações práticas para o desenho e otimização de sistemas de AO preditivo em FSOC, destacando os compromissos entre complexidade do modelo, robustez e configuração de hardware. Além disso, sublinham os potenciais benefícios da extensão desta abordagem para modelos atmosféricos multicamada mais precisos, com vista a melhorias adicionais de desempenho.

Palavras-chave: AO, turbulência atmosférica, modelos AR, FSOC, satélite LEO, controlo preditivo, estimação Yule-Walker.

Abstract

Free-Space Optical Communication (FSOC) between low Earth orbit (LEO) satellites and ground stations is highly sensitive to atmospheric turbulence, which degrades wavefront quality and limits the achievable data rate. This thesis investigates predictive control strategies within the Linear Quadratic Gaussian (LQG) framework to mitigate turbulence-induced distortions and maintain stable optical links, enabling data rates up to 40× higher than typical radio frequency (RF) communications.

A simplified phase-only atmospheric model is employed, and the autoregressive (AR and VAR) models' coefficients are estimated using the Yule-Walker equations, using the same estimation method for both AR and VAR models. A single-layer model of the atmosphere is used in the FSOC simulations to evaluate wavefront correction performance and optical signal quality, considering variations in both atmospheric parameters (e.g., wind speed, direction and Fried's parameter) and hardware parameters (e.g., AO loop frequency).

Results indicate that VAR(2) offers the best balance between robustness and sensitivity, as higher-order models would provide only marginal improvements in wavefront correction while becoming increasingly vulnerable to mismatches in wind direction. In contrast, increasing the AO loop frequency significantly enhances the Strehl Ratio (SR). Other hardware parameters have a negligible impact within feasible ranges.

These findings provide practical guidance for the design and optimization of predictive AO systems in FSOC, highlighting the trade-offs between model complexity, robustness, and hardware configuration. They also underscore the potential benefits of extending the approach to more accurate multi-layer atmospheric models for further performance enhancement.

Keywords: AO, atmospheric turbulence, AR models, FSOC, LEO satellite, predictive control, Yule-Walker estimation.

Acknowledgements

First and foremost, I have to express my gratitude to those who have been by my side since day one, my best friends, my biggest fans, and those who inspire me every day in all senses of life, my parents — Graça Mariana and José Gregório. I couldn't be more grateful for the solid foundations you two are in my life. I hope you're proud. You are the reason I could pull through all the hard times and persevere to achieve this goal, thank you. To the rest of my family, for provoking my curiosity, believing in me, and for being the best role models I could have.

To the University of Porto, I'm glad that I got to pursue this degree in this great institution, with amazing professors and a universe of new experiences. Where I got to learn about engineering from the best in the field and discover my interests in the area. Thanks to FEUP, I was lucky enough to be part of BEST. An organization full of principles, goals, with a mission to accomplish in this faculty, to promote diversity, and give a voice to students. BEST taught me so much about myself and what I'm capable of — while giving me the best friends in the whole universe. I'm very grateful I saw that recruitment email, even before attending my first day of classes; it definitely opened the door to a whole new world. Nonetheless, for the chance of going in ERASMUS to Krakow — the other corner of Europe — for the sake of learning and meeting new cultures, and the chance to be part of *Universidade Júnior*.

To my friends, those who made this city feel like a true home, those who filled the solitude from moving to a new city, those who are my shelter and my daily motivation, those who believe in me no matter what, those to whom I look up as true examples, I am profoundly grateful to have you in my life. Those who have been by my side since high school, the ones I met through BEST, the ones I met in ERASMUS, thank you for choosing to be my friends, thank you for listening, thank you for existing.

To the team where I got to do this thesis, a true example of professionalism, and companionship between colleagues. I'm very grateful I got to attend all the meetings with you, for all the crazy scientist stories I got to hear, and for all the feedback given. I'll always look up to you guys.

Lastly, to my supervising team, PhD. Carlos Correia and Prof. António Mendes Lopes. For the guidance, mentorship, feedback, knowledge transferred, and constant support through out this journey. On a special note to Carlos for believing in me, even when things weren't so clear to me, for showing me there was an end to the tunnel that was worth the fight, for all the patience, endless meetings, and lessons taught. I'm truly grateful, thank you!

To all those mentioned above, I dedicate this work with all my heart.

Ana Margarida Soares de Freitas

" (...) continuo sendo o número treze, só estou estacionado no lugar do número quatorze."

José Saramago

Contents

List of Figures

List of Tables

List of Acronyms

AO	Adaptive Optics
AR	Autoregressive
DM	Deformable Mirror
EE	Ensquared Energy
ESA	European Space Agency
FEELINGS	FEEder LINks optical Ground Station
FSOC	Free Space Optical Communications
FWHM	Full Width Half Maximum
GEO	Geostationary Earth Orbit
IR	Infrared
ISS	International Space Station
LEO	Low Earth Orbit
LISA	LIght and Small Adaptive optics
LQG	Linear Quadratic Gaussian
LQR	Linear Quadratic Regulator
ML	Machine Learning
MMSE	Minimum Mean Square Error
NASA	National Aeronautics and Space Administration
OOMAO	Object Oriented Matlab Adaptive Optics
OMGI	Optimal Modal Gain Integrator
PSF	Point Spread Function
PSD	Power Spectral Density
RF	Radio Frequency
SH	Shack-Hartmann
SR	Strehl Ratio
VAR	Vector Autoregressive
WFS	Wavefront Sensor

List of Symbols

A_p	VAR(p) coefficient matrices
a_1, a_2	AR(2) Yule-Walker coefficients
b	Bufton profile sharpness parameter
$C_n^2(h)$	Refractive index structure constant at altitude h
$C_{ij}(\tau)$	Cross-covariance between layers i and j
$C_\phi(\rho)$	Spatial phase covariance
D	Telescope aperture diameter
$D_\phi(\tau)$	Temporal phase structure function
$d(\theta)$	Slant distance to satellite
dz	Phase screen thickness
f	Spatial frequency
f_s	Sampling frequency
H	Satellite orbital altitude
H_θ	Projection operator
h	Atmospheric altitude
h_t	Tropopause altitude
I	Beam intensity
$J(u)$	LQR quadratic criterion
k	Time step index
k_{r_0}	Fried's parameter mismatch factor
k_v	Wind speed mismatch factor
L_0	Outer turbulence scale
l_0	Inner turbulence scale
M	LQR time horizon
r	Spatial position
r_0	Fried parameter
T	Sampling period
t	Time
$U(r)$	Complex scalar field
v	Measurement noise
$v_{apparent}$	Apparent wind speed
v_g	Ground-level wind speed
$v_{natural}$	Natural wind speed
v_{sat}	Satellite orbital speed
v_t	Tropopause wind speed
v_{wind}	Total effective wind speed
x	State vector
$\hat{x}$	Estimation of the state vector

u	DM control command
y	WFS measurement
A,B,C,D	State-space system matrices
Q,R	LQR cost function weighting matrices
W	Reconstruction matrix
w	Process noise

ℓ	Discrete lag index, $\ell = 0, 1, ..., p$
λ	Optical wavelength
θ	Elevation angle
θ_ε	Wind direction robustness offset
ω_{sat}	Satellite angular velocity (rad/s)
Γ	Gamma function
$\Gamma_\phi(\tau)$	Temporal phase autocovariance
$\gamma_i(\tau)$	Temporal autocovariance at lag τ of a point i
κ	Wavenumber, $\kappa = 2\pi/\lambda$
$\Phi_n(k)$	Power spectrum of refractive index fluctuations
$\Phi_\phi(f)$	Phase power spectral density
ϕ	Wavefront phase
$\hat{\phi}$	Estimated wavefront phase
ϕ^{cor}	Corrected phase
ϕ^{res}	Residual phase
ϕ^{tur}	Turbulent phase
ρ	Distance between two points
Σ_ϕ	Spatial covariance matrix of phase
Σ'_ϕ, Σ''_ϕ	Spatial covariance matrix with 1, and 2 time-shifts
Σ_v	Covariance matrix of the process noise
Σ_w	Covariance matrix of the measurement noise
σ_I^2	Intensity variance
σ_ϕ^2	Phase variance
$\sigma^2(\tau)$	Temporal lag error
σ_χ^2	Log-amplitude variance
τ	Lag

Chapter 1

Introduction

1.1 Context and Motivation

Nowadays, space missions are becoming increasingly more sophisticated, and the amount of data they are capable of collecting and transmitting to Earth is rapidly increasing. To cope with this need, one option is to really on higher-bandwidth spectrums, such as the optical spectrum. The optical spectrum uses light as a means of transmitting information via lasers (NASA 2023).

Free Space Optical Communication (FSOC) systems benefit from data rates up to 40× higher, than the radio spectrum — from 5 Gbps to 200 Gbps (Kaushal et al. 2017). This higher bandwidth allows using shorter contact time to download mission data, decreasing the need for more terminals and ground stations.

This summer, the European Space Agency (ESA) has successfully completed an optical communication demonstration campaign using two observatories on Earth and NASA's Psyche mission, the spacecraft is currently flying at over 300 million km from Earth. This 30-minute roundtrip communication link enabled the reception of a data stream of 1.3 Mbps from a distance twice as far away as the sun and decoded the incoming data. This achievement lays the groundwork for a future in which data acquisition from deep space becomes more reliable, and mission data output can be significantly increased (ESA 2025).

In the case of satellite-to-ground communications, the altitude at which the satellite is orbiting is crucial, defining the time necessary to establish the two-way handshake. Geostationary Earth orbit (GEO) satellites orbit the Earth at approximately 35,786 km, while low Earth orbit (LEO) ranges between 300 km and 2,000 km. A satellite orbiting at 400 km has a latency close to 90× lower, relevant for applications like satellite internet.

However, when optical signals propagate through the atmosphere, they become highly susceptible to dynamic environmental conditions, such as turbulence, wind, and temperature gradients. These variations introduce wavefront distortions, which degrade signal quality and limit system performance. LEO satellites are especially challenging due to their fast movement across the sky.

Many techniques have emerged to mitigate these wavefront disturbances, including spatial filtering, error-correction coding, and post-processing reconstruction methods. However, unlike these approaches, Adaptive Optics (AO) operates in real time, actively compensating for distortions as they occur. This real-time correction makes AO particularly effective for preserving signal quality over long propagation distances.

AO was first developed for astronomical applications, where it is used to stabilize images and suppress jitter caused by atmospheric turbulence (Babcock 1953). A similar principle is applied in FSOC, but the environment poses distinct challenges. In FSOC, the line-of-sight must be continuously maintained with fast-moving LEO satellites, which makes telescope elevation a critical factor: at lower elevations, the optical beam travels through a longer atmospheric path, amplifying the impact of turbulence. In addition, the concept of apparent wind — arising from the relative motion between the satellite and the ground station — further influences the temporal dynamics of turbulence as perceived by the system. To address these effects, an AO system installed on the ground station senses the wavefront distortions with a wavefront sensor (WFS), estimates the required correction, and applies it in real time through a deformable mirror (DM), thereby compensating for atmospheric distortions and preserving the integrity of the transmitted optical signal.

1.2 Problem Statement

Despite their effectiveness, AO systems suffer from intrinsic latency due to sensor integration time, computational delays, and actuator response times. This delay leads to outdated correction commands by the time they are applied, resulting in residual wavefront error. In many AO implementations, this delay has been identified as a primary limitation to achieving optimal performance.

In a previously done study by Robles (2023) on AO systems for FSOC, the sources of error were analysed. The main source of error in AO systems is from fitting, caused by the mismatch between the wavefront and the best shape the DM can reproduce. The mitigation of this error is achieved by utilizing higher-end equipment, so it is outside the scope of this work. The second largest source of error is temporal error, which originates from the delay between wavefront measurement and correction in the AO loop. One promising approach to mitigate this issue is the use of predictive control. By forecasting the future state of the atmospheric wavefront, it is possible to apply more timely and accurate corrections, potentially reducing residual error and enhancing system performance.

The problem addressed in this thesis is the capability of a model-based predictive controller to improve wavefront correction, mitigating the effects of atmospheric turbulence, and enabling higher data-rate communications, as the state-of-the-art FSOC motivates.

1.3 Objectives of the Thesis

The main objective of this thesis is to evaluate the extent to which incorporating predictive control techniques into an AO system improves the quality of signal reception by the ground station in

FSOC. This includes implementing and comparing different predictive strategies, and quantifying performance improvements.

To introduce this topic, it is necessary to review the principles of FSOC, outlining its advantages and the challenges to propagation that arise from dynamic environmental conditions. Then, AO is introduced as a solution to these challenges, followed by a discussion on its intrinsic delays and the strategies to minimize them.

Figure 1.1 illustrates the conceptual pipeline of this thesis: starting from the demand for higher-bandwidth communications, FSOC emerges as a promising solution. However, its performance is highly sensitive to the propagation environment. To address this, AO is introduced, though it is itself limited by intrinsic delays. Predictive control is therefore expected to minimize these delays, bringing the wavefront correction of the AO system closer to the ideal.

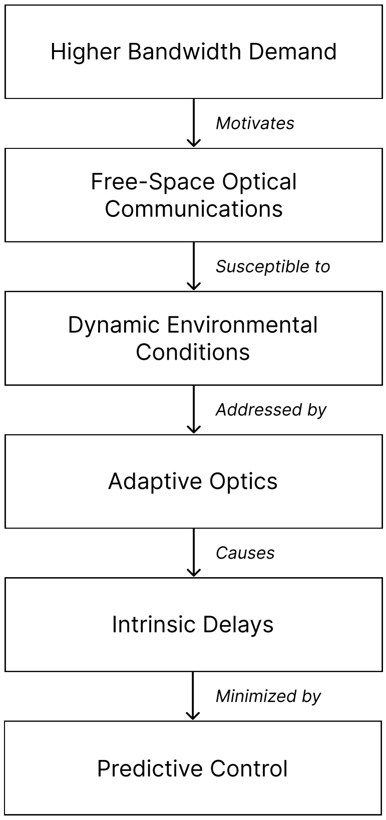

Figure 1.1: Conceptual pipeline from high-bandwidth demand to FSOC, its turbulence sensitivity, AO correction, and its delay, which is mitigated with the implementation of predictive control.

1.4 Methodological Overview

The simulations are carried out using the OOMAO framework (Conan and Correia 2014), where the optical channel, telescope, WFS, and DM are modeled to reproduce realistic propagation conditions. Within this environment, the AO control loop is formulated under an optimal Linear Quadratic Gaussian (LQG) framework, which integrates both the physical plant dynamics and the predictive models. The predictive component is tested through different formulations, including autoregressive (AR) models and state-space approaches, enabling a comparative evaluation of their ability to minimize AO delays.

The baseline for this study is two optical communication systems: *LISA* — LIght and Small Adaptive optics — a compact AO bench for telecommunications developed by ONERA (Giggenbach et al. 2022), and *FEELINGS* — FEEder LINks optical Ground Station — the ONERA optical communications ground station (Cyril et al. 2022).

The analysis is structured in four stages. First, a set of single-layer test cases is defined (Cases 1–5), representing increasingly challenging atmospheric conditions as well as two realistic configurations (*LISA* and *FEELINGS*). These cases establish a baseline for performance comparison across models. Second, a prediction gain analysis is performed specifically for the *LISA* and *FEELINGS* configurations to quantify the improvement in AO correction when predictive control is applied. Third, a sensitivity study investigates the effect of key simulation parameters — telescope diameter, Shack-Hartmann (SH) resolution, wind speed, sampling frequency, and Fried's parameter — on AO performance. The evaluation metrics considered throughout are the residual phase variance and the Strehl ratio (SR), which together provide a quantitative measure of wavefront correction quality. Lastly, the predictive models go through a robustness analysis of the estimated parameters — wind speed, module and direction, and the Fried parameter. This structured methodology enables a thorough comparison of predictive LQG strategies and their benefits for FSOC under realistic dynamic conditions.

1.5 Structure of the Thesis

This thesis is organized to progressively build a comprehensive understanding of predictive control in FSOC systems, from fundamental principles to advanced simulation-based evaluation.

Chapter 2 introduces the fundamentals of FSOC, including optical wave propagation, applications in space-to-ground links, and the impact of atmospheric turbulence. It also motivates the use of AO and outlines the main technical challenges in FSOC systems.

Chapter 3 describes AO systems, detailing their components — WFS, DM, and real-time control loops. It also covers wavefront reconstruction, performance metrics, and control strategies relevant to FSOC applications.

Chapter 4 presents model-based predictive control strategies for AO, including state-space modeling and the LQG framework. It discusses temporal prediction models, ranging from scalar autoregressive approaches to vectorial autoregressive models, with data-driven identification techniques founded on the Yule-Walker equations.

Chapter 5 evaluates the prediction models performance through simulations under various scenarios, including *LISA* and *FEELINGS* AO configurations. It analyzes prediction gain and assesses the influence of system parameters and their robustness, with the aim of achieving optimal wavefront correction.

Chapter 6 summarises the study's main conclusions, limitations, and future research opportunities.

Chapter 2

Fundamentals of Free Space Optical Communication (*FSOC*) Systems

FSOC systems require a line-of-sight connection between the transmitter and receiver for the propagation of information from one point to another. They rely on modulated light — typically generated by lasers — to propagate information through the atmospheric channel or free space toward the receiver, instead of guided optical fibers used in fiber-optic systems. Both the optical uplink (ground-to-satellite) and downlink (satellite-to-ground) involve the propagation of the optical beam through the Earth's atmosphere and free space (Kaushal and Kaddoum 2015).

Figure 2.1 pictures the ONERA *FEELINGS* optical ground station, where a world-first AO system enabled the optical link with a GEO satellite to be demonstrated. The 60 cm full-aperture telescope, equipped with advanced AO correction, enabled stable high-frequency optical communication despite atmospheric turbulence (Cyril et al. 2022).

Figure 2.1: ONERA's optical ground station *FEELINGS* established a stable two-way laser link with the Airbus Defence and Space TELEO payload in geostationary orbit (ONERA 2024).

To illustrate the overall structure of a FSOC system and its key components, Figure 2.2 presents a high-level block diagram, highlighting the transmitter, optical channel, and receiver.

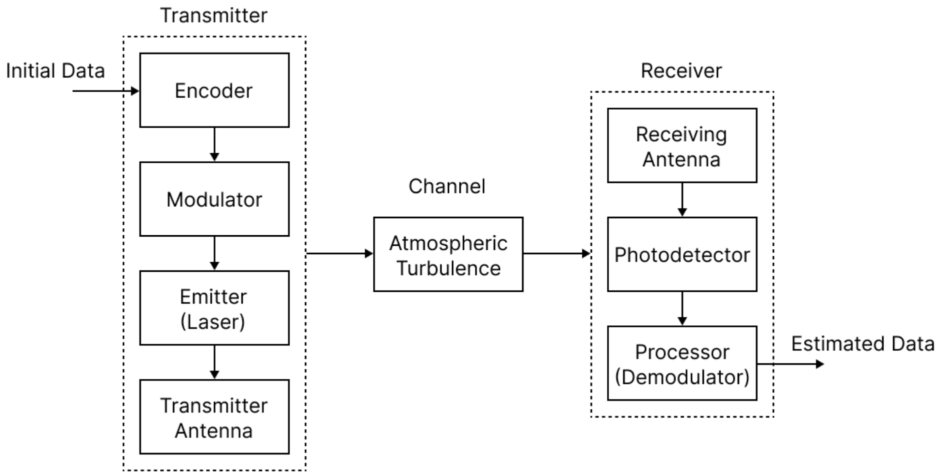

Figure 2.2: Block diagram of an FSOC link, from the transmitter to the receiver.

The transmitted data is first encoded and modulated before being propagated through the optical channel — the atmosphere. The received signal then undergoes demodulation and decoding at the receiver (Kaushal et al. 2017). This thesis focuses specifically on understanding and modeling the channel impairments, with the aim of optimizing signal reception through advanced predictive control techniques.

This chapter provides the theoretical background for FSOC systems. It begins with the physical principles governing optical wave propagation in free space, establishing the scientific basis for FSOC systems. Following this, the advantages of FSOC over traditional Radio-Frequency (RF) communication systems are discussed. Subsequently, the chapter explores the major technical challenges, with a particular focus on atmospheric turbulence. Introducing the origin of phase and amplitude distortions in an electromagnetic field caused by propagation through a turbulent environment. Finally, it introduces AO as a promising solution to mitigate these turbulence-induced impairments.

2.1 Principles of Optical Wave Propagation

FSOC is based on the transmission of modulated optical signals through the atmosphere. In idealized conditions, the optical beam can be locally modeled as a plane wave, solution of the homogeneous Helmholtz equation:

$$\nabla^2 U(\mathbf{r}) + k^2 U(\mathbf{r}) = 0 \tag{2.1}$$

where $U(\mathbf{r})$ is the complex scalar field and $\kappa = 2\pi/\lambda$ is the wave number, with λ the wavelength. A particular solution is the plane wave (Dessenne et al. 1998):

$$U(\mathbf{r}) = A \exp\left[i(\kappa \cdot \mathbf{r})\right] \tag{2.2}$$

where A is the amplitude, κ is the wave vector, and i is the imaginary unit ($i^2 = -1$).

However, as the beam propagates through the turbulent atmosphere, refractive index fluctuations distort the optical wavefront. These fluctuations are modeled statistically, most commonly through the Kolmogorov turbulence model, which assumes an inertial range where the power spectral density (PSD) — how the power of a signal is distributed across different frequencies — of the phase fluctuations follows (Kolmogorov 1991):

$$\Phi_\phi(f) \propto f^{-11/3} \tag{2.3}$$

where f is the spatial frequency. The Kolmogorov model assumes an infinite outer scale, meaning turbulence eddies of all large sizes contribute (Kolmogorov 1991). In practice, the von Kármán model introduces a finite outer scale L_0, modifying the PSD to (De Karman and Howarth 1938):

$$\Phi_\phi(f) \propto \left(f^2 + \frac{1}{L_0^2}\right)^{-11/6} \tag{2.4}$$

This refinement better represents real atmospheric conditions, where energy injection happens at large but finite scales.

In this thesis, the effects on the amplitude, or the scintillation effect (Section 2.5.5), are not considered. Instead, the analysis focuses on the fluctuations induced by phase distortions accumulated along the wavefront. This simplification allows for a first assessment of the proposed approach before extending it to a more complete model that incorporates amplitude effects.

The phase screen generated from these statistics represents a two-dimensional slice of the random wavefront distortions at a given propagation distance (Assémat et al. 2006). These screens typically exhibit smoothly varying phase structures with ripples and tilts at different scales, corresponding to turbulence eddies. Representations of phase screens appear as grayscale or false-color maps showing regions of positive and negative phase deviations, where larger structures represent low-frequency components and finer ripples represent high-frequency distortions, as it is illustrated in Figure 2.3.

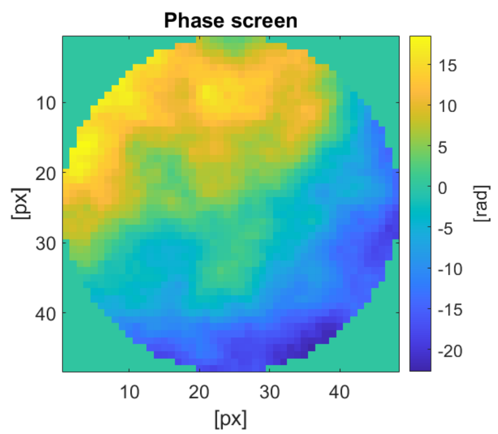

Figure 2.3: Representation of a simulated atmospheric phase screen for a circular telescope aperture, with 60 pixel spatial resolution.

These statistical properties are fundamental for predicting the temporal and spatial characteristics of the wavefront. For instance, the phase variance over an aperture of diameter D scales as:

$$\sigma_\phi^2 \propto \left(\frac{D}{r_0}\right)^{5/3} \tag{2.5}$$

where r_0 is the Fried parameter (coherence length). Similarly, the temporal power spectrum of the wavefront, linked via Taylor's frozen flow hypothesis (Section 2.5.2), provides the basis for designing predictive controllers.

Understanding these properties is crucial in FSOC systems, as they determine the required correction bandwidth and prediction horizon for AO systems. These models guide the simulation of phase screens and the design of AO control strategies capable of compensating for atmospheric distortions.

2.2 Applications in Space-to-Ground Communication

FSOC systems are predominantly employed in point-to-point communication links, encompassing a diverse range of applications such as terrestrial connections, namely smart grid infrastructures and inter-building data exchange, satellite-to-ground communication for space-based data transmission, and even underwater optical links, where traditional radio frequency methods are less effective (Jahid et al. 2022). Some of these examples are pictured in Figure 2.4.

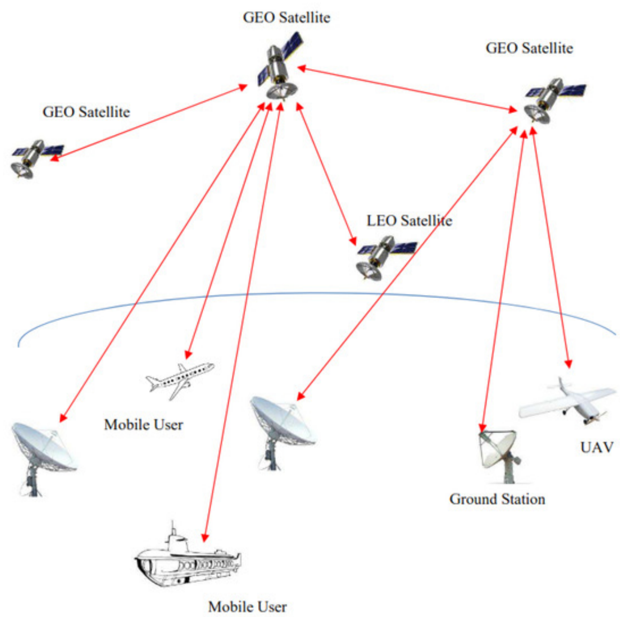

Figure 2.4: Illustration of applications of FSOC communication links (Goncalves Teixeira et al. 2021).

Key applications include satellite-to-ground links, where data collected in LEO satellites is sent back to Earth for processing, analysis, or real-time use in applications such as Earth observation, climate monitoring, telecommunications, and defence. These enable the rapid transmission of high-resolution imagery, scientific measures, and other critical data.

2.3 Motivation for Adaptive Optics in FSOC

For FSOC systems to deliver the high-capacity, low-latency performance required by modern space and terrestrial applications, the optical beam must arrive at the receiver nearly undistorted. Yet, the very properties that give FSOC its advantage — narrow beam divergence and short wavelengths — also make it extremely vulnerable to atmospheric turbulence. Turbulence-induced wavefront distortions can collapse the coupling efficiency, trigger sharp increases in bit error rate, and even break the link entirely, particularly in long-distance or low-elevation satellite-to-ground paths where the atmospheric column is thickest. Without effective correction, these impairments can nullify the system's bandwidth advantage.

AO directly addresses this limitation by sensing and correcting wavefront errors in real time, preserving beam quality and enabling FSOC to meet its performance potential under dynamic and unpredictable atmospheric conditions. Chapter 3 will present the principles, components, and role of AO in reducing turbulence-induced errors.

2.4 Advantages and Technical Challenges

In FSOC systems, information is transmitted using optical beams, while RF systems use radio waves. In optical communications, the wavelength can range from 700 to 1600 nm, and RF systems range between 30 mm to 3 m. These shorter wavelengths and higher frequencies of the infrared (IR) spectrum allow wider bandwidths — since an increase in carrier frequencies increases the capacity of a communications system to carry information, thus increasing the amount of data transmitted per unit of time (Kaushal et al. 2017).

Additionally, FSOC systems provide enhanced security due to the narrow beam divergence — the spreading of the laser beam as it propagates — since it is proportional to λ/D, where D is the aperture diameter and lower values of λ impose less divergence. This makes eavesdropping or interception more difficult.

Finally, optical links are largely immune to electromagnetic interference, including those from terrestrial sources, such as radio towers or atmospheric electric fields, making them particularly robust in environments where RF performance may degrade.

Nevertheless, FSOC systems encounter substantial technical challenges that can critically affect overall performance. Table 2.1 summarises the main error sources and their origins, for a system with AO. Assessing the contribution of each error term through an error budget analysis is essential to identify where system improvements can be made.

Table 2.1: Main adaptive optics system error terms.

Name	Symbol	Origin
Fitting error	$\sigma^2_{fitting}$	Mismatch between the actual wavefront shape and the best shape the deformable mirror can reproduce.
Aliasing error	$\sigma^2_{aliasing}$	Misinterpretation of high-frequency wavefront distortions as lower-frequency ones due to limited WFS sampling.
Temporal error	$\sigma^2_{temporal}$	Delay between wavefront measurement and correction in the AO loop.
Noise error	σ^2_{meas}	Measurement noise from the WFS that propagates to the wavefront reconstruction.

In an error budget analysis, Robles (2023) quantified the sources of potential performance gains and losses for *LISA* and *FEELINGS*, with the results shown in Figure 2.5. The study examined the evolution of phase variance as the elevation angle of a LEO satellite changes during its link with the ground station. It provides a residual phase variance budget for fitting, aliasing, temporal, and measurement noise errors.

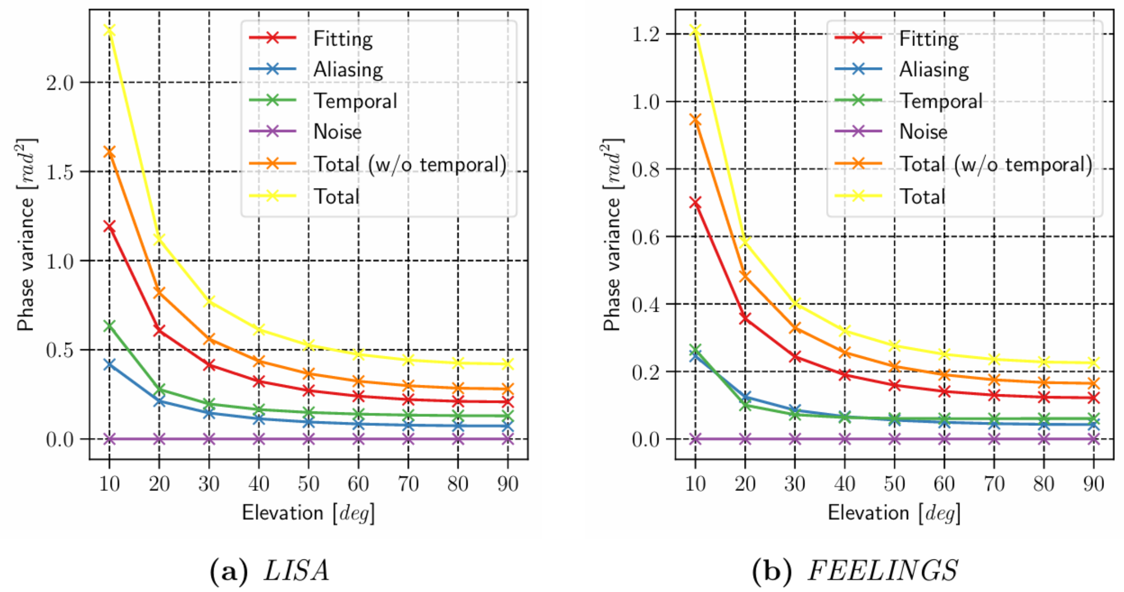

Figure 2.5: Plot representing the AO budget for the two system configurations considered (Robles 2023).

LISA and *FEELINGS* are two different simulation configurations that have been tested on-sky, by *ONERA* (Giggenbach et al. 2022; Phung et al. 2021; Cyril et al. 2022). Both systems exhibit a similar error budget structure — *FEELINGS* is a more sophisticated system, thus the lower total phase variance. From this study, the dominant source of error is fitting, and temporal errors represent the second largest source of error. These temporal errors are expected to be mitigated by predictive control, which is the focus of this thesis. The orange curve represents the total residual phase variance without temporal error, illustrating that correcting for temporal errors would result in significant performance uplift.

2.5 Atmospheric Turbulence and Its Effects on Optical Links

Optical communication offers remarkable advantages in terms of bandwidth, security, and latency. However, its reliability depends critically on the stability of the propagation channel. In satellite-to-ground links, the atmosphere introduces phase and amplitude distortions due to turbulence, which can severely degrade signal quality. Understanding how these effects manifest over space and time is essential for designing robust compensation and control strategies.

2.5.1 Nature and Origin of Atmospheric Turbulence

Atmospheric turbulence is driven by temperature, pressure, humidity, and wind velocity gradients, which produce random fluctuations in the refractive index of air, both spatially and temporally. As an optical wave is being propagated through the atmosphere, it is distorted by these fluctuations in the refractive index of air.

Turbulence is described by the Navier-Stokes equations and, because of the inherent difficulty in solving this set of equations, Kolmogorov (1991) developed a statistical theory in 1941 describing its behavior — the fundamental theory for this thesis.

According to Kolmogorov's theory, turbulence in the atmosphere can be imagined as a mix of swirls of different sizes, called eddies. Large eddies form when energy enters the system (for example, from the wind or heat differences near the ground). These large eddies break down into smaller and smaller ones, in a process known as the energy cascade. This continues until the eddies are so small that their energy is dissipated as heat, as can be seen in Figure 2.6.

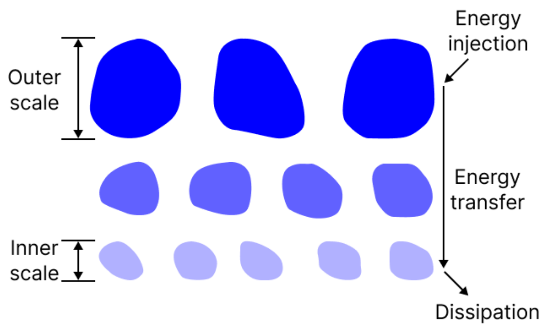

Figure 2.6: Diagram illustrating the energy injected into the flow (e.g., by solar heating) cascades from large eddies to progressively smaller ones until dissipated at the inner scale.

The largest size of these eddies is called the outer scale L_0, and the smallest ones are limited by the inner scale l_0. Between these two scales, the turbulence behaves in a statistically predictable way. In this range, the variations in air density — and therefore in the refractive index — follow a well-known model called the Kolmogorov spectrum, which describes how much turbulence energy exists at each spatial scale (or spatial frequency). The power spectrum of the refractive index fluctuations is given by:

$$\Phi_n(f) = 0.033 C_n^2 f^{-11/3}, \quad 1/L_0 \ll f \ll 1/l_0 \tag{2.6}$$

where f is the spatial frequency, which describes how rapidly the refractive index varies over space — higher f values correspond to smaller eddies and finer-scale distortions. The Kolmogorov model is valid within the inertial range, bounded by the inner scale l_0 and outer scale L_0 of turbulence.

These variations are quantified by the refractive index structure constant C_n^2, a central parameter in optical turbulence modeling (Andrews 2019). It quantifies the intensity of turbulence at a given altitude or location and is usually modeled as a function of altitude, $C_n^2(h)$. Higher values of C_n^2 indicate stronger turbulence and greater distortion of the optical wavefront. The Hufnagel-Valley vertical profile model, Equation (2.7), describes how the refractive index structure constant behaves through altitude, h, in meters above ground level — for a 90° elevation (Andrews and Beason 2023).

$$C_n^2(h) = 0.00594 \left(\frac{v_{natural}}{27}\right)^2 \left(h \times 10^{-5}\right)^{10} e^{-h/1000} + 2.7 \times 10^{-16} e^{-h/1500} + C_0 e^{-h/100} \tag{2.7}$$

where the parameter $v_{natural}$ is the root mean square upper atmospheric natural wind speed, and C_0 is the value of C_n^2 at ground level.

Table 2.2: Typical atmospheric parameters used in the Hufnagel-Valley model for different turbulence strengths

Name	*High*	*Moderate*	*Low*	Units
Natural wind speed, $v_{natural}$	30	21	10	m/s
C_n^2 at ground level C_0	5	1.7	0.1	$\times 10^{-14}$ m$^{-2/3}$

Figure 2.7 shows how the C_n^2 behaves in the atmosphere, highlighting a decrease as altitude increases — meaning that turbulence effect in the refractive index is stronger near the surface. In this illustration, different simulation conditions are exhibited, according to those presented in Table 2.2.

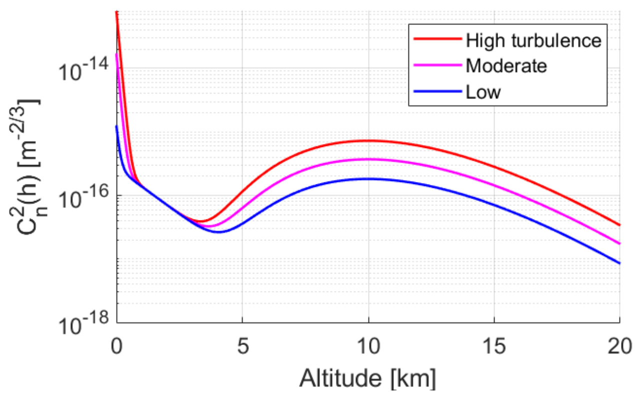

Figure 2.7: Illustration of the C_n^2 profile through the atmosphere for the different environments of Table 2.2, for an elevation of 90°.

There are other parameters to express the turbulence strength, one of which is Fried's parameter (Fried 1982):

$$r_0(\theta) = \left[0.423\,\kappa^2 \sec(\theta) \int_{path} C_n^2(h)\, dh\right]^{-3/5} \tag{2.8}$$

where $\kappa = 2\pi/\lambda$ is the wavenumber, θ is the elevation angle above the horizon, and $C_n^2(h)$ is the refractive index structure constant as a function of altitude h. It describes the integrated coherence length of the turbulence phase distortion along a propagation path. Assuming a Kolmogorov spectrum, it is defined such that a telescope with aperture equal to r_0 would experience an average phase variance of 1 rad^2 across its pupil. A smaller value of r_0 indicates stronger turbulence and therefore more severe wavefront distortion. Typical values range from a few centimeters in poor conditions to several tens of centimeters under excellent seeing conditions.

In order to study and simulate the effects of turbulence on optical wave propagation, a common approach is to discretize the atmosphere into a finite number of horizontal layers (Roggemann et al. 1995). Where each layer represents a slice of the atmosphere at a given altitude, characterized by its own turbulence strength, wind speed, and direction. Each layer acts as a phase screen of thickness dz — so thin that the propagation effects within itself are neglectable — they are assumed to be statistically independent from each other, and cumulative — meaning that the total effect of turbulence along the optical path is the sum of the contribution from all the layers, Figure 2.8 illustrates this phenomenon.

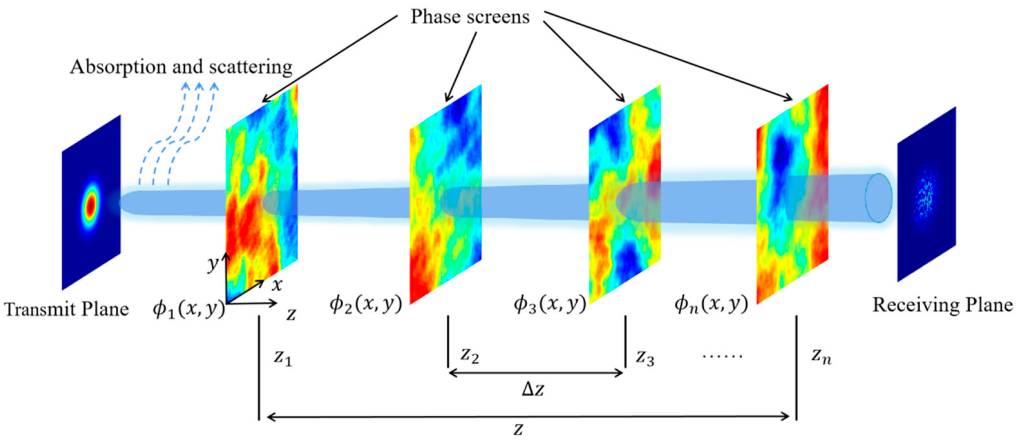

Figure 2.8: Diagram representing the progression of the phase screens in the atmosphere (Jiang et al. 2023).

In a layered turbulence model, the total integral is approximated as the sum of contributions from each layer. This allows defining an r_0 value per layer, based on its local C_n^2 and thickness. These individual r_0 values help simulate how much each layer contributes — expressed as the fractional r_0 — to the overall distortion and are used to scale the amplitude of phase screens during simulation.

Understanding, predicting, and compensating for this phase distortion is the central challenge when designing an effective correction system for FSOC links. Thus, the number of layers used to describe the atmosphere, in the simulations, will be analyzed to assess its impact on the system's performance.

2.5.2 Time Dynamics

The temporal evolution of turbulence depends on the dynamics of the atmosphere, however at short time scales — such as those encountered in high frequency FSOC AO systems — the turbulence can be considered steady, and the evolution driven by the translation of wind. This is called the Taylor's frozen flow hypothesis, which states that the turbulence phase does not change in space — it is frozen — but it is driven by a shift of the frozen phase screen according to the wind speed (Taylor 1938).

For a given layer, Taylor's frozen flow hypothesis assumes that:

$$\phi(\mathbf{r}, t+\tau) \approx \phi(\mathbf{r} - \mathbf{v}\cdot\tau, t) \tag{2.9}$$

where ϕ is the phase distortion, $\mathbf{r}$ is the spatial position, τ is a time delay, and $\mathbf{v}$ is the wind velocity vector.

Figure 2.9 illustrates this relation, the spatial shift of a point caused by the action of the wind vector $\mathbf{v}$ in a period τ. The whole phase screen is shifted spatially according to the direction of the wind vector. The red point after a delay of τ holds the same value but in a different spatial location.

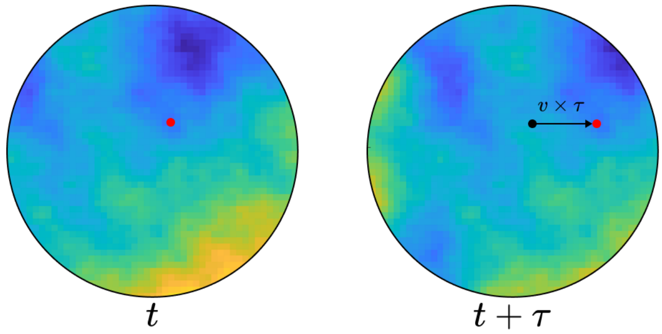

Figure 2.9: Representation of the frozen flow hypothesis, relating the temporal delay τ with the spatial shift caused by the wind v_{wind} of the phase screen.

This hypothesis is crucial for analytically computing temporal turbulence statistics, as it enables their derivation from spatial statistics — based on the Kolmogorov turbulence model.

In the context of LEO satellite links, the frozen flow hypothesis becomes even more applicable due to the presence of a strong apparent wind; the high angular velocity of the satellite motion relative to the ground creates an effective sweeping of the turbulence across the telescope's line of sight. This apparent motion reinforces the validity of treating the turbulence as being frozen over short intervals, enhancing the predictive power of the model.

This study, as an initial investigation of predictive models for FSOC AO systems, neglects the boiling component of turbulence inherent to highly turbulent environments with scintillation — characterized by strong thermal gradients or internal dynamics. This simplification assumes that the dominant behavior is translational, as the frozen flow in Taylor's hypothesis.

2.5.3 Wind Profiles

In the frozen flow hypothesis, wind speed and direction strongly influence the turbulence strength and the understanding of its temporal evolution. Consequently, it is essential to model wind profiles accurately along the propagation path, considering both the altitude-dependent wind characteristics and the telescope elevation angle, which varies during satellite tracking. The total wind has two components: the natural wind and the apparent wind, due to satellite tracking (Robles 2023).

The natural wind component depends on the vertical height h of the layer and is modeled using the empirical Bufton (1973) profile:

$$v_{natural}(h) = v_g + (v_t - v_g)\left(\frac{h}{h_t}\right)^b \exp\left[b\left(1 - \frac{h}{h_t}\right)\right] \tag{2.10}$$

where v_g is the wind speed at ground level, v_t is the wind speed at the tropopause, h_t is the typical tropopause height, and b is the profile sharpness parameter. Higher values of b give a higher fidelity model, and sharper transition between ground and upper atmospheric wind speeds. In this study, a value of $b = 10$ is adopted, representing a relatively sharp transition, consistent with values reported in literature for FSOC scenarios.

The apparent wind results from the angular motion of the telescope as it tracks the satellite, as a projection of the angular velocity onto the turbulent layer. It depends on the layer height, the altitude at which the satellite is orbiting, and the telescope's angular velocity ω_{sat}. The angular velocity of the satellite depends on its elevation, relative to the telescope, and the slant distance to the satellite is given by:

$$d(\theta) = \frac{H}{\sin(\theta)}, \tag{2.11}$$

with θ representing the elevation angle of the telescope ($\theta = 90^\circ$ at zenith, and $\theta = 0^\circ$ at the horizon), and H the altitude at which the satellite is orbiting — between 300 and 2,000 km.

Assuming the satellite moves with orbital speed v_{sat}, the angular speed seen from ground is:

$$\omega_{sat}(\theta) \approx \frac{v_{sat}}{d(\theta)} = \frac{v_{sat} \cdot \sin(\theta)}{H} \tag{2.12}$$

This shows that the angular velocity decreases as the elevation decreases, and the maximum relative speed of the satellite is achieved when it is orbiting around the zenith — also where the propagation distance is shorter.

The apparent wind velocity at each atmospheric layer, with altitude h is:

$$v_{apparent}(h, \theta) = \omega_{sat}(\theta) \cdot h = \frac{v_{sat} \cdot h \cdot \sin(\theta)}{H} \tag{2.13}$$

The total wind speed experienced by the turbulence layer is therefore given by:

$$v_{wind}(h, \theta) = v_{natural}(h) + \frac{v_{sat} \cdot h \cdot \sin(\theta)}{H} \tag{2.14}$$

Figure 2.10 depicts the relationship between the apparent wind speed and the elevation angle, as defined in Equation (2.13), from the satellite's position at the horizon to the zenith, showing how the value increases.

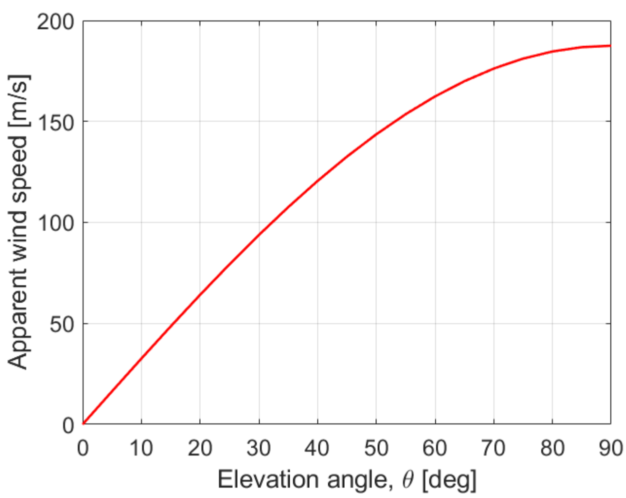

Figure 2.10: Plot showing the evolution of the apparent wind speed according to elevation, for a satellite with an average speed of 7.5 km/s at 400 km of altitude, for a layer at 10 km.

Figure 2.11 illustrates the resulting wind profiles for two representative elevation angles: 30° and 90°. The vertical axis represents the effective distance of each atmospheric layer from the ground station, which is inherently dependent on the satellite's elevation angle. A lower elevation angle increases the optical path length through the atmosphere, thereby altering the mapping between physical altitude and layer distance as seen from the station. The analysis was conducted for a satellite in low Earth orbit, traveling at a velocity of 7.5 km/s at an altitude of 400 km.

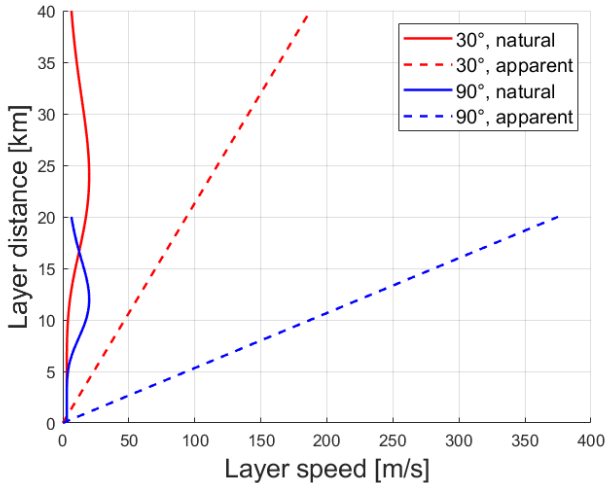

Figure 2.11: Plot representing the natural wind profile given by the Bufton profile and apparent wind from the satellite tracking, at different elevations. Satellite at 400 km of altitude, with an average speed of 7.5 km/s.

For the case of a layer at 10 km of altitude, when the elevation is 30°, it is at a slant distance of $10/\sin(30°) = 20$ km. The apparent wind of that layer at the maximum elevation is 187.5 m/s, and for 30° it is 93.75 m/s, decreasing roughly by a factor of two. This simple case highlights how the satellite's elevation strongly modulates the effective wind speed perceived by the AO system. These considerations establish the boundaries for the analysis presented in Chapter 5, where the impact of varying wind speeds on wavefront correction performance is systematically evaluated.

In this case, the natural wind is assumed to have the same orientation as the apparent wind. If that is not true, the argument for the wind vector in each layer may change.

2.5.4 Statistical Characterization of Turbulence

This work adopts a zonal wavefront representation, where the optical phase is discretized at spatial nodes aligned with the subapertures of a Shack-Hartmann wavefront sensor (will be discussed further in Section 3.2.1). This approach enables direct mapping between measured gradients and phase estimates, making it well-suited for both reconstruction and predictive modeling in AO.

To describe the behavior of atmospheric turbulence in this zonal context, statistical tools that model the expected relationships between phase values across space and time were used. These tools include spatial covariance, temporal autocovariance, and cross-covariance between layers, all of which are derived from the underlying structure of turbulence and form the basis for predictive estimation techniques.

2.5.4.1 Spatial Covariance of the Zonal Wavefront

The spatial covariance between wavefront phase values at two points separated by a distance ρ is defined as (Assémat et al. 2006):

$$C_\phi(\rho) = \left(\frac{L_0}{r_0}\right)^{5/3} \frac{\Gamma(11/6)}{2^{5/6}\pi^{8/3}} \left[\frac{24}{5}\Gamma\left(\frac{6}{5}\right)\left(\frac{2\pi\rho}{L_0}\right)^{5/6} K_{5/6}\left(\frac{2\pi\rho}{L_0}\right)\right] \tag{2.15}$$

where L_0 is the outer scale of turbulence, r_0 is the Fried's parameter, Γ represents the Gamma function, $K_{5/6}$ is a modified Bessel function of the third order, and ρ is the distance between two zonal points.

This expression describes the expected phase correlation as a function of spatial separation ρ, and is fundamental in constructing the spatial covariance matrix $\mathbf{C}_\phi \in \mathbb{R}^{N\times N}$, which characterizes the turbulence-induced distortion over the aperture. The spatial covariance for a 0.6 m diameter aperture sampled at a 60×60 pixels resolution is presented in Figure 2.12.

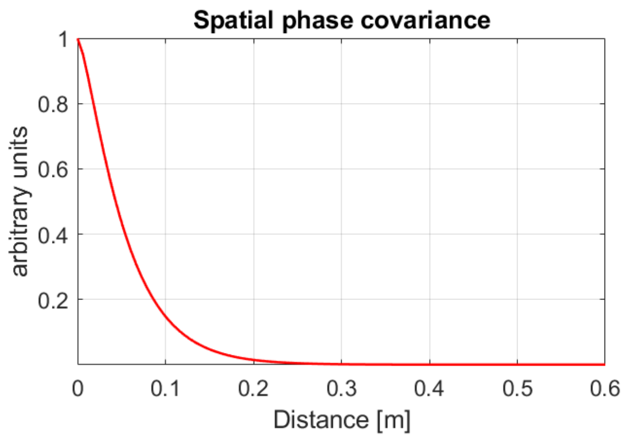

Figure 2.12: Plot representing the spatial phase covariance $C_\phi(\rho)$ across a pupil with 0.6 m of diameter, and resolution of 60×60 pixels.

The graph is normalized to highlight, at this resolution, the influence of two points separated by a distance ρ across the pupil on each other. The minimum separation between two points at this resolution is 0.01 m, for which they exhibit 90% spatial covariance, meaning their phase values are almost identical. Up to a distance of 0.1 m the correlation between phase values is still considerable — more that 10%.

Understanding the spatial relationship between the phase values at each point reveals that the wavefront exhibits a certain continuity, where two consecutive points are never drastically different from each other. Therefore, when predicting the phase value at a given point, its surrounding points are likely to have a significant influence.

2.5.4.2 Temporal Autocovariance and the Frozen Flow Hypothesis

Temporal prediction relies on the autocovariance of the wavefront over time. For a point on the wavefront, the autocovariance at a time lag τ is given by:

$$\Gamma_{\phi}(\tau) = \left\langle \phi(t)\phi(t+\tau)^{\top} \right\rangle \tag{2.16}$$

Using the frozen flow hypothesis (Section 2.5.2), it is assumed that turbulence is transported over time by wind without changing its internal structure — as a fixed grid through the aperture. This enables approximating the wavefront at a future instant as a spatially shifted version of the current wavefront:

$$\phi(\mathbf{r}, t+\tau) \approx \phi(\mathbf{r} - \mathbf{v} \cdot \tau, t) \tag{2.17}$$

where $\mathbf{v}$ is the wind velocity vector. This spatial shift means that temporal statistics can be derived directly from the spatial covariance model $C_{\phi}(\rho)$, by evaluating it at the displacement corresponding to the wind transport:

$$\Gamma_{\phi}(\tau) \approx C_{\phi}\left(\frac{\rho}{v_{wind}}\right) \tag{2.18}$$

The temporal autocorrelation of each spatial point of the wavefront, computed according to Equation (2.18) for a 0.6 m diameter aperture sampled at a 60×60 pixel resolution with a wind speed of 140 m/s, is presented in Figure 2.13.

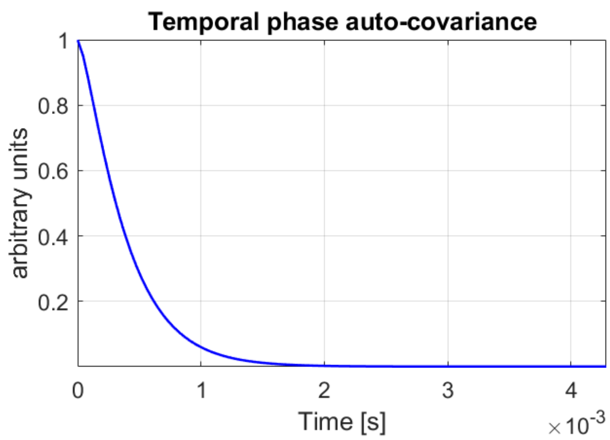

Figure 2.13: Plot representing the temporal phase auto-covariance $\Gamma_{\phi}(\tau) \approx C_{\phi}(\rho/v_{wind})$ for each spatial point on the wavefront with $v_{wind} = 140$ m/s.

This relationship is essential in deriving linear prediction models such as autoregressive estimators. FSOC systems operate between 1000 Hz and 5000 Hz, with sampling periods of 0.001 s and 0.0002 s, respectively. That is where the interest in working at high frequencies lays ground: a point is more correlated with its past values when the time interval between them is shorter. Thus, it is expected that better correction of the wavefront could be achieved, as the prediction relies on more strongly correlated data and is therefore less susceptible to rapid decorrelation effects introduced by atmospheric turbulence.

2.5.4.3 Cross-Covariance Between Atmospheric Layers

In a multi-layer atmospheric model, each layer introduces its own phase distortion and is transported by its respective wind vector. To fully describe this system, the statistical dependency between different layers has to be modeled. The cross-covariance between layers i and j is given by:

$$\mathbf{C}_{ij}(\tau) = \left\langle \phi_i(t)\phi_j(t+\tau)^\top \right\rangle \tag{2.19}$$

When layers are assumed independent (a common simplification), $\mathbf{C}_{ij} = 0$ for $i \neq j$. However, in tomographic reconstruction or multi-layer Kalman filtering, these cross-layer terms become important — especially when wind speeds are similar or overlapping volumes exist in the field of view.

The full spatio-temporal covariance structure — including cross-layer interactions — is used to construct augmented state models and train optimal predictors that operate in dynamic conditions.

In summary, the zonal-based statistical modeling of phase — using spatial covariance, temporal autocovariance, and inter-layer cross-covariance — provides a compact and predictive description of atmospheric turbulence. These models enable the development of optimal estimation and control strategies that compensate for wavefront distortion in FSOC systems.

2.5.4.4 Temporal Structure Function

A generalized structure function $D(\rho)$ is a statistical tool used to quantify differences between realizations of a stochastic process u separated by ρ:

$$D(\rho) = \left\langle \|u(x+\rho) - u(x)\|^2 \right\rangle, \tag{2.20}$$

where $\langle \cdot \rangle$ denotes an ensemble average over all realizations.

For this work, the temporal structure function is a valuable tool that characterizes how the phase of a turbulent wavefront evolves. In essence, it quantifies the expected variance between two realizations of the wavefront phase separated by a time lag τ. This measure is particularly relevant in AO prediction, since temporal fluctuations of the phase determine how accurately future wavefronts can be estimated from past measurements. Taking the form of:

$$D_\phi(\tau) = \left\langle \|\phi(t+\tau) - \phi(t)\|^2 \right\rangle, \tag{2.21}$$

which evaluates the temporal separation of two phase values separated by a lag of τ. This relationship between two temporally separated points can also be expressed by the temporal covariance Γ_ϕ (Tyson and Frazier 2022):

$$D_\phi(\tau) = 2 \cdot \left(\Gamma_\phi(0) - \Gamma_\phi(\tau)\right) \tag{2.22}$$

This is the baseline to evaluate the temporal evolution of the wavefront's phase if there was no prediction. In the case where wavefront estimation is done, the analogous metric is the temporal prediction error. It can be written as (Jackson et al. 2015):

$$\sigma^2(\tau) = \left\langle \|H_\theta(\phi_{k+1} - \hat{\phi}_{k+1})\|^2 \right\rangle, \tag{2.23}$$

where $\hat{\phi}_{k+1}$ denotes the estimate of the phase at time step $k+1$, and H_θ represents the projection operator onto the modes of interest. The variance $\sigma^2(\tau)$ therefore expresses the mean squared difference between the true and the predicted phase after a temporal shift of length τ.

This expression can be reformulated in terms of the covariance of the phase:

$$\sigma^2(\tau) = \operatorname{trace}\{H_\theta(\Sigma_\phi - \Sigma'_\phi)H_\theta^\top\} \triangleq D_t(\tau), \tag{2.24}$$

where Σ_ϕ is the spatial covariance matrix and Σ'_ϕ is its time-shifted counterpart, $\Sigma'_\phi = \Sigma_\phi(\rho' = \rho + \|v\|\tau)$ from Equation (2.15).

Describing the phase as an autoregressive process:

$$\begin{aligned} \phi_{k+1} &= A\phi_k + \varepsilon_k, \\ \phi_{k+1} &= A\phi_k + B\phi_{k-1} + \varepsilon_k, \end{aligned} \tag{2.25}$$

where the first equation corresponds to an AR(1) model and the second to an AR(2) model (Section 4.3.1). Here, the matrices A and B capture the temporal correlations between successive phase screens, while ε_k represents the innovation (unmodeled turbulence) at step k.

The temporal structure function from Equation (2.24) can be expanded for the cases presented in Equation (B.1), as demonstrated in Appendix A:

$$\begin{aligned} \sigma^2_{p=1}(\tau) &= \operatorname{trace}\{H_\theta(\Sigma_\phi + A\Sigma_\phi A^\top - 2\Sigma'_\phi A^\top)H_\theta^\top\} \\ \sigma^2_{p=2}(\tau) &= \operatorname{trace}\{H_\theta(\Sigma_\phi + A\Sigma_\phi A^\top + B\Sigma_\phi B^\top + 2A\Sigma'_\phi B^\top - 2(A\Sigma'_\phi - B\Sigma''_\phi)H_\theta^\top\} \end{aligned} \tag{2.26}$$

These derivations of the temporal lag error for first- and second-order models — $p = 1$ and $p = 2$ respectively — provide a clear link between the model parameters and the expected phase variance over a time lag τ. These expressions will be used to evaluate how different predictive models affect the residual phase variance and, consequently, the variation of the SR (Section 3.4) with temporal lags. This allows a direct assessment of the performance improvement achievable through predictive control in AO systems.

2.5.5 Scintillation and Wavefront Distortion

Scintillation, easily seen as the twinkling of stars at night, has been described as the rapid changes in brightness of light, caused by amplitude fluctuations of the wavefront (Gracheva and Gurvich 1965). This amplitude fluctuation, represented by the log-amplitude variance σ_χ^2, is a function of the propagation length L, and the turbulence strength:

$$\sigma_\chi^2 \approx \left(\frac{2\pi}{\lambda}\right)^{7/6} L^{11/6} C_n^2 \tag{2.27}$$

The variance of the log-amplitude is related to the variance of intensity through:

$$\sigma_I^2 = A\left[\exp(4\sigma_\chi^2) - 1\right] \tag{2.28}$$

where A is the aperture averaging factor, which depends on the turbulent conditions — the aperture diameter and the wavenumber.

Scintillation index, σ_I, is a measure of the normalized beam intensity, I.

$$\sigma_I^2 = \frac{\langle I^2\rangle - \langle I\rangle^2}{\langle I\rangle^2} \tag{2.29}$$

While scintillation introduces amplitude fluctuations that can severely degrade FSOC link quality, its modeling involves complex Rytov-based formulations and stochastic beam spreading. In this study, amplitude effects are deliberately excluded to isolate and quantify the predictive control performance against phase-only distortions. This simplification provides a lower bound on error and establishes a clean benchmark for future extensions that incorporate scintillation.

2.6 System Delay

In FSOC systems, temporal dynamics play a decisive role in link stability and performance. A major limiting factor is the presence of delay, which introduces a temporal mismatch between the actual state of the optical channel and the system's response; the effects of this temporal mismatch in the system performance have been previously shown in Figure 2.5. Even small delays can reduce the effectiveness of turbulence compensation or tracking loops, leading to residual phase errors and degraded signal quality.

Delays in FSOC arise from several mechanisms. The finite speed of light introduces a propagation latency that, while negligible for short terrestrial links, becomes non-negligible in satellite-to-ground communication, where one-way delays can reach milliseconds. Additional contributions come from the acquisition and processing stages — since wavefront sensors and digital processors require finite integration and computation times —, as well as from actuation — as deformable mirrors, fast steering mirrors, and other optical elements cannot respond instantaneously. Altogether, these effects mean that the correction is applied not to the instantaneous wavefront, but to one that has already evolved under the influence of turbulence and platform motion. The consequence is an imperfect compensation, leaving behind a residual wavefront error that directly limits communication performance.

For this reason, system delay must be explicitly modeled and addressed in FSOC design. While one possibility is to reduce latency through faster hardware, a complementary and often more effective approach is algorithmic: predictive control. By exploiting the temporal correlations of atmospheric turbulence, predictive methods aim to estimate the future state of the wavefront and compensate for it in advance, thereby minimizing the error induced by delay. In the following chapters, predictive control techniques will be studied and their ability to mitigate residual errors in FSOC systems will be assessed.

2.7 Summary

This chapter covered the theoretical foundations of FSOC, a brief passing through the principles of optical wave propagation, to highlight how a plane wave has an amplitude and phase component. As the beam is propagated through the atmosphere, the atmospheric turbulence induces fluctuations both in phase, and amplitude. The fluctuations in amplitude, also denoted as scintillation, are prone to occur in very turbulent environments — for example, low elevation angles, or places with worse seeing conditions as urban areas. This study will dive into the phase fluctuations, which degrade the quality of the optical link and can even disrupt the whole link, serving as a baseline study.

The high sensitivity to atmospheric effects motivates AO to be applied to FSOC systems, operating in real time and compensating for the phase disturbances that lead to signal fading, and reduced data rates. The error budget analysis conducted by Robles (2023) concluded that the second largest source of residual phase variance — after correction — arises from temporal error, a consequence of the delay between measurement of the wavefront and its correction, motivating for predictive control strategies.

The atmospheric turbulence model used in this study is described, including its nature and origin, the evolution of turbulence under the frozen flow hypothesis, and the wind profiles, which incorporate a new component: the apparent wind resulting from the relative motion of the satellite with respect to the atmospheric layer. Adopting a zonal approach to represent the wavefront, the optical phase is discretized at spatial points across the telescope pupil. The model is constructed from its theoretical statistical characterization, allowing a parallelism between space and time, driven by the frozen flow hypothesis. This translation between space and time is the key that opens the door to the identification of predictive models (presented in Section 4.3.2).

The key takeaways are that AO is crucial and requires a control unit with predictive capability to mitigate the disturbances caused by atmospheric turbulence, which is derived from the spatio-temporal statistics of turbulence.

Chapter 3 proceeds to cover the principles of AO, its components, performance metrics, and a discussion on different control strategies, concluding with the approach that best fits the needs of correcting the wavefront to guarantee connectivity between the transmitter and the receiver, which will be further developed in Chapter 4.

Chapter 3

Adaptive Optics for Turbulence Mitigation

In the previous chapter, the effects of atmospheric turbulence on FSOC were examined. These effects, particularly the distortion of the optical wavefront, were shown to significantly degrade the signal quality and system performance. These distortions can vary rapidly and unpredictably, especially in outdoor or long-range applications — such as the ones being discussed in this thesis. To address this challenge, this chapter introduces AO as a key technology for real-time correction of wavefront distortions.

This chapter presents the fundamental principles of AO, including its feedback control mechanism and equipment. Followed by a discussion of this application in FSOC environments. The goal is to provide a comprehensive understanding of how AO can enhance link stability and data integrity in the presence of atmospheric disturbances.

3.1 Principle of Adaptive Optics

Adaptive optics is a technique that is used to correct distortions in optical signals as they travel through the atmosphere (Roddier 1999). These distortions, often caused by temperature gradients and wind, lead to fluctuations in the signal's intensity and direction. AO systems are designed to detect these changes and apply real-time corrections to maintain a stable and focused beam.

At the heart of an AO system is a feedback loop. It begins with a WFS that monitors the incoming optical wavefront and identifies irregularities. This information is processed by a control unit, which determines the system response. The correction is then applied using a flexible optical element, typically a DM that can be slightly deformed to counteract the distortion. This process repeats continuously, allowing the system to adapt to rapidly varying conditions (Roddier 1999).

An AO system is illustrated in Figure 3.1. It highlights the main components — wavefront sensor, control unit, and adaptive/deformable mirror — and shows how they interact in a closed-loop configuration to correct the incoming wavefront distortions in real time.

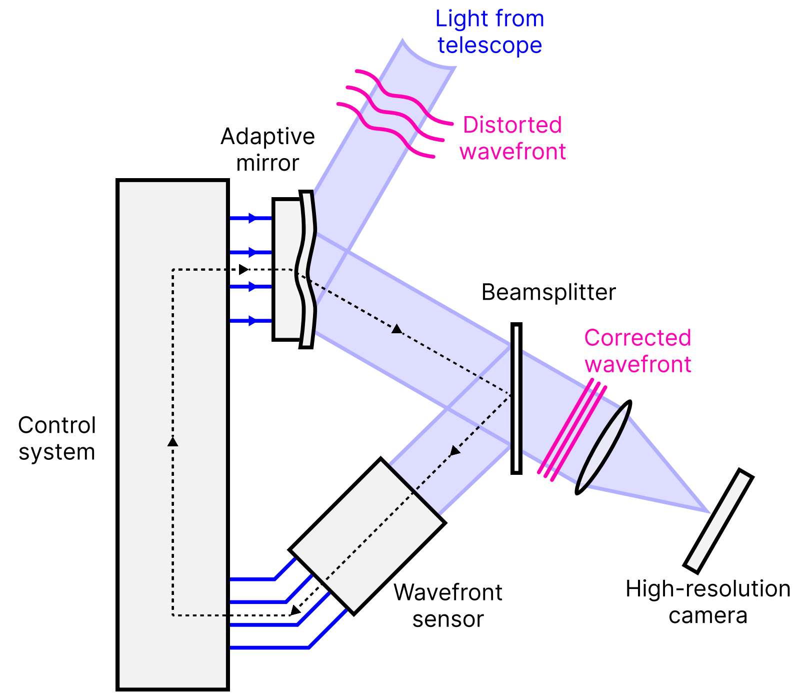

Figure 3.1: Simplified diagram of an adaptive optics system.

Originally developed for astronomical telescopes to improve image definition, the same principles are applicable to communication systems, where maintaining a narrow and stable beam is essential.

3.2 Components of an AO System

3.2.1 Wavefront Sensors

The WFS is responsible for detecting distortions in the incoming optical signal. It provides the system with real-time information about how the wavefront has been altered by atmospheric turbulence or other disturbances.

One of the most widely used types of wavefront sensors is the SH WFS, which decomposes the incoming wavefront into an array of smaller beams using a lenslet array — a grid of tiny lenses, each acting as an individual subaperture that samples a local portion of the wavefront (Platt and Shack 2001). Figure 3.2 illustrates how the grid is set in the case of a SH with 8×8 lenslets, in a Fried geometry (Steinbock 2012). The red circle illustrates the lens of the telescope, which makes invalid part of the SH lenslet/subaperture grid — the grey area, which is outside of the aperture. The blue dots represent the positioning of the DM actuators in the area. The spatial points are numerated as illustrated; this order will be relevant in the modeling of the state-space vector with the zonal phase values (this will be discussed in Section 4.1).

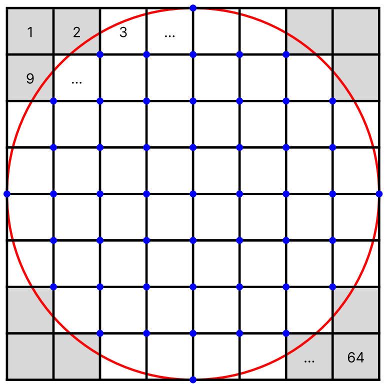

Figure 3.2: Representation of a Shack-Hartmann in a Fried geometry configuration. In this case, the SH has an 8×8 lenslet grid, which we number as exemplified in the top left. The red circle illustrates the lens of the telescope. Lenslets outside this aperture are colored in grey (invalid subapertures). The blue dots represent where the DM actuators are positioned from the perspective of the SH.

Each lens focuses its portion of the wavefront onto a detector array placed behind it. Each lenslet creates a focal spot on the detector, and the displacement of each spot carries information about the local slope of the wavefront (Platt and Shack 2001). Figure 3.3 depicts how this sensor receives the wavefront, comparing a plane wavefront with a distorted one, and how they are interpreted by the detector. By measuring these displacements — to the lenslet's center — the system can reconstruct the local slopes of each wavefront at each lenslet, and from that estimate the overall wavefront shape.

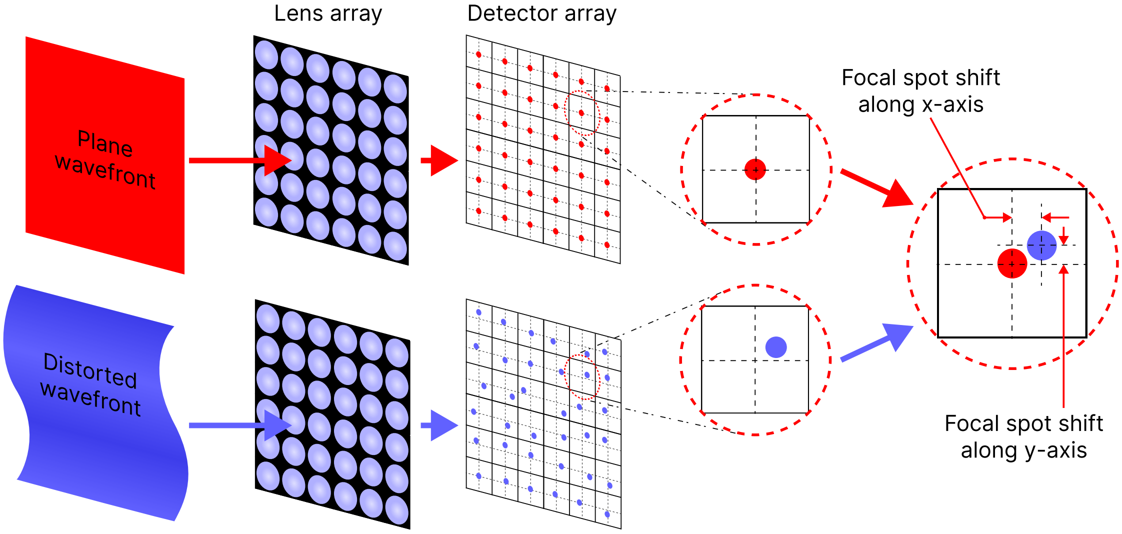

Figure 3.3: Illustration of the principle of a Shack-Hartmann wavefront sensor.

The Shack-Hartmann WFS is widely used due to its simplicity, robustness, and suitability for high-speed real-time applications such as FSOC. Furthermore, since it inherently provides local slope data at each lenslet, it aligns well with zonal wavefront reconstruction approaches — as used in this work.

An alternative method is the pyramid WFS, which offers higher sensitivity under certain conditions by splitting the beam into the pyramid's number of sides — 4 in the case of a square pyramid — and then analysing the intensity distribution (Ragazzoni 1996). However, for its inherent complexity and additional calibration required, it was not adopted in the present system.

3.2.2 Deformable Mirrors

The DM is the actuator component of the AO system. Its role is to physically reshape the optical wavefront by adjusting the surface of a mirror. Its structure is deformed by an array of discrete actuators. This correction is based on the command generated by the wavefront sensor (Roddier 1999).

Most DMs used in FSOC are based on piezoelectric actuators, which convert electrical energy into mechanical force using the piezoelectric effect — the ability of a material to generate an electric charge when stress is applied (Bera and Sarkar 2016). These actuators, placed behind the mirror surface, push or pull on specific points, deforming its surface. Figure 3.4 shows how a piezoelectric DM is structured, with the positioning of the actuators behind the mirror glass sheet.

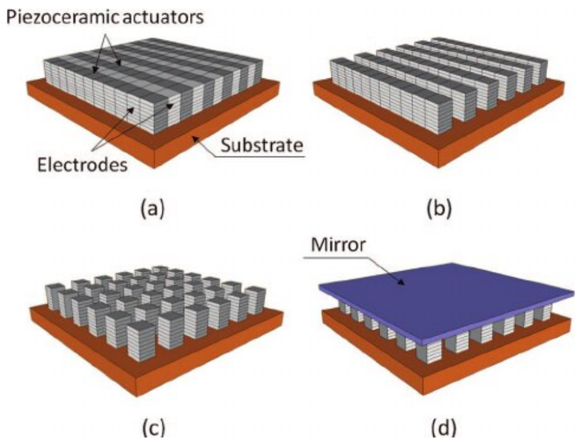

Figure 3.4: Illustration of the structure of a piezoelectric deformable mirror (Wlodarczyk et al. 2014).

The geometry of the mirror — its diameter and the number of actuators — determines how precisely it will correct the wavefront. Specifically for the same diameter, if there are more actuators there will be a more precise correction of the wavefront, but also an increase in the system's complexity and control requirements.

In FSOC, where compactness and efficiency are desired, the DM design should balance between satisfactory resolution and mechanical simplicity, still with high response frequencies.

3.2.3 Real-Time Control Loop

The real-time control loop is the core mechanism that connects the wavefront sensing and its correction. It ensures that the system continuously adapts to changing optical conditions by processing data and updating the deformable mirror accordingly.

In FSOC systems, especially those involving fast-moving LEO satellites, the optical channel changes rapidly — due to the apparent wind effect as described in Section 2.5.3. To maintain an effective correction, the control loop must operate at high update rates — over 1000 Hz. As previously shown in Figure 2.13, the temporal autocovariance of a given spatial point drops sharply with time, indicating that after a 2 ms delay between measurement and actuation, the point is effectively uncorrelated with its past value. This loss of correlation leads to dominant temporal errors, as evidenced in Figure 2.5. High-speed operation is therefore essential not only to correct turbulence effects in real time, but also to provide predictive algorithms with temporally relevant data, enabling them to forecast the wavefront evolution and further enhance correction performance.

The system is typically modeled as a feedback loop with delay, and its stability depends on the controller design, sensor noise, and actuator dynamics, Figure 3.5.

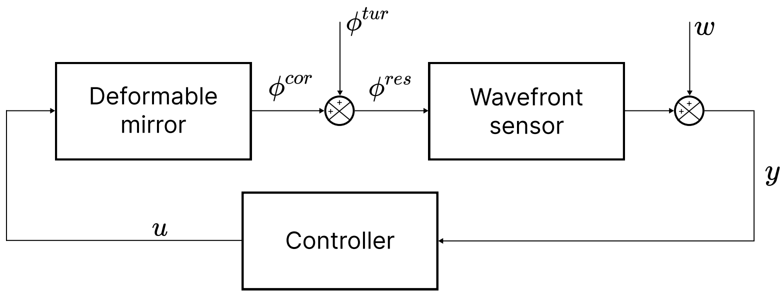

Figure 3.5: Block diagram for an AO closed-loop system in FSOC.

The WFS data is acquired and subsequently processed to generate a measurement y_k, which represents the residual wavefront ϕ^{res}_{k-1}. Based on this updated measurement, the next DM command u_{k+1} is calculated and applied as a zero-order hold over the entire control interval:

$$u_{k+1} = u(t), t \in [kT, (k+1)T[\tag{3.1}$$

When the command u_{k+1} is applied, it acts on the residual wavefront ϕ^{res}_{k+1} despite being derived from the earlier measurement y_k, which reflects ϕ^{res}_{k-1}. This introduces a two-frame delay between the wavefront correction and the corresponding measurement, which is a key contributor to the temporal error in the AO control loop.

Figure 3.6 illustrates the time frames involved in this control action, relating the moment of actuation to the frames used to predict that actuation. Highlighting the typical two-frame delay considered for most AO systems.

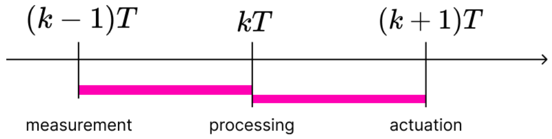

Figure 3.6: Chronogram of the adaptive optics control loop.

Temporal prediction of the wavefront addresses the delay between the measured wavefront and the actuated wavefront. By predicting the wavefront in the instant it is actuated, based on the measured data, it is expected that the temporal error will decrease. Thus, applying predictive control, either with a Kalman filter in an optimal control approach or machine learning, is necessary to achieve better wavefront correction. These control strategies will be presented and discussed in Section 3.6.

3.3 Wavefront Reconstruction

The SH WFS provides local slope measurements of the incoming optical wavefront, capturing how it has been distorted by the atmosphere. However, since these measurements represent gradients (not absolute phase), the full wavefront must be reconstructed from this data to compute the appropriate correction commands for the DM.

This is achieved through a process known as wavefront reconstruction. The key component in this process is the interaction matrix, typically obtained through system calibration. During calibration, each actuator of the DM is excited individually or in patterns, and the SHWFS response is recorded. This results in a matrix — typically denoted **M** — which describes how deformations of the mirror affect the sensor readings.

Each actuator has a corresponding influence function, which characterizes how the mirror shape changes when that actuator is activated. Because the DM surface is continuous, actuating one element often affects neighboring subapertures as well, and the stroke is limited by its surroundings; otherwise, the mirror glass could break. This interaction is captured in the interaction matrix, mapping actuator commands to WFS measurements.

During operation, the system receives a vector of slope measurements (i.e., residual wavefront error). To correct this, the inverse problem must be solved by determining the set of DM actuator commands that best cancel out the measured wavefront error. This is typically done by computing the pseudo-inverse of the interaction matrix, resulting in a reconstruction or control matrix **W**. The actuator commands are then computed as:

$$\mathbf{u}_i = \mathbf{W}\,\mathbf{y}_i \tag{3.2}$$

where $\mathbf{y}_i$ is the WFS measurement vector and $\mathbf{u}_i$ is the resulting DM command vector.

This approach assumes linearity between sensor and actuator responses, which holds well under small perturbations. However, in practice, several challenges arise — such as noisy measurements and poorly observed spatial modes. To handle this, regularization techniques (like SVD truncation or Tikhonov regularization) are often used when computing the pseudo-inverse, improving stability and preventing the system from amplifying noise.

The method described here reconstructs the wavefront in a zonal basis, where the phase is estimated at discrete subapertures — a natural match for the SHWFS output. An alternative is the modal approach, where the wavefront is decomposed into a predefined set of basis functions — like Zernike polynomials. Modal methods tend to be more robust to noise but may miss localized details.

In FSOC systems, fast and accurate wavefront reconstruction is essential for maintaining high signal quality. The zonal method, supported by efficient calibration and regularized inversion, offers a balance between spatial resolution and real-time performance — making it suitable for the predictive control strategies explored in this work.

3.4 Performance Metrics

To evaluate the effectiveness of an AO system, particularly in the demanding context of FSOC, it is essential to quantify how well the corrected wavefront approaches its ideal, undistorted form.

An important initial metric to consider is the residual wavefront error, which quantifies the root-mean-squared deviation between the measured and corrected wavefronts. This metric provides direct insight into how effectively the system is minimizing optical aberrations. Lower residual errors indicate a more accurate correction, serving as a foundational measure of system performance before evaluating its impact on communication efficiency:

$$\sigma_\phi^2 = \langle \|\phi - \phi^{cor}\|^2 \rangle \tag{3.3}$$

The Point Spread Function (PSF) describes how light intensity spreads due to diffraction when a point source is captured by a detector (Tyson and Frazier 2022). This distribution, illustrated in Figure 3.7, relies solely on the properties of the optical system. PSF serves as a tool to evaluate how the system reacts to a point source and provides insight into its optical transfer characteristics. If the system is shift invariant, the PSF can be used to predict its response to a point object.

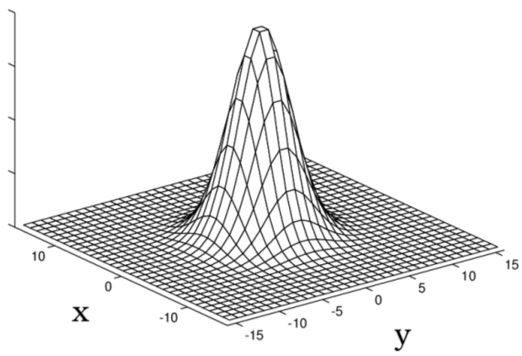

Figure 3.7: Point spread function.

Two metrics are widely used for these systems are: Ensquared Energy (EE) and the Strehl ratio (SR). These indicators offer insight into the system's optical performance after correction and are directly correlated to link quality in FSOC applications.

The Ensquared Energy measures the fraction of total beam energy contained within a specified area, typically corresponding to the receiver aperture or detector active area. It provides a spatially integrated assessment of beam quality and is useful for characterizing how well the beam is concentrated after AO correction:

$$EE = \frac{E_{\text{target}}}{E_{\text{total}}} \tag{3.4}$$

The Strehl ratio, defined as the ratio of the peak intensity of the corrected PSF to the theoretical maximum intensity. A SR near 1 indicates that the AO system has nearly fully compensated for the wavefront aberrations, while lower values reflect residual distortion (Tyson and Frazier 2022). This metric is especially sensitive to high-order aberrations and is widely used due to its straightforward interpretation:

$$SR = \frac{I_{measured}(0)}{I_{perfect}(0)} \tag{3.5}$$

In this case, since there are small variations of the residual phase variance, the SR can be related to it — using the definition of coherent energy.

$$SR = \exp(-\sigma_\phi^2)\exp(-\sigma_\chi^2) \tag{3.6}$$

In this initial study, focused on correcting phase fluctuations, the log-amplitude element of Equation (3.6) will be discarded. Instead, the SR will be estimated with the Maréchal approximation (Ross 2009):

$$SR \approx \exp(-\sigma_\phi^2) \tag{3.7}$$

Figure 3.8 illustrates the computation of the SR, comparing a PSF for the diffraction limit with a partial corrected PSF. The goal is that, after phase correction, the PSF of the source is as close as possible to the diffraction limit. In that case, the losses are minimal and the quality of the link is excellent. In FSOC practice, maintaining $SR \geq 0.3$ is generally considered necessary to sustain a reliable high-data-rate link. For a SR of 0.3 the FWHM — Full Width Half Maximum — of the diffraction-limited PSF is preserved. The FWHM is defined as the width of the PSF at half of its maximum intensity value; if it is kept constant, then it means that the fiber coupling is still efficient.

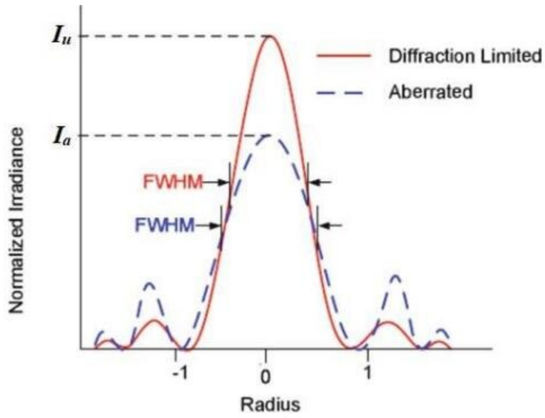

Figure 3.8: Comparison of the PSF for the diffraction limit with $SR = 1$ and a partial corrrection with $SR = 0.3$ (Jasim and Hassan 2023).

In FSOC systems where the optical signal is injected into a single-mode or few-mode fiber, the most critical performance metric is often the fiber coupling efficiency. This parameter quantifies the fraction of optical power successfully coupled into the fiber core after AO correction and directly reflects link performance. It captures the combined effects of residual wavefront errors, tip-tilt jitter, and beam wander, all of which reduce the spatial overlap between the corrected incoming wavefront and the fiber's fundamental mode (Wagner and Tomlinson 1982).

While EE and fiber coupling efficiency are commonly used to evaluate the quality of the received signal, this work selects the SR as the primary performance metric due to its direct relationship with residual phase variance and its sensitivity to improvements achievable through predictive control. By quantifying the quality of wavefront correction, the SR also serves as an indicator of improved signal reception. In the context of this thesis, the SR provides the most informative and computationally accessible link between wavefront correction accuracy and communication performance.

3.5 AO in the Context of FSOC

This thesis focuses on FSOC with LEO satellites, which orbit at altitudes between 300 km and 2,000 km. For comparison, GEO satellites are positioned approximately 35,786 km above the equator. As the propagation distance increases, the signal takes more time to travel between the satellite and the ground station; which is why LEO satellites fit better the needs of FSOC systems.

Figure 3.9 schematically illustrates a satellite's coverage area on the Earth's surface for different elevation angles. The coverage area corresponds to the portion of the Earth's surface from which the satellite is visible (Cakaj 2021). The largest circular area, shown in red, represents visibility at an elevation angle of 0°, while the smaller area, shown in magenta, corresponds to an elevation angle of 30°. This figure highlights that most of the satellite's coverage corresponds to low elevation angles (below 30°), where atmospheric turbulence and scintillation are strongest, significantly affecting optical link quality.

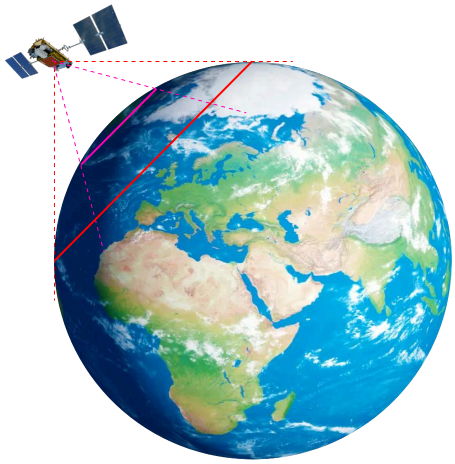

Figure 3.9: Visual representation of the area covered by a satellite at different elevation angles — red is 0° and magenta is 30°

The close proximity of LEO satellites to Earth provides several advantages. Their low altitude enables high-resolution imaging, as the shorter distance to the surface allows for finer spatial detail. LEO is also the orbit of choice for the International Space Station (ISS), enabling easier crew transport and resupply missions. Satellites in LEO travel at roughly 7.8 km/s, completing an orbit around Earth in approximately 90 minutes; consequently, the ISS circles the planet roughly 16 times per day (European Space Agency (ESA) 2020).

From a FSOC perspective, the primary benefit of LEO satellites stem from their smaller latency in communications, which is relevant for a few applications, e.g., satellite internet. Unlike GEO satellites, which must remain along the equatorial plane, LEO satellites can follow inclined orbits, providing greater flexibility in trajectory planning and network design. These features contribute to the widespread adoption of LEO for communication and Earth observation applications.

However, the relative motion of LEO satellites with respect to the Earth's surface introduces significant challenges. A ground station can observe a LEO satellite for a maximum duration of approximately 13 minutes, with roughly half of this time spent at elevations below 20°, where turbulence is stronger (Robles 2023). This necessitates the use of realistic, high-fidelity turbulence models, high-speed AO systems, and predictive control strategies to maintain link performance.

As discussed in Section 2.5.2, the evolution of atmospheric turbulence is governed by the frozen flow hypothesis, in which turbulence layers move with the local wind. During satellite tracking, maintaining a fixed line of sight is equivalent to translating the turbulent layers relative to the observer, giving rise to the so-called apparent wind (see Section 2.5.3). The apparent wind is typically an order of magnitude greater than the natural wind, accelerating the temporal evolution of turbulence and increasing the temporal error in AO correction. Mitigating this error requires either increasing the AO loop frequency or implementing predictive control algorithms capable of compensating for the rapidly evolving wavefront distortions.

3.6 Control Strategies for Adaptive Optics

In AO, control strategies are crucial for compensating the rapidly evolving wavefront distortions induced by atmospheric turbulence. Conventional controllers, such as simple integrators, are limited by their lack of predictive capability, which results in temporal lag errors. Predictive control strategies overcome this limitation by estimating the future state of the wavefront and applying corrections in advance.

Historically, AO systems relied on integral-action controllers, often tuned using the Optimal Modal Gain Integrator (OMGI) method (Gendron and Lena 1994; Dessenne et al. 1998). The OMGI assigns an optimal gain to each mode of the AO system, adapting the controller response to the turbulence characteristics.

Among predictive methods, the LQG controller is the most established and widely adopted in astronomical AO. By combining a state-space model with Kalman filtering, the LQG controller provides optimal next-step predictions using a minimal set of turbulence descriptors, typically Fried's parameter and wind velocity. Its performance has been validated across numerous on-sky experiments under a wide range of turbulence conditions (Kulcsár et al. 2006; Sivo et al. 2014; ONERA 2024).

Machine learning (ML) methods provide an alternative by learning turbulence dynamics directly from observational data without requiring explicit parameterization. Techniques such as deep neural networks have shown promising predictive performance in simulations, particularly under highly variable or poorly characterized turbulence (Liu et al. 2020). However, ML-based controllers often require extensive training data, lack formal stability guarantees, and their performance can degrade outside the training distribution (Swanson et al. 2021). In contrast, LQG offers a fully model-based, theoretically grounded framework with predictable behavior across a wide range of turbulence conditions.

A comparative study by Robles et al. (2022) demonstrated that even at lower operational frequencies, LQG outperforms OMGI, achieving roughly twice the Strehl ratio and superior fiber coupling efficiency. Moreover, Dray et al. (2024) showed that for FSOC AO systems, which demand both rapid response and robustness to changing conditions, LQG performance is comparable to state-of-the-art ML approaches, while maintaining a structured and transparent design process.

Given its proven effectiveness, well-understood tuning methodology, and compatibility with the objectives of this work, the LQG controller is adopted as the predictive control framework for this study. Its predictive capabilities enable effective mitigation of temporal lag errors, making it particularly suited for FSOC AO applications where high-speed, reliable wavefront correction is critical.

3.7 Summary

This chapter presents the principles of AO, its components, and how they interact. Once more, attending for the temporal delay between measurement and actuation, which leads to temporal lag error, and how a promising way to mitigate it is with predictive control.

This study will be based on Fried's geometry, so the reconstruction of the wavefront from the SHWFS matches the zonal approach of the wavefront.

Regarding the control unit, which constitutes the core focus of this study, particular attention is given to temporal decorrelation. For a delay of 2 ms, the temporal autocovariance function indicates that a spatial point loses correlation with itself. In a control system without prediction, operating at 1000 Hz, this corresponds to the expected delay between measurement and actuation. To mitigate this delay, possible strategies include increasing the sampling frequency of the AO system by employing higher-performance hardware, and/or integrating a predictive controller.

The performance metrics are established to evaluate the predictive capability of the selected models in mitigating temporal error. The notion of PSF is relevant to distinguish between the diffraction-limited wavefront in the absence of disturbances and the real wavefront affected by atmospheric turbulence. The comparison between the two of them is given by the SR, the primary metric of this study. Its calculation, in this study, is done via the Maréchal approximation, and a SR of 0.3 or higher is required to sustain a reliable high-data-rate link; at this value, the FWHM of the diffraction-limited PSF is still largely preserved.

In FSOC systems the optical signal is then injected into a fiber, so a critical metric is the fiber coupling efficiency. However, this study concentrates on the ability of predictive control to mitigate temporal errors by aligning the predicted wavefront with the actual wavefront. Therefore, the analysis will focus exclusively on the SR as the performance metric.

Lastly, a comparative analysis was done between control strategies previously employed in AO systems. The traditional OMGI solution is discarded for its lack of predictive capability, which has been proven to be outperformed by an LQG approach by Robles (2023). While both the LQG and state-of-the-art ML approaches have demonstrated similar effectiveness in mitigating turbulence effects, the LQG framework was ultimately chosen for the high fidelity of atmospheric turbulence models and its on-sky validation in enabling two-way communication with LEO satellites.

Chapter 4

Model-Based Predictive Control Strategies for Adaptive Optics

In the previous chapters, the effects of atmospheric turbulence were presented, AO was shown to be a promising technique to enable fast-paced wavefront correction, some control options were evaluated, and it was decided to study an optimal controller. With this in mind, this chapter introduces the conditions and principles required for this type of predictive controller.

This chapter develops the theoretical background of model-based optimal predictive control applied to AO systems, focusing on how atmospheric dynamics can be modeled, predicted, and compensated in real time. It builds on the physical and system-level insights from previous chapters, transitioning toward control design.

4.1 State-Space Model for Control Design

The dynamics of the AO system are translated into a mathematical representation suitable for optimal control synthesis. In this framework, the state-space approach captures the wavefront evolution and control actions over time using discrete-time linear systems.

A typical formulation is Equation (4.1), where x_k represents the system state, u_k the actuator commands, y_k the sensor measures, w_k the process noise, and v_k the measurement noise. While A, B, C, and D are matrices describing the system.

$$\begin{aligned} x_{k+1} &= Ax_k + Bu_k + w_k \\ y_k &= Cx_k + Du_k + v_k \end{aligned} \tag{4.1}$$

In the case of AO, the state vector $x_k \in \mathbb{R}^n$ represents the zonal phase values or modal coefficients — in this case the zonal phase values. The matrix $A \in \mathbb{R}^{n\times n}$ captures the temporal evolution of the atmospheric phase, and its estimation is discussed in Section 4.3.2. $B \in \mathbb{R}^{n\times m}$ maps the DM commands $u_k \in \mathbb{R}^m$ to apply corrections in the state space x_k—in a zonal representation, it models how actuator commands deform the phase screen across the pupil. $C \in \mathbb{R}^{p\times n}$ models how the WFS observes the state, and $D \in \mathbb{R}^{p \times m}$ captures direct feedthrough from control commands, which is often negligible in AO systems.

This state-space formulation is particularly suitable for designing optimal controllers such as LQG, which combines a Kalman predictor with a Linear Quadratic Regulator (LQR) to handle both process and measurement noise.

4.2 Predictive Controller with *LQG* Framework

This section presents the LQG controller as a predictive control strategy tailored to AO systems, originally developed by Paschall and Anderson (1993). The LQG framework integrates optimal control and state estimation to compensate for atmospheric turbulence in real time (Sivo et al. 2014).

The LQG controller combines two foundational tools from control theory: the LQR, which provides the optimal control input to minimize a predefined quadratic cost, and the Kalman filter, which estimates the internal system state from noisy sensor measurements (Anderson and Moore 2007; Kulcsár et al. 2006). In this configuration, the LQR assumes full state availability, while the Kalman filter reconstructs the unmeasured or noisy state, enabling the controller to act predictively. This separation principle allows for optimal regulation of stochastic systems, such as those governed by turbulent wavefronts in AO.

Figure 4.1 illustrates the block diagram of an LQG controller applied to an AO system. The Kalman filter estimates the current and future wavefront states based on noisy measurements from the wavefront sensor. These estimates are then used by the LQR to compute the optimal control action, which is applied to the AO system — via the DM.

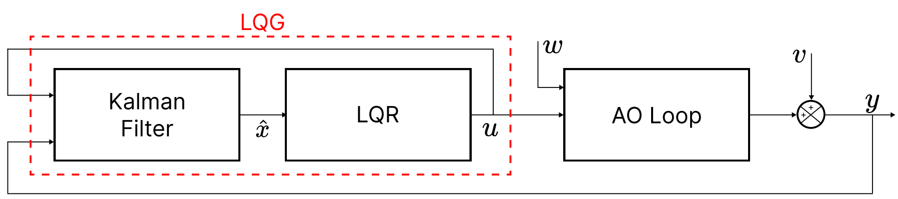

Figure 4.1: Block diagram of an LQG controller applied to an AO system.

In AO applications, the control objective typically involves minimizing the residual phase variance, which is closely related to the SR, as discussed in Section 3.4. The controller aims to anticipate future wavefront distortions based on the estimated atmospheric dynamics and apply corrective actions before they reach the wavefront sensor. By reducing the residual phase variance as much as possible, the system can achieve a higher SR, which translates into better wavefront correction and a higher-quality received signal.

4.2.1 Optimal Linear Quadratic Regulator (*LQR*)

The LQR component addresses the problem of finding the optimal sequence of control inputs $\mathbf{u}_k$ that minimizes the long-term cost associated with state deviations and control effort. For a discrete-time system, this is defined as:

$$J(u) = \lim_{M\to\infty} \frac{1}{M} \sum_{k=0}^{M-1} \left(x_k^\top Q x_k + u_k^\top R u_k \right) \tag{4.2}$$

where Q and R are weighting matrices that encode the relative importance of state error and control energy, and M is the time horizon over which the average cost is computed.

In the context of AO, the cost function can be tailored to minimize the variance of the residual phase ϕ_{k+1}^{res} that remains uncorrected by the DM, that is directly linked to maximizing the SR (Herrmann 1992), which enhances image quality, and is also associated with better fiber coupling performance (Canuet et al. 2017). This leads to a simplified quadratic criterion (Kulcsár et al. 2006; Kulcsár et al. 2012):

$$J(u) = \lim_{M\to\infty} \frac{1}{M} \sum_{k=0}^{M-1} \left\| \phi_{k+1}^{res} \right\|^2 \tag{4.3}$$

where ϕ_{k+1}^{res} denotes the residual phase after correction at time step $k+1$.

The optimal control input is computed based on the estimated future state, which allows the controller to act with predictive capabilities. In combination with the Kalman filter, this approach forms a closed-loop predictor-corrector architecture that is particularly well-suited to dynamic and noisy environments such as atmospheric turbulence.

4.2.2 Kalman Filter

The LQG obtains optimal correction if there is optimal estimation of the states from the available measurements using a Kalman filter (Simon 2006). The estimation process is carried out in two main steps: a measurement update, where new observations are assimilated, and a time update, which predicts the future state based on the system model. The discrete-time formulation is as follows:

$$\hat{x}_{k|k} = H \left(y_k - C\hat{x}_{k|k-1} - Du_{k-1} \right) \tag{4.4}$$

$$\hat{x}_{k+1|k} = A\hat{x}_{k|k} \tag{4.5}$$

Equation (4.4) corresponds to an update of the estimation using the last measurement available. The term inside the parentheses is called the innovation. It represents the difference between the actual measurement y_k and the predicted measurement y_{k-1} based on the prior state estimate. Equation 4.5 then propagates the updated state estimate forward in time using the system dynamics, matrix A.

H, the Kalman gain matrix can be computed as an asymptotic solution of the discrete algebraic Riccati equation. It depends on the state-space matrices, the covariance matrix of the process noise Σ_v, and the covariance matrix of the measurement noise Σ_w. These are assumed to be zero-mean white Gaussian processes with $\Sigma_{v,w} = 0$.

In AO applications, the estimated state $\hat{x}_{k|k}$ typically encodes the current turbulent wavefront and its temporal evolution. This estimate is then used by the LQR to compute the optimal control input $\mathbf{u}_k$, resulting in a closed-loop LQG controller capable of both filtering and predicting the atmospheric disturbance.

4.2.3 Summary of the *LQG* Predictive Controller

The LQG controller offers a principled and powerful framework for predictive control in AO systems. By integrating a LQR with a Kalman filter, the controller simultaneously addresses optimal actuation and robust state estimation under stochastic disturbances. Its structure naturally lends itself to real-time correction of atmospheric turbulence, a key challenge in FSOC systems.

In this chapter, the theoretical formulation of the LQG has been adapted to minimize the residual phase variance — an objective directly tied to communication signal integrity. Meanwhile, the Kalman filter serves as the predictive engine, leveraging system dynamics and noisy measurements to reconstruct and forecast wavefront evolution.

However, the performance of the Kalman filter is intrinsically dependent on the fidelity of the underlying dynamic model. In the context of atmospheric turbulence, this involves modeling the temporal evolution of the wavefront using stochastic processes. Therefore, the predictive capacity of the LQG controller hinges on how accurately these temporal dynamics are captured. This motivates the present study's focus on quantifying performance through metrics such as the SR and the temporal lag error, which directly reflect the effectiveness of wavefront prediction and correction.

4.3 Temporal Prediction Models for AO

Predictive controllers are expected to reduce the temporal error, since they calculate the AO correction from a prediction of the future wavefront, rather than using the last available measurement. (Jackson et al. 2015)

Predictive controllers use a model based on the spatio-temporal statistics of turbulence. Many works have been carried out focusing on the search for a model that can provide good prediction performance, is computationally efficient, and is easily identifiable from available AO telemetry (Jackson et al. 2015; Sivo et al. 2014; Kulcsár et al. 2006). However, most of these studies focused on AO for astronomy, which works at around 500 Hz in a stable position. It is therefore necessary to validate whether these conclusions still apply to FSOC systems, which operate at higher frequencies, typically between 1000 and 5000 Hz (Robles 2023). In rapidly varying conditions, such as the strong apparent wind often encountered in FSOC, the temporal error becomes significantly larger, further motivating the use of predictive control.

4.3.1 Autoregressive Predictive Models

Predicting atmospheric turbulence in time relies on the idea that its behavior can be described by its statistical properties over time — most commonly, the temporal covariance. A common approach to model such behavior is through autoregressive models, which estimate the current state based on a weighted combination of its previous values.

When extended to multiple signals, AR models take the form of vector autoregressive (VAR) models, which not only capture the temporal evolution of each point but also the relationships between them. In the context of AO, this is particularly useful for modeling the simultaneous behavior of wavefront values at different points across the pupil, especially when using a zonal (grid-based) representation (Jackson et al. 2015).

The turbulent phase in the telescope pupil is assumed to be represented by a weakly stationary discrete time series $\{x_k\}_k$, where x_k is a state vector representing the turbulent phase ϕ_k at a given time step k.

An AR model of order p — or AR(p) — assumes that the future state of the process can be estimated as a weighted sum of its past p values:

$$x_{k+1} = \sum_{i=1}^{p} a_i x_{k-i+1} + \upsilon_k \tag{4.6}$$

This means that the future state is predicted using a linear combination of the previous p states using the coefficients a_i, and υ_k an additive white Gaussian noise component that ensures the conservation of energy in the process. In a zonal approach, each spatial point of the pupil evolves independently, being influenced only by its own past values — depending on the order of the AR model — without influence of its neighboring points. Figure 4.2 illustrates this influence in a single point, in a first order AR model.

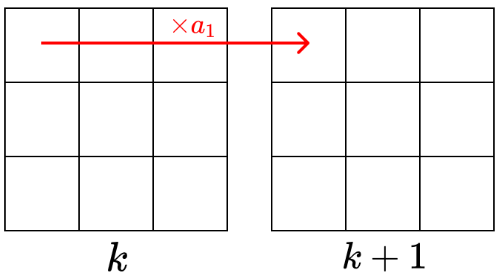

Figure 4.2: Illustration of an AR(1) model in a zonal representation, the future phase value at point (1,1) is predicted solely from its own past value at time k, weighted by coefficient a_1.

However, based on the frozen flow hypothesis — which states that the temporal evolution of the phase screen results from its displacement by the wind — the future value of the phase at each spatial point is strongly influenced by the values of its neighboring points at the current time step. This is because the phase pattern is transported across the pupil along the wind direction, meaning that each point at time $k+1$ tends to inherit the phase from an upstream neighbor at time k.

This spatial interaction is captured by VAR models of order p, or VAR(p), which allows each point to also be influenced by the history of other points in the pupil.

The VAR(p) model can be written as:

$$\mathbf{x}_{k+1} = \sum_{i=1}^{p} \mathbf{A}_i \mathbf{x}_{k-i+1} + \upsilon_k \tag{4.7}$$

where $\mathbf{x}_k$ is a state vector containing the phase values at N spatial points at time step k, $\mathbf{A}_i \in \mathbb{R}^{N\times N}$ are the coefficient matrices that encode how each point is influenced by all other points, and υ_k is a zero mean white Gaussian noise vector.

The spatio-temporal coupling is captured by the temporal covariance matrices, which quantify the statistical dependencies between points across time. Figure 4.3 illustrates this influence on a single point in a first-order VAR model.

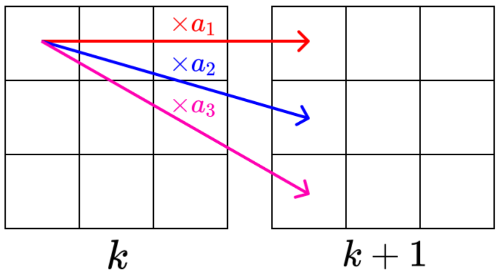

Figure 4.3: Illustration of a VAR(1) model in a zonal representation, the influence of point (1,1) at time k weighted by coefficients a_1, a_2 and a_3 at time $k+1$.

Figure 4.4 presents the spatial phase covariance matrix, which translates the correlation between spatial points based on the distance between them, from Equation (2.15). In this example, for a square pupil with dimensions of 8×8 points. The spatial separations between points occur repeatedly, meaning that any two points with the same separation have the same spatial covariance. For zero separation — a point with itself — the covariance reaches its maximum, equal to the phase variance. To understand this figure, both axes represent the spatial points indices according to their distribution in the pupil, represented in Figure 3.3.

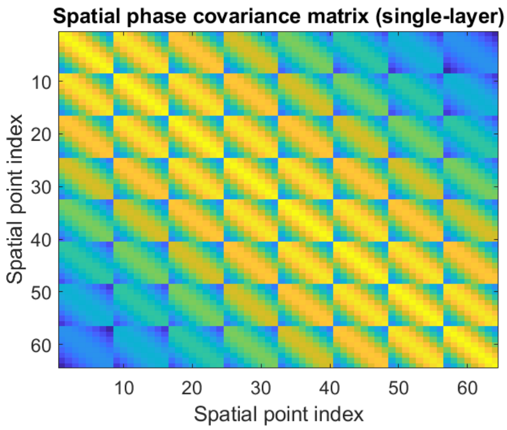

Figure 4.4: Chart representing the spatial phase covariance matrix for a single-layer atmosphere, computed on a square pupil sampled with 8×8 points, illustrating the spatial correlation of phase distortions across the aperture. Yellow indicates higher covariance, while blue represents lower covariance.

This spatial covariance information serves as the foundation for identifying the parameters of the AR models, which are subsequently used to predict the temporal evolution of the wavefront and enable predictive control in the AO system.

For a first order VAR model, the evolution of the phase screen — represented as a grid in Figure 4.5 — follows the frozen flow hypothesis, meaning that for high-frequency systems the turbulence pattern is transported across the aperture by the wind. In the illustration, the red grid denotes the baseline phase screen, while the black grids correspond to the same screen observed at increasing time lags, and the blue grid is its previous state. This representation highlights the variance between two realizations of the wavefront phase separated by a temporal lag.

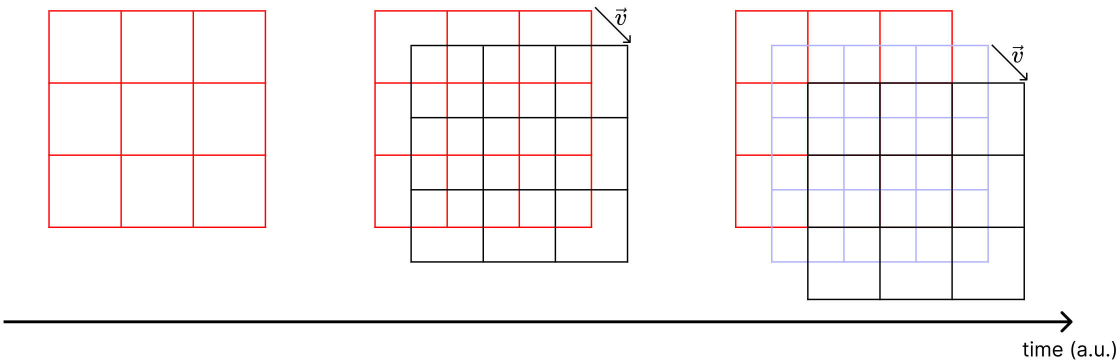

Figure 4.5: Diagram exemplifying the temporal evolution of a phase screen modeled with a VAR(1) process, showing the wind-driven translation of a phase screen across the aperture. The red grid represents the initial phase screen, and the black grid shows its time-shifted counterpart, illustrating the wind-driven motion across the aperture.

As the black grid is carried by the wind, the variance between the two realizations increases until it reaches a maximum when the grids are misaligned by approximately half a spatial period (middle panel). With further translation, the black grid eventually overlaps the red one again, at which point the variance decreases.

For the case of a second-order VAR model, illustrated in Figure 4.6, the same wind-driven translation occurs, but the black grid overlaps the baseline grids — pink and red grids — with twice the frequency compared to the VAR(1) case. As a result, the oscillation of variance increase and decrease occurs twice within the same interval, whereas it happens only once for a VAR(1) model.

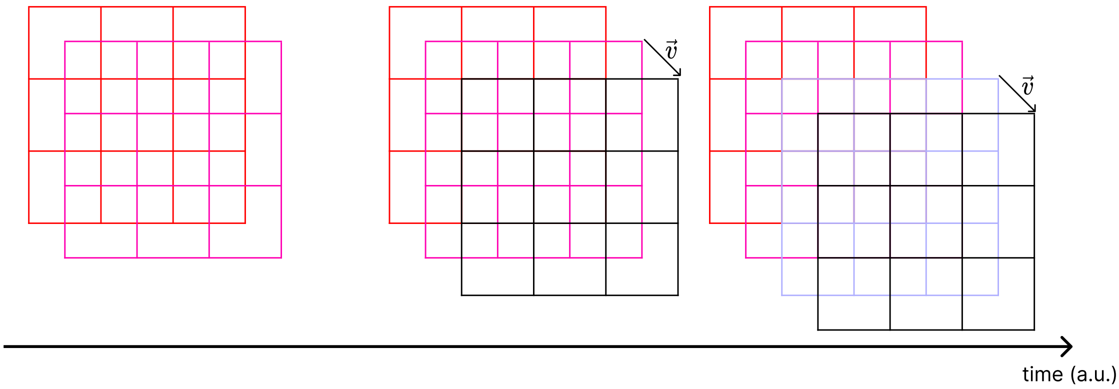

Figure 4.6: Diagram exemplifying the temporal evolution of a phase screen modeled with a VAR(2) process, showing the wind-driven translation of a phase screen across the aperture. The red and pink grid represents the initial phase screens, and the black grid shows its time-shifted counterpart, illustrating the wind-driven motion across the aperture.

This illustrates that, in the case of VAR models, larger lags do not necessarily correspond to larger variance between the predicted and the actual wavefront. Because these models are vectorial and exploit more information in the prediction, the residual variance is distributed across multiple lagged dependencies rather than increasing monotonically with lag. This behavior is a characteristic of VAR models and will be revisited later in the discussion of the results (Chapter 5).

4.3.2 Data-driven Autoregressive Model Identification

To use an autoregressive — either AR or VAR — model for temporal prediction, it is necessary to determine its parameters — that is, the coefficients that define how the current state depends on previous states. This process is known as model identification.

Model identification consists of estimating these coefficients from available data — in this case, AO telemetry — such that the model reproduces the statistical dynamics of the system with minimal prediction error — further discussed in Chapter 5, which evaluates prediction accuracy. In the context of AO, this involves analyzing time series of wavefront measurements and computing the best-fit model parameters based on assumptions such as stationarity and linearity (Lütkepohl 2005).

Several methods can be used for this purpose, each with different trade-offs in terms of complexity, computational cost, and ability to exploit spatial and temporal correlations. The most relevant methods considered in AO applications are presented in the following subsections.

In this study, the Yule-Walker equations — presented in Yule (1927) and Walker (1931) — relate the AR coefficients to the covariance structure of the process, with the formulation differing between the scalar AR case and the VAR case.

4.3.2.1 Scalar AR Yule-Walker Estimator

For an AR model of order p, the process at spatial point i can be written as:

$$\phi_{i,k+1} = \sum_{j=1}^{p} a_{i,j}\phi_{i,k-j+1} + \varepsilon_{i,k} \tag{4.8}$$

where $a_{i,j}$ are the AR coefficients to be estimated, and $\varepsilon_{i,k}$ is assumed to be zero-mean, white noise.

The Yule-Walker equations relate these coefficients to the autocovariances, for each point i can be written in matrix form as:

$$\underbrace{\begin{bmatrix} \gamma_i(0) & \gamma_i(1) & \cdots & \gamma_i(p-1) \\ \gamma_i(1) & \gamma_i(0) & \cdots & \gamma_i(p-2) \\ \vdots & \vdots & \ddots & \vdots \\ \gamma_i(p-1) & \gamma_i(p-2) & \cdots & \gamma_i(0) \end{bmatrix}}_{\Gamma_i \in \mathbb{R}^{p\times p}} \underbrace{\begin{bmatrix} a_{i,1} \\ a_{i,2} \\ \vdots \\ a_{i,p} \end{bmatrix}}_{\mathbf{a}_i} = \underbrace{\begin{bmatrix} \gamma_i(1) \\ \gamma_i(2) \\ \vdots \\ \gamma_i(p) \end{bmatrix}}_{\gamma_i} \tag{4.9}$$

where $\gamma_i(\ell) = \langle \phi_{i,k}\phi_{i,k-\ell} \rangle$ is the temporal autocovariance at lag $\ell = 0, 1, ..., p$, of a point i.

The AR coefficients are obtained by solving:

$$\mathbf{a}_i = \Gamma_i^{-1}\gamma_i \tag{4.10}$$

For a AR(2) Yule-Walker system at point i:

$$\begin{bmatrix} a_{i,1} \\ a_{i,2} \end{bmatrix} = \begin{bmatrix} \gamma_i(0) & \gamma_i(1) \\ \gamma_i(1) & \gamma_i(0) \end{bmatrix}^{-1} \begin{bmatrix} \gamma_i(1) \\ \gamma_i(2) \end{bmatrix} \tag{4.11}$$

This is a point-wise method that is attractive because it is fast, simple, and does not require iterative optimization. However, it assumes that the process is stationary and that the data used for estimation is not too noisy. In practical terms, it works well when there is enough telemetry to capture the underlying statistics of the turbulence.

Moreover, the method naturally extends to arbitrarily high AR orders p, and VAR models, providing greater flexibility to model complex temporal dependencies.

4.3.2.2 VAR Yule-Walker Estimator

The scalar AR method treats each point separately — it predicts AR models' coefficients — while the VAR treats the entire wavefront phase vector as a whole. This implies that the prediction at each point depends not only on its own past values but also on the past values of all other spatial points. (Conan et al. 2023; Jackson et al. 2015)

A VAR model of order p to represent the wavefront phase vector at time t can be written as:

$$\phi_{k+1} = \sum_{j=1}^{p} \mathbf{A}_k \phi_{k-j+1} + \varepsilon_k \tag{4.12}$$

where $\phi_k \in \mathbb{R}^N$, N is the number of spatial points, each $\mathbf{A}_k$ is an $N \times N$ matrix of coefficients that models the influence of the wavefront at lag k on the current time, and $\varepsilon(t)$ is a noise vector —assumed white and Gaussian.

Under the assumption of stationarity, the coefficient matrices $\mathbf{A}_k$ can be obtained by solving the block Yule-Walker equations:

$$\begin{bmatrix}\mathbf{A}_1\mathbf{A}_2\cdots\mathbf{A}_p\end{bmatrix} = \begin{bmatrix}\Sigma_1\Sigma_2\cdots\Sigma_p\end{bmatrix} \begin{bmatrix}\Sigma_0 & \cdots & \Sigma_{p-1} \\ \vdots & \ddots & \vdots \\ \Sigma_{p-1}^\top & \cdots & \Sigma_0\end{bmatrix}^{-1} \tag{4.13}$$

where $\Sigma_\ell = \langle \phi_{k+\ell}\phi_k^\top \rangle$ denotes the temporal autocovariance matrices with lag index $\ell = 0, 1, 2, ..., p$.

For a VAR(1) model:

$$A_1 = \Sigma_1 \Sigma_0^{-1} \tag{4.14}$$

where $\Sigma_0 = \langle \phi_k \phi_k^\top \rangle$ is the autocovariance matrix, $\Sigma_1 = \langle \phi_{k+1}\phi_k^\top \rangle$ is the lag-1 covariance matrix.

For a VAR(2) model:

$$\begin{bmatrix}\mathbf{A}_1\mathbf{A}_2\end{bmatrix} = \begin{bmatrix}\Sigma_1\Sigma_2\end{bmatrix} \begin{bmatrix}\Sigma_0 & \Sigma_1 \\ \Sigma_1^\top & \Sigma_0\end{bmatrix}^{-1} \tag{4.15}$$

where $\Sigma_\ell = \langle \phi_{k+\ell}\phi_k^\top \rangle$ are the lag-ℓ covariance matrices.

Compared to point wise AR-based predictor, VAR prediction is more robust in the presence of spatial correlations and is expected to significantly reduce prediction error when these correlations are strong. This makes it particularly effective for applications such as tomographic AO, where the phase at each point is influenced by large-scale wavefront structures.

4.3.2.3 Summary and Discussion of Identification Models

The Yule–Walker method uses the temporal autocovariance of a stationary process to determine the coefficients of AR models. Its multivariate extension generalizes this approach to VAR models by incorporating cross-covariances between the vector components.

For AR models, where each spatial point is treated independently. In other words, the prediction at each point is based solely on its own past values, without accounting for spatial correlations. It relies on the temporal autocovariance function.

In contrast, the VAR method models the entire wavefront as a single vector, enabling the prediction at each point to depend not only on its own history but also on the past values of neighboring points. This VAR formulation allows to exploit both spatial and temporal correlations. As a result, improved performance is expected — particularly in systems governed by the frozen flow hypothesis, which assumes that the atmosphere evolves primarily through translational motion. This assumption inherently links spatial structure to temporal evolution, making VAR models particularly suitable for predictive control in AO.

These predictors have already been studied in the context of astronomical AO, which motivates the analysis of their performance for FSOC systems.

Figure 4.7 reproduces the results presented by Jackson et al. (2015), showing the theoretical temporal lag errors under AO correction for different prediction strategies.

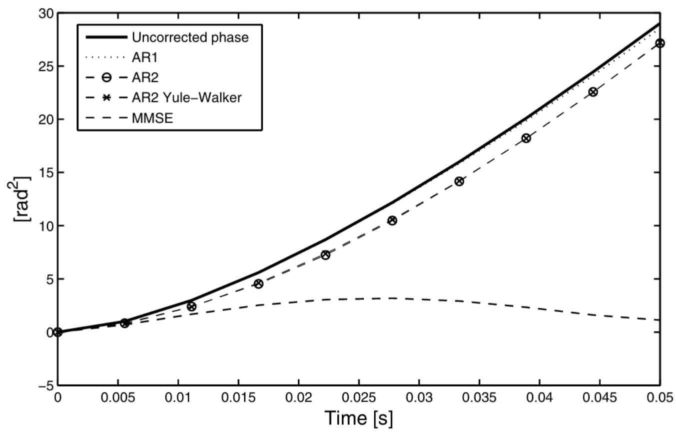

Figure 4.7: Theoretical temporallag errors under AO for astronomy conditions (Jackson et al. 2015).

In that study, the AR-based models showed only marginal improvement over the no-prediction case, primarily for longer system delays. Their performance degraded significantly as the lag increased, indicating limited robustness to temporal delays.

In contrast, the MMSE predictor — equivalent to the VAR(1) model — maintains a stable performance profile. Although a slight peak in prediction error is observed — for the motives explained in Section 4.3.1—, its overall structure remains relatively flat across different lags. This suggests that the VAR(1) predictor is more robust to increasing system delays, making it a promising strategy for FSOC.

These models assume linear dynamics and statistical stationarity, which may be violated under rapidly changing turbulence profiles in FSOC applications. When tested in the context of FSOC systems, only the AR(2) Yule-Walker model, and the VAR(1) outperformed the uncorrected phase baseline. Consequently, the simpler AR(1) and AR(2) models are not considered in this thesis. These fail under smaller temporal lags.

Although higher-order AR and VAR models can capture additional temporal dynamics, they substantially increase the number of parameters to estimate, particularly under limited training data or time-varying turbulence conditions. Previous studies have shown that most predictive information is already captured by first- and second-order models (Gendron and Lena 1994; Jackson et al. 2015). Therefore, this work focuses on the AR(2) Yule-Walker model, as well as VAR(1) and VAR(2) models. Consistently, Robles (2023) reported that performance gains for VAR models beyond second order are negligible. These models will be tested in the context of their ability to improve prediction quality within the LQG framework, with particular attention to their impact on the temporal lag error of the phase and SR across different simulation conditions.

4.4 Summary

This chapter describes how the problem is formulated in state-space, where the system dynamics between the different components are represented, and the interaction of noise with the system is captured.

The LQG framework is introduced, a framework that integrates optimal control and state estimation. In this case, the optimal controller, the LQR, aims to minimize the residual phase after correction, and the Kalman filter is responsible for state estimation. This work is focused in improving the state estimation by using AR and VAR models. Model identification for these approaches is carried out using the Yule-Walker equations, which estimate future states based on the statistical properties of past states, in both scalar and vectorial formulations.

Lastly, a comparative discussion between the AR models previously applied to astronomy AO by Jackson et al. (2015), how AR(2) Yule-Walker and VAR(1) are two promising options for FSOC. Since the VAR(1) model is the most promising for astronomical AO, it motivates the elevation of the VAR model order to see if the wavefront correction benefits from it. The model order is limited to second order to maintain simplicity and reduce computational cost. Accordingly, this study considers the AR(2) Yule-Walker model, as well as VAR(1) and VAR(2) formulations.

Chapter 5 evaluates these models under various simulation conditions, assessing their ability to mitigate the residual phase of the received wavefront at the ground station. Performance is quantified through a prediction gain analysis for *LISA* and *FEELINGS*. The influence of both hardware and atmospheric parameters is examined, and robustness tests of the prediction models are performed with respect to the estimated atmospheric parameters.

Chapter 5

Evaluation and Comparative Analysis

This chapter reports the simulation methodology, a case study to different FSOC simulation environments, a gain analysis to the predictive models under study, and a sensitivity analysis of the predictive models to the simulated parameters. The goal is to assess the performance of the various temporal estimators presented in Chapter 4 under realistic FSOC conditions.

5.1 Simulation Methodology

The simulation experiments were carried out in MATLAB. It was chosen for its familiarity, widespread use in scientific computing, its extensive library of toolboxes, mainly OOMAO (Object-Oriented MATLAB Adaptive Optics) toolbox.

OOMAO, developed by Conan and Correia (2014), is an object-oriented toolbox for AO systems. It is based on a set of classes which represent the light source, atmosphere, telescope, WFS, DM, and an imager of an AO system. These classes are assembled to perform the numerical modeling of the AO system, used to simulate the propagation of the wavefront through the system and to update object properties.

It supports both modal and zonal modeling approaches. This work uses the zonal approach, where the wavefront is described on a grid of discrete spatial points, making it compatible with the toolbox. Additionally, OOMAO includes a library of theoretical tools to analyze atmospheric turbulence and wavefront statistics — essential features for deriving and testing the predictive models used in this study.

The framework models an AO system operating in closed-loop, incorporating a SH WFS, a DM with matched actuator geometry, temporal sampling, and servo delay modeling, and a turbulence generator based on the frozen flow hypothesis.

To replicate FSOC conditions, the simulations deviate from typical astronomical parameters. Table 5.1 presents simulation parameters used in previous studies of AO for astronomical purposes.

Table 5.1: Representative parameters from astronomical AO systems

Name	Keck NGS AO	Gemini Altair	Subaru AO	SCExAO	Units
Telescope diameter, D	10	8	8	8	m
Wavelength, λ	1.58	1.6	0.8-2.5	1.0-2.5	µm
Sampling frequency, f_s	500-672	600-1000	100-500	1000-1700	Hz
SH subpupils	20×20	12×12	-	-	-

These systems typically operate on 8-10 m diameter telescopes with loop frequencies ranging from 500 to 1700 Hz, and SH wavefront sensors from 12×12 to 20×20 subapertures. These configurations are optimized for faint astronomical targets and relatively stable seeing (Dam et al. 2004; Christou et al. 2010; Minowa et al. 2010; Jovanovic et al. 2015).

Unlike astronomical observation systems, which point toward fixed celestial targets, FSOC systems must continuously track satellites in orbit to maintain the optical link (see Section 3.5). This dynamic pointing requirement introduces additional complexity to the system, as the relative motion between the satellite and the ground station affects alignment, turbulence interaction, and control latency, as well as the apparent wind effect (see Section 2.5.3).

Therefore, to realistically simulate a FSOC system, specific design constraints must be considered. These include using a smaller telescope diameter to allow agile tracking of fast-moving satellites, selecting a wavelength in the IR spectrum due to lower atmospheric attenuation, and adopting a higher sampling frequency to cope with the rapid temporal variations introduced by atmospheric turbulence and satellite motion.

Table 5.2 shows the AO relevant parameters for two different systems, the *LISA* — a compact AO bench for telecommunications developed by *ONERA* — and *FEELINGS* — the *ONERA* optical communications ground station. These parameters will serve as the baseline configuration for the simulations (Giggenbach et al. 2022; Phung et al. 2021; Cyril et al. 2022).

Table 5.2: Representative parameters from FSOC AO systems

Name	*LISA*	*FEELINGS*	Units
Telescope diameter	0.4	0.6	m
Wavelength, λ	1.55	1.55	µm
Loop sampling frequency, f_s	2000	4500	Hz
SH subpupils	8×8	16×16	-

To properly evaluate the performance of predictive control strategies, it is important to test both single-layer and multi-layer atmosphere models. The single-layer case offers a simplified view — assuming only the r_0 and wind speed at an atmospheric layer — useful for isolating algorithm behavior and initial tests. Conversely, the multi-layer model better reflects atmospheric conditions closer to the real-life scenario by accounting for different altitudes, wind speeds, and turbulence strengths through the atmosphere. For this study, the goal is to evaluate the predictive models' capability to mitigate the effects of turbulence. A single-layer atmospheric model will serve as the baseline for assessing their performance, although future work should extend the analysis to more realistic multi-layer atmospheric conditions.

The wind speed to consider in each of the layers should be the total wind — natural and apparent —, which accounts for both the real wind crossing the section and the relative movement of the satellite to the telescope lens.

To evaluate the performance of the proposed control strategies under diverse atmospheric conditions, diverse values of r_0 are considered in the simulations. This parameter represents the integrated turbulence strength and is strongly influenced by local factors such as altitude, elevation, the meteorological conditions, and the observability of the sky. For instance, a telescope placed in the middle of a city will have a smaller r_0 — in the order of some centimeters — while in high-altitude observatories it will be around 10 times larger.

5.2 Single-Layer Case Study

This section will present the simulation parameters and the performance of the temporal prediction models for AO in each case.

Usually, AO systems for FSOC tend to vary between the following parameters:

Table 5.3: Boundary parameters from FSOC AO systems.

Name	Maximum	Minimum	Units
Telescope diameter	1	0.4	m
Loop sampling frequency, f_s	5000	1000	Hz
SH subpupils	20×20	6×6	-

The parameters presented in Table 5.3 represent the characteristics of the equipment used in the AO system. To evaluate the impact of different equipment, and the trade-off between higher performance and resolution, the cases studied are defined in Table 5.4 — Case 4 corresponds to *LISA* and Case 5 to *FEELINGS* from *ONERA*.

Table 5.4: Simulation parameters from FSOC AO systems.

Name	Case 1	Case 2	Case 3	Case 4	Case 5	Units
Telescope diameter	1	0.5	0.4	0.4	0.6	m
Loop sampling frequency, f_s	5000	3000	1000	2000	4500	Hz
SH subpupils	20×20	12×12	6×6	8×8	16×16	-

While these parameters describe the equipment, it is also necessary to define the limits of the atmospheric parameters — the wind speed and turbulence parameter r_0.

Table 5.5: Boundary atmospheric parameters.

Name	Maximum	Minimum	Units
Fried's parameter, r_0	0.2	0.01	m
Wind speed, v_{wind}	200	70	m/s

In urban or polluted environments where atmospheric turbulence is significant, the Fried parameter r_0 typically falls within the range of 4–6 cm at 1500 nm. In contrast, under excellent seeing conditions — such as those observed at high-altitude observatories like Cerro Paranal — r_0 can reach values of approximately 20 cm. These bounds will define the operational range considered for r_0 in this study.

The total wind speed, which characterizes the effective motion of turbulent layers across the telescope aperture, also varies significantly with observing conditions. Studying a satellite with an average 7.5 km/s at an altitude of 400 km, the apparent wind speed observed from a layer at 10 km altitude depends on the satellite's elevation angle, reaching a maximum of 187.5 m/s at the zenith. To account for variations with elevation and to include a margin for the natural wind component, the wind speed is assumed to range between 70 m/s and 200 m/s. Thus, considering elevations between 20° and 90° (see Section 2.5.3).

When simulating average atmospheric conditions, they will be considered as $r_0 = 0.1$ m and $v_{wind} = 100$ m/s, which correspond to Cases 2, 4, and 5.

5.2.1 Case 1: Optimal Scenario

Under the configuration of Case 1 (Table 5.4) and the optimal atmospheric conditions (Table 5.5), the performance of the predictive models can be evaluated in Figure 5.1 and Figure 5.2.

For a loop sampling frequency of 5000 Hz, the temporal lag τ will always be greater than 0.0002 s ($\tau \geq 1/f_s$). For that temporal lag, the VAR models clearly have a better performance, both in terms of less residual phase variance and SR — the optical system is performing very close to the diffraction limit, meaning that the correction is almost perfect.

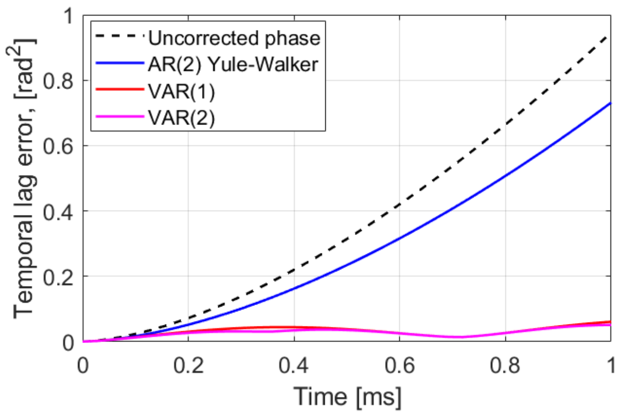

Figure 5.1: Plot display of the temporal lag error of Case 1 under optimal atmospheric conditions.

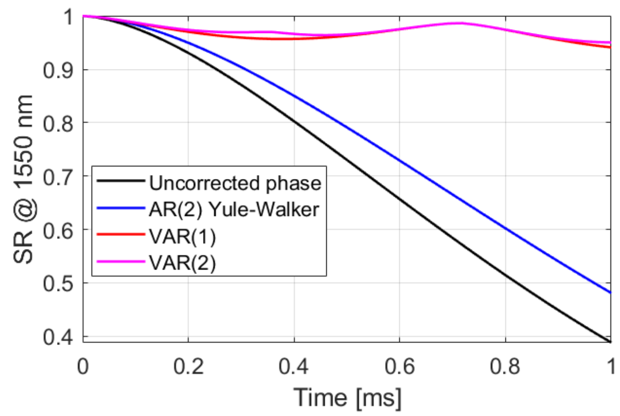

Figure 5.2: Plot displaying the SR of Case 1 under optimal atmospheric conditions.

The SR analysis demonstrates that the optical quality achieved using VAR-based predictive models is significantly higher compared to other approaches. Among the VAR models, performance is comparable in terms of average SR; however, a characteristic feature of VAR-based predictions is the presence of temporal fluctuations. These fluctuations are more pronounced in the VAR(2) model and tend to occur at approximately twice the frequency observed in the VAR(1) model (discussed in Section 4.3.2.2).

5.2.2 Case 2: Intermediate Scenario

For Case 2 (Table 5.4) and average atmospheric conditions — $r_0 = 0.1$ m and $v_{wind} = 100$ m/s — the performance of the predictive models can be evaluated in Figure 5.3 and Figure 5.4.

For a loop sampling frequency of 3000 Hz, the temporal lag τ will always be greater than 0.0003 s ($\tau \geq 1/f_s$).

Under this set of conditions, system performance deteriorated compared to Case 1, as evidenced by an overall increase in phase residual variance across all models. Despite this degradation, the VAR-based models continued to outperform the alternatives, maintaining the best correction quality.

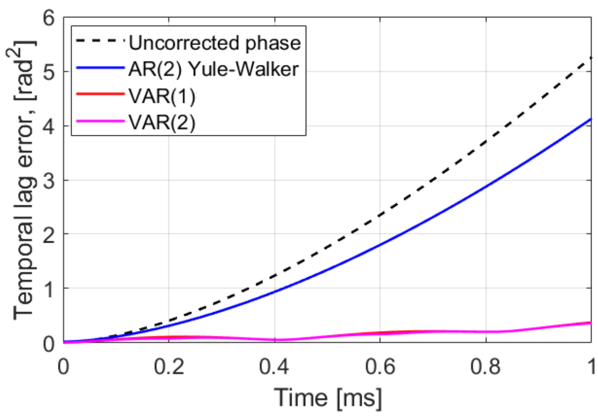

Figure 5.3: Plot display of the temporal lag error of Case 2 under average atmospheric conditions.

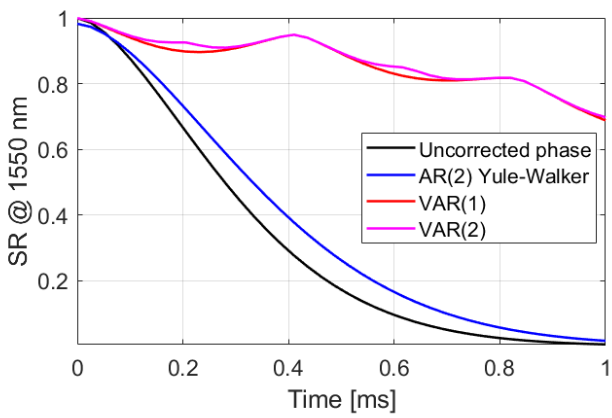

Figure 5.4: Plot displaying the SR of Case 2 under average atmospheric conditions.

Visually, the SR curve of Figure 5.4 resembles that of Case 1 in Figure 5.2, but appears squished along the time axis, indicating a similar behavior occurring at a reduced temporal frequency. Therefore, the performance will be equally good for smaller delay intervals.

5.2.3 Case 3: Worst Scenario

In Case 3 (Table 5.4) and for poor atmospheric conditions (Table 5.5), the performance of the predictive models can be evaluated in Figure 5.5 and Figure 5.6.

For a loop sampling frequency of 1000 Hz, the temporal lag τ will always be greater than 0.001 s $(\tau \geq 1/f_s)$. For much lower temporal lags, the system already fails to correct the wavefront. The combination of suboptimal AO parameters and the most severe atmospheric turbulence simulated underscores the need for high-performance AO systems if FSOC is to be reliably deployed in urban environments, or to communicate at low elevations with satellites. As expected, system performance is significantly degraded under these adverse conditions.

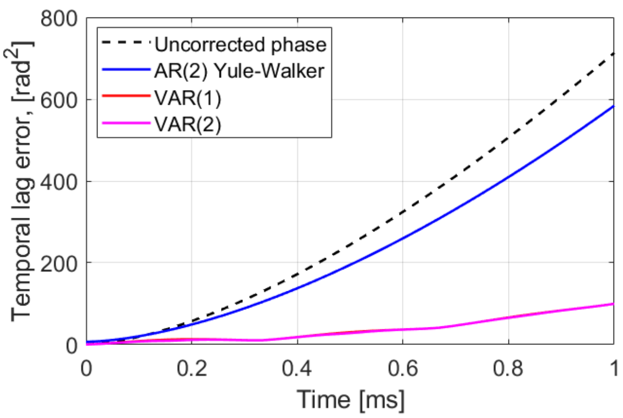

Figure 5.5: Plot display of the temporal lag error of Case 3 under poor atmospheric conditions.

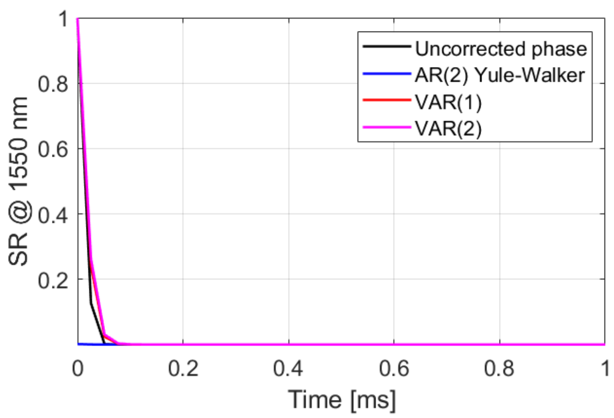

Figure 5.6: Plot displaying the SR of Case 3 under poor atmospheric conditions.

Figure 5.6 highlights the importance of a high-performance AO system when operating under poor atmospheric conditions. To identify which simulation parameters most significantly enable effective wavefront correction in such scenarios, it becomes necessary to analyse the individual impact of each parameter on the performance of the predictive models, done in Section 5.4.

5.2.4 Case 4: *LISA*

For the *LISA* AO configuration (Table 5.4), with average atmospheric conditions — $r_0 = 0.1$ m and $v_{wind} = 100$ m/s — the performance of the predictive models is shown in Figure 5.7 and Figure 5.8.

The *LISA* configuration was designed to represent an AO system with realistic but moderately high-performance parameters. For a loop sampling frequency of 2000 Hz, the temporal lag τ will always be greater than 0.0005 s $(\tau \geq 1/f_s)$. As shown in Figure 5.7, the temporal lag error indicates a clear reduction in phase residuals when using VAR-based predictors.

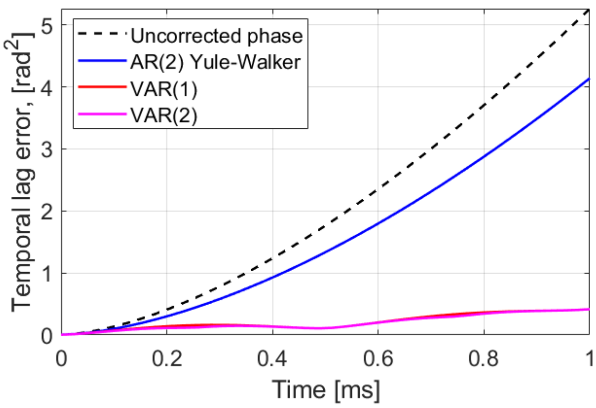

Figure 5.7: Plot display of the temporal lag error of Case 4 under average atmospheric conditions.

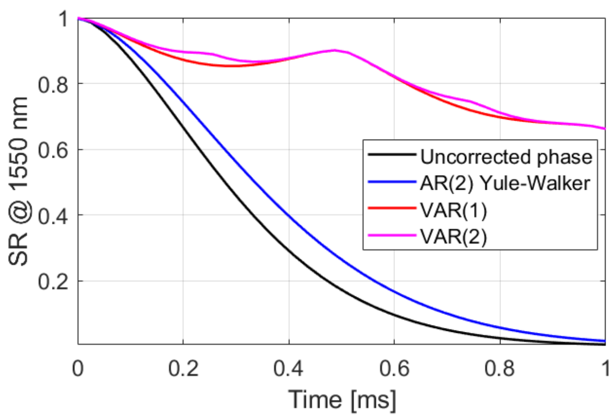

Figure 5.8: Plot displaying the SR of Case 4 under average atmospheric conditions.

In this setting, the fluctuations characteristic of the VAR models are more pronounced than in Cases 1 and 2, observable on Figure 5.8. These fluctuations are likely caused by the lower spatial resolution of the SH wavefront sensor, which limits the precision of the measured wavefront data and, consequently, affects the stability of the predictor.

5.2.5 Case 5: *FEELINGS*

For the *FEELINGS* AO configuration (Table 5.4), with average atmospheric conditions — $r_0 = 0.1$ m and $v_{wind} = 100$ m/s — the performance of the predictive models is shown in Figure 5.9 and Figure 5.10.

For a loop sampling frequency of 4500 Hz, the temporal lag τ will always be greater than 0.0002 s ($\tau \geq 1/f_s$).

Compared to the *LISA* setup in Case 4, the *FEELINGS* configuration features slightly improved AO parameters, such as a higher actuator density and a more responsive — higher sampling frequency — control loop. This results in noticeably improved predictive performance — particularly for the VAR models. As observed in Figure 5.9, the residual phase variance is lower across all VAR-based predictors, indicating that the system is better able to compensate for atmospheric distortions within the same lag interval.

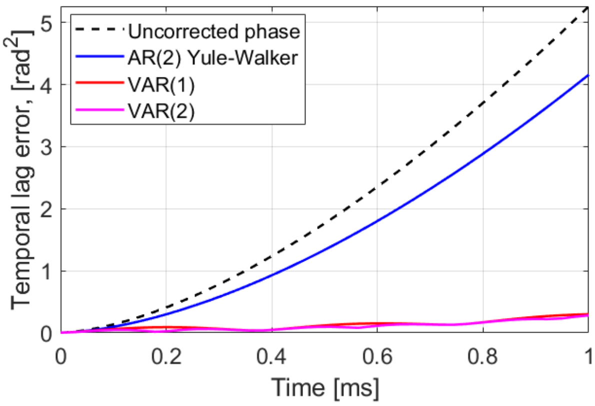

Figure 5.9: Plot display of the temporal lag error of Case 5 under average atmospheric conditions.

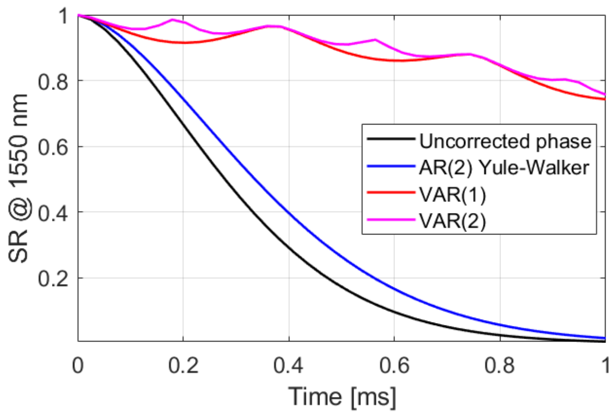

Figure 5.10: Plot displaying the SR of Case 5 under average atmospheric conditions.

In terms of optical quality, Figure 5.10 reveals a higher and more stable SR compared to Case 4. This improvement is most evident in the VAR(2) model, which exhibits reduced temporal fluctuations and maintains a consistently higher SR level. These findings suggest that VAR models are sensitive to fine-tuning of AO system parameters and can significantly benefit from enhanced hardware configurations.

This case reinforces the importance of optimizing AO design in tandem with selecting suitable predictive models. Even modest improvements in AO specifications can yield measurable gains in predictive control accuracy and overall system performance, making FSOC systems more viable under real-world atmospheric conditions.

5.2.6 Summary

These results explore a progression from the best-case scenario — combining an optimal AO system with ideal atmospheric conditions — to an average configuration with moderate parameters, and finally to the worst-case scenario where both the AO system and atmospheric conditions are severely degraded. It becomes evident that enabling reliable FSOC in urban environments requires high-performance predictive AO systems. Without such systems, maintaining a stable optical link between the ground station and the LEO satellite is not feasible. Case 3, in particular, illustrates the stringent demands placed on the AO system when operating under poor seeing conditions, which are more prevalent in densely populated and polluted urban areas.

Cases 4 and 5 — two realistic cases — yield results similar to those of Case 2, both in terms of residual phase variance and SR, except for the VAR models, which obtain significantly better results on Case 5. This leads to the conclusion that VAR models are able to achieve better correction with a slight improvement in simulation parameters. Although the AO system parameters differ slightly between these cases, their overall similarity suggests that the dominant factor influencing performance is the atmospheric condition. To quantify a prediction gain, an analysis is done in

Section 5.3, and to better understand the specific causes of performance degradation, a parameter-wise analysis is necessary — examining the individual impact of both atmospheric and AO system parameters, for a fixed temporal lag, across each predictive model.

5.3 Prediction Gain Analysis

To quantify the possible reduction of the temporal error in AO systems, this section presents an analysis of the prediction gain, taking the *LISA* and *FEELINGS* configurations as case studies. The evaluation based on the residual phase variance, under the same turbulence profile defined in the previous section — $r_0 = 0.1$ m and $v_{wind} = 100$ m/s.

Four predictors are considered: the uncorrected phase, which establishes the baseline reference; an AR(2) model derived through the Yule–Walker equations; and VAR(1) and VAR(2) models estimated via the MMSE method.

Performance is quantified through the relative gain with respect to the no-prediction case, defined as the ratio of the residual phase variance with prediction to that of the uncorrected phase:

$$\text{Gain}(\%) = \left(1 - \frac{\sigma^2_{\text{prediction}}}{\sigma^2_{\text{no-prediction}}}\right) \times 100 \tag{5.1}$$

In this formulation, higher percentages correspond to stronger predictive power — a prediction gain of 100% corresponds to 0 rad^2 residual phase variance, meaning perfect correction. Expressing results in this way highlights not only whether a predictor is effective, but also how much closer it brings the system toward overcoming the temporal error barrier that fundamentally limits AO performance.

Table 5.6 presents selected values of the prediction gain at specific time lags, while Figure 5.11 illustrates the overall results for the *LISA* and *FEELINGS* configurations, shown individually in Figure 5.11a and Figure 5.11b, respectively.

Table 5.6: Prediction gains for the *LISA* and *FEELINGS* configurations as a function of temporal lag, τ, showing the residual phase variance (rad^2) obtained with the four predictors. Results correspond to a turbulence profile with $r_0 = 0.1$ m and $v_{wind} = 100$ m/s.

	Lag (s)	Uncorrected	AR(2) YW	Gain (%)	VAR(1)	Gain (%)	VAR(2)	Gain (%)
LISA	0.0005	3.1264	2.4082	22.97	0.3123	90.01	0.2463	92.12
	0.0007	5.0105	3.9279	21.60	0.3983	92.05	0.3969	92.08
	0.0010	8.8819	7.1443	19.56	0.9102	89.75	0.9052	89.90
FEELINGS	0.0002	0.7267	0.5363	26.20	0.0679	90.66	0.0580	92.02
	0.0005	3.1264	2.4146	22.77	0.1301	95.84	0.1286	95.89
	0.0007	5.0105	3.9460	21.25	0.2891	94.23	0.2520	94.97
	0.0010	8.8819	7.1919	19.03	0.5587	93.71	0.5506	93.80

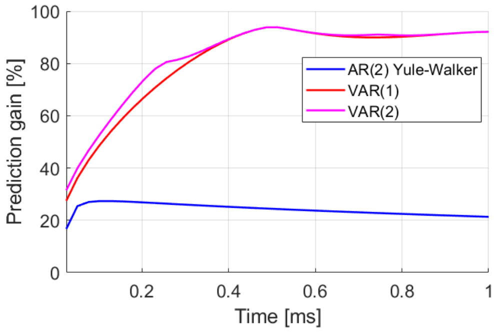

(a) *LISA*.

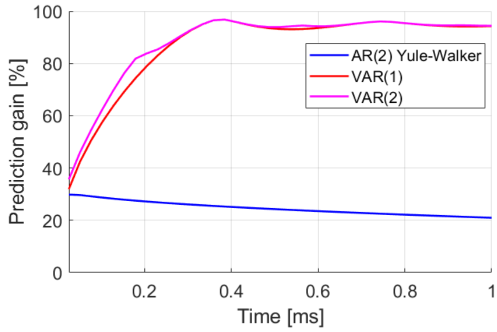

(b) *FEELINGS*.

Figure 5.11: Plot showing the prediction gain for (a) the *LISA* and (b) the *FEELINGS* configuration as a function of temporal lag, τ, in comparison to the uncorrected phase model. Results correspond to a turbulence profile with $r_0 = 0.1$ m and $v_{wind} = 100$ m/s.

The temporal lags were selected to overlap each system's sampling period — ranging from a one-frame effective delay to multi-frame delays — and approximating the sampling period of the *FEELINGS* to have more homogeneous results, enabling a fair comparison under identical turbulence.

Both configurations yield very similar results for the AR(2) model estimated using the Yule-Walker method. An interesting point since they vary in aperture, sampling frequency, and the number of subapertures of the SH. While the uncorrected phase and AR(2) Yule-Walker models show similar performance across both systems, VAR models reveal a pronounced advantage for *FEELINGS* due to its higher sampling frequency.

For each VAR model, the prediction gain for both configurations is nearly identical when compared to the no-prediction case, indicating a similar relationship between these predictive models and the baseline. However, since the *LISA* configuration exhibits slightly higher residual phase variance than *FEELINGS* at larger temporal lags, its prediction gain becomes correspondingly lower in that regime.

Although the VAR(2) model achieves slightly better results in both configurations, its improvement over VAR(1) remains marginal, with the largest observed difference being only 2%. Since these results are based solely on phase aberrations while neglecting amplitude effects for a simplified model of the atmosphere, they do not yet reflect the full system behavior. A more complete evaluation with the full model is therefore required. Nevertheless, within this simplified framework, the results suggest that increasing the model order beyond one offers little practical benefit.

5.4 Simulation Parameters Sensitivity Analysis

In Section 5.2, five simulation configurations were analyzed, obtaining significantly distinct results. The prediction gain analysis of Section 5.3 also made clear the effects of having higher performance equipment. These differences stem from the specific parameter settings applied in each case. This motivates a deeper investigation into how varying individual parameters — while holding others constant — affect system performance.

This section aims to identify the primary contributors to performance variation by examining the impact of each parameter, within typical operational bounds of an FSOC AO system, on residual phase variance and SR. This analysis supports the development of trade-offs between system optimization and optical performance quality.

To evaluate the effect of each individual parameter, all other system parameters were held constant — including the system lag τ. The baseline configuration selected for this analysis was *FEELINGS*, as both *FEELINGS* and *LISA* are based on prior research, making them more reliable than the hypothetical test cases. Between *LISA* and *FEELINGS*, the AR model showed similar performance, whereas the VAR models performed better under the *FEELINGS* setup.

Regarding the choice of system lag τ, since the AO loop operates at 4500 Hz (an update every $1/4500$ s ≈ 0.00022 s), a slightly larger value of 0.0005 s was selected, $\tau \geq 2T_s = 0.0004$ s. This reflects the realistic presence of hardware and processing delays, while remaining within a plausible range for predictive control.

Table 5.7 presents the baseline simulation parameters used for the sensitivity analysis. These are based on the *FEELINGS* configuration, chosen for its realistic and research-backed characteristics.

Table 5.7: Baseline simulation parameters used in the sensitivity analysis, derived from the *FEELINGS* configuration.

Name	Case 5	Units
Telescope diameter	0.6	m
Loop sampling frequency, f_s	4500	Hz
Temporal lag, τ	0.0005	s
SH subpupils	16×16	-
Fried's parameter, r_0	0.10	m
Wind speed, v_{wind}	100	m/s

Although the atmospheric parameters are well-established in the literature and have been used extensively in AO modeling, a degree of uncertainty is always associated with them. In particular, the wind velocity profile and Fried's parameter, r_0, can never be known with absolute precision during real operation. To account for this, a robustness analysis will be carried out to evaluate how sensitive each predictive model is to such parameter mismatches.

The methodology involves first simulating a baseline case in which the predictor is provided with the exact atmospheric parameters. This is then followed by perturbed scenarios, where the predictor assumes slightly different values of wind speed, wind direction, or r_0 , while the atmospheric simulation retains the true values. By analyzing performance metrics such as the residual phase variance across these cases, it becomes possible to determine the extent of parameter uncertainty that can be tolerated while still achieving a lower lag error than in the no-prediction case. The formulation to do this analysis is presented in Appendix B.

5.4.1 Shack-Hartmann Number of Lenslets

The influence of the number of lenslets of the SH wavefront sensor, ranging in the typical parameters of Table 5.3, also affects the number of actuators in the DM, since they are directly coupled. Fixing the other simulation parameters to those of Table 5.7, the results of this analysis are shown in Figure 5.12 and Figure 5.13.

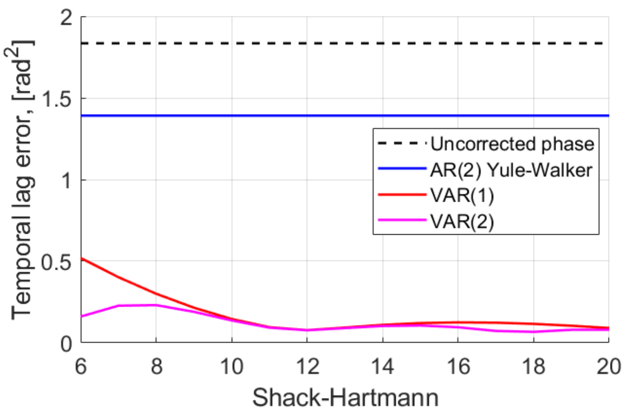

Figure 5.12: Plot displaying the residual phase variance as a function of SH number of lenslets, while all other parameters are fixed to the baseline configuration in Table 5.7.

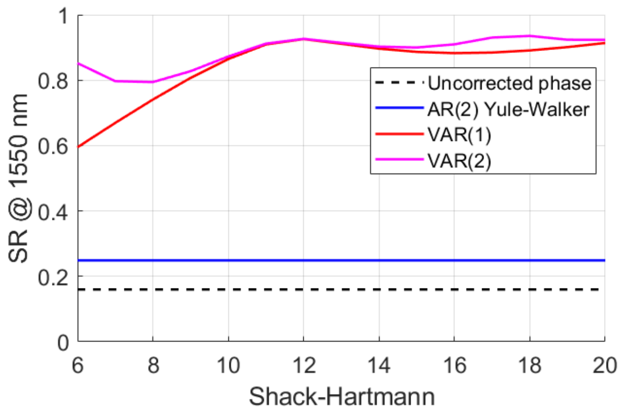

Figure 5.13: Plot displaying the SR as a function of SH number of lenslets, while all other parameters are fixed to the baseline configuration in Table 5.7.

Increasing the number of subapertures in the SH wavefront sensor does not affect the structure or performance of the AR-based predictive models. Consequently, even with a high-resolution WFS, these models fail to ensure a stable optical link. This limitation is evident from the fact that the SR remains below 0.3 in all tested cases, which is insufficient for maintaining reliable FSOC performance.

These observations further underscore the necessity of adopting VAR models. In particular, the VAR(2) model exhibits greater robustness to fluctuations in the number of subapertures of the SH, demonstrated by its lower amplitude variation in both residual phase variance and SR. This enhanced stability confirms its effectiveness in enabling high-performance FSOC links under realistic conditions.

5.4.2 Wind Speed, v_{wind}

The total wind speed has a direct impact on the temporal dynamics of the wavefront distortions, influencing how well the predictive models can compensate for phase variations. While all other parameters are fixed according to the baseline in Table 5.7, the system's response was evaluated over the wind speed interval defined in Table 5.3. The corresponding results are shown in Figure 5.14 and Figure 5.15.

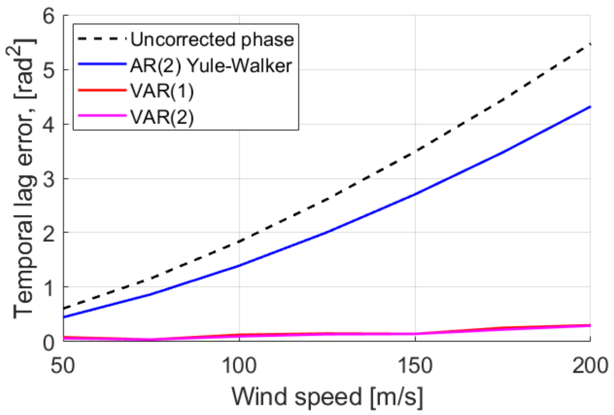

Figure 5.14: Plot displaying the residual phase variance as a function of wind speed v_{wind}, while all other parameters are fixed to the baseline configuration in Table 5.7.

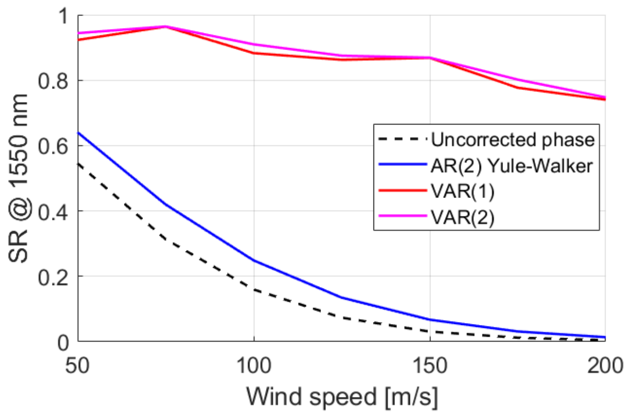

Figure 5.15: Plot displaying the SR as a function of wind speed v_{wind}, while all other parameters are fixed to the baseline configuration in Table 5.7.

The AR-based models once again underperform, failing to maintain a stable optical link under varying wind speeds. In contrast, VAR-based models demonstrate high robustness and reliability.

During satellite tracking — from an elevation angle of 30° up to zenith, and back down to 30° — the total wind velocity varies significantly, as described in Section 2.5.3. Since wind speed is modeled as a function of elevation, this variation spans a range of approximately 150 m/s throughout the tracking interval. Despite this large fluctuation, the VAR models demonstrate strong robustness, with the SR varying by no more than 0.1. This confirms the effectiveness of spatio-temporal prediction in dynamic conditions, making VAR models suitable for practical FSOC scenarios involving satellite motion.

As it was mentioned before, the estimated wind speed is not 100% accurate, thus some errors in prediction can arise from estimating a slightly wrong value. To quantify this, a robustness test of the wind speed value and direction was done, Figure 5.16 and Figure 5.17 respectively. Where a mismatch factor quantifies the relative discrepancy between the true atmospheric parameter used to generate the turbulence covariances and the assumed value used in the predictor design.

In the case of wind speed, the mismatch factor k_v was established such that the effective assumed velocity is $v_{\text{assumed}} = k_v \cdot v_{\text{true}}$. Values of $k_v > 1$ represent overestimation of the speed, values $0 < k_v < 1$ represent underestimation, and negative values correspond to inversion of the wind direction. Since the models used to estimate the wind speed (Section 2.5.3) are well established, the expected deviations from the true value are relatively small. Anyway, the robustness analysis was carried out for $k_v \in [-0.5, 2.5]$, a large interval precisely to highlight how robust the predictive models are to a mismatch in wind speed.

For wind direction, the mismatch factor is given by an angular offset θ_ε applied to the nominal direction θ_0, such that $\theta = \theta_0 + \theta_\varepsilon$, with positive and negative values corresponding to clockwise or counter-clockwise deviations. In Section 4.3.1, it is illustrated how the predictive VAR models are explicitly designed around the wind direction; therefore, even small errors in their estimation are expected to impact performance, with the severity of the effect depending on the magnitude of the deviation.

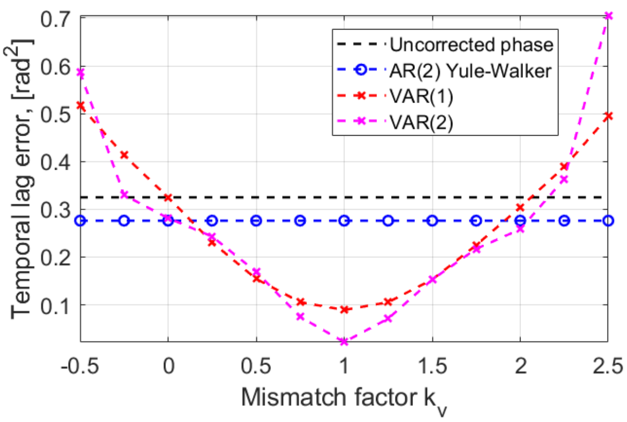

Figure 5.16: Plot representing the robustness of the predictive models to wind speed mismatch factor k_v, with a *FEELINGS* system.

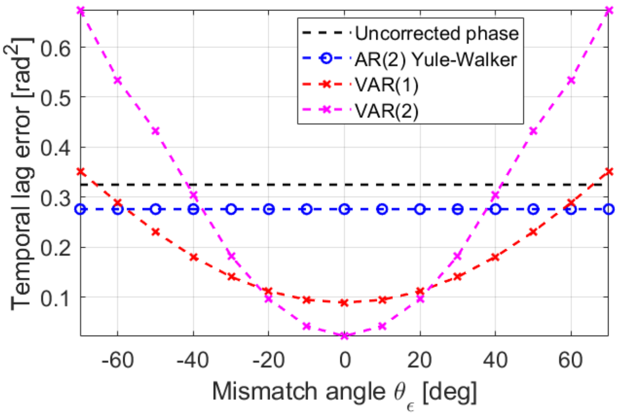

Figure 5.17: Plot representing the robustness of the predictive models to wind direction mismatch angle θ_ε, with a *FEELINGS* system.

The AR models did not exhibit any sensitivity to mismatches in either wind speed or wind direction. This behavior is expected, as they rely solely on the temporal evolution at each point independently and are therefore unaffected by errors in the assumed wind shift. As a result, these models are inherently more robust: even if the wind parameters are poorly estimated, the temporal lag error does not increase. In contrast, the VAR models, which explicitly embed spatial correlations through the wind-driven shift, showed sensitivity to deviations from the true wind parameters.

Results for the VAR(1) model indicate that the wind speed of a given layer can be overestimated up to a factor of 2 before lag error reaches the equivalent of no-prediction. An error in wind direction of up to 60° still reduces temporal lag error, at a sample frequency of 4500 Hz. The VAR(2) model exhibits similar robustness to wind-speed errors; however, its tolerance to wind-direction mismatch is lower, with deviations of about 40° already leading to performance equivalent to the no-prediction case. This behavior highlights a trade-off between prediction accuracy and robustness. While VAR(2) can provide higher accuracy than VAR(1) when the wind parameters are perfectly known, its longer temporal horizon makes it more sensitive to errors in wind direction. Consequently, even moderate deviations can degrade its performance, potentially making it less reliable than VAR(1) or point-wise AR models under uncertain conditions.

5.4.3 Sampling Frequency, f_s

The sampling frequency f_s is directly related to the temporal lag τ of the AO system. Most AO systems exhibit a lag of approximately two sampling intervals between the wavefront measurement and the corresponding actuation, due to sensor integration, processing, and actuator response delays. As such, the system delay can be approximated by:

$$\tau \approx 2 \times \frac{1}{f_s} \tag{5.2}$$

This implies that increasing the sampling frequency — a function of hardware capabilities — can reduce the effective delay in the correction loop.

For the following analysis, all parameters are fixed according to the baseline configuration in Table 5.7, except for the sampling frequency, which is varied within the limits defined in Table 5.3. The corresponding temporal lag τ is computed using Equation (5.2).

Figures 5.19 and 5.18 illustrate the impact of varying the sampling frequency on the system's optical performance.

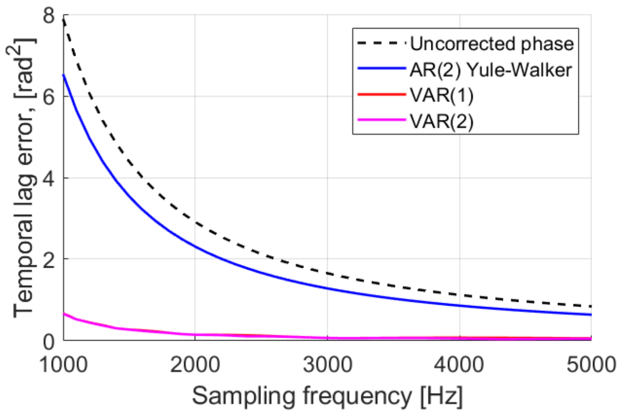

Figure 5.18: Plot displaying the residual phase variance as a function of sampling frequency f_s, the lag τ is adjusted to each f_s, while all other parameters are fixed to the baseline configuration in Table 5.7 — VAR(1) and VAR(2) overlap.

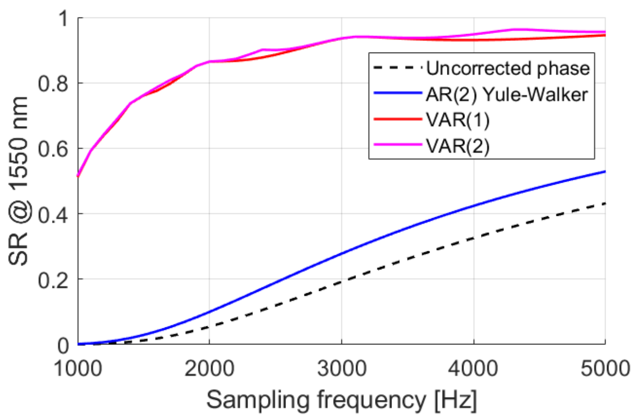

Figure 5.19: Plot displaying the SR as a function of sampling frequency f_s, the lag τ is adjusted to each f_s, while all other parameters are fixed to the baseline configuration in Table 5.7.

As shown in Figure 5.19, increasing the sampling frequency significantly improves the SR for all predictive models. The VAR-based predictors, particularly VAR(2), consistently outperform all others, achieving a SR above 0.9 at a sampling frequency higher than 4000 Hz. This demonstrates the VAR model's ability to effectively compensate for faster phase dynamics at higher loop rates.

In contrast, AR-based models exhibit more limited performance. Even at high sampling frequencies, their maximum SR remains of 0.5.

Similarly, as shown in Figure 5.18, the residual phase variance of VAR(1) and VAR(2) decreases sharply with increasing sampling frequency, while AR models achieve only gradual improvements. Across the entire frequency range, AR-based models show an order of magnitude higher residual error compared to their vector counterparts.

5.4.4 Fried's Parameter, r_0

From the failure of Case 2 (Section 5.2.2), it became evident that Fried's parameter r_0 plays a critical role in maintaining a reliable link. This observation led to the hypothesis that r_0 is among the most influential parameters affecting system performance.

To test this hypothesis, an analysis was performed by varying r_0 within the boundary values defined in Table 5.5, while keeping all other parameters fixed according to the baseline configuration specified in Table 5.7.

Fried's parameter, or coherence length, represents the aperture diameter for which the wavefront phase variance reaches 1 rad^2 at a given wavelength. By isolating this parameter, its specific impact on residual phase variance and SR can be evaluated.

The results of this sensitivity analysis are shown in Figures 5.20 and 5.21.

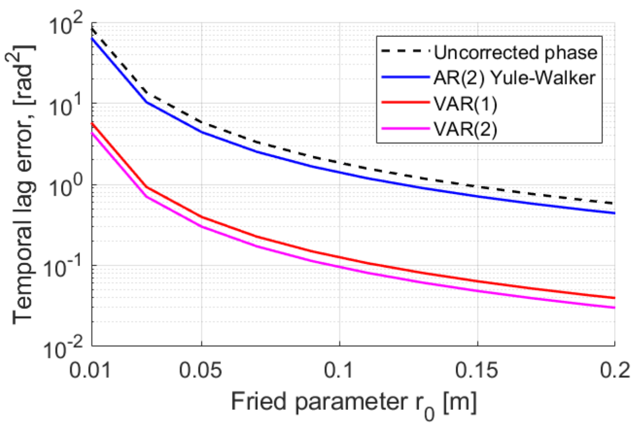

Figure 5.20: Plot displaying the residual phase variance as a function of Fried's parameter r_0, while all other parameters are fixed to the baseline configuration in Table 5.7.

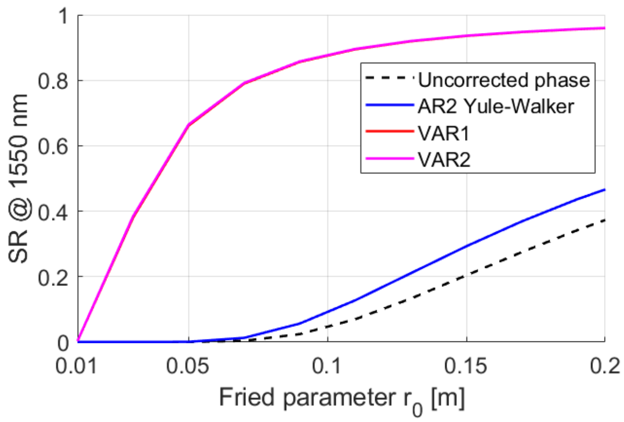

Figure 5.21: Plot displaying the SR as a function of Fried's parameter r_0, while all other parameters are fixed to the baseline configuration in Table 5.7.

For the simulated range defined in Table 5.5, Fried's parameter r_0 exhibits the most significant influence on system performance. Specifically, variations in r_0 result in changes to the residual phase variance spanning over two orders of magnitude, which in turn has a profound impact on the SR, as shown in Figures 5.20 and 5.21.

These results highlight the critical importance of operating in environments with favorable turbulence conditions. In particular, to enable reliable FSOC operation in urban, high-turbulence, or low elevation scenarios, it becomes essential to employ high-performance AO systems in conjunction with advanced predictive control strategies, such as VAR models. Without these, the wavefront distortions become too severe, and the signal may be entirely lost.

A similar robustness analysis to the one done in Section 5.4.2 was conducted for variations in the atmospheric coherence length r_0, which quantifies the strength of turbulence. In this case, the mismatch factor was defined as a relative scaling of the true value is $r_{\text{assumed}} = k_{r_0} \cdot r_0$, where $k_{r_0} > 1$ corresponds to an overestimation of the turbulence strength — a larger r_0 than the actual value, corresponding to weaker turbulence — and $k_{r_0} < 1$ corresponds to underestimation — a smaller r_0, corresponding to stronger turbulence. The analysis was carried out for $k_{r_0} \in [0.5, 1.5]$, covering plausible deviations from the nominal atmospheric conditions.

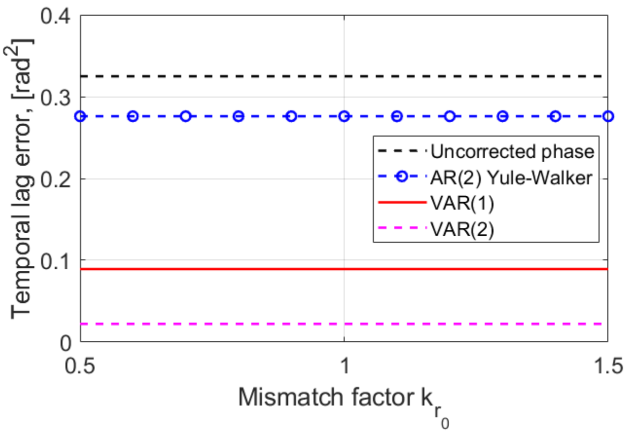

Figure 5.22: Robustness of the predictive models to Friend's parameter, r_0, mismatch factor k, with a *FEELINGS* system, the baseline $r_0 = 0.1$ m.

Regarding variations in r_0, all predictive models, including both AR and VAR, showed no appreciable change in temporal lag error — the resulting curves remain essentially flat. This behavior is expected because the design of the predictors cancels out the dependence on the turbulence strength, rendering the temporal lag error largely independent of r_0. Consequently, even under poorly estimated or extreme turbulence conditions, the performance of both point-wise AR models and VAR models remains effectively unchanged, highlighting the inherent robustness of the predictive framework with respect to variations in r_0.

5.4.5 Summary

This study aimed to identify the primary contributors to performance variations by examining the impact of the variation of each parameter within the boundaries of FSOC systems, as those of Table 5.3 and Table 5.5 in the performance metrics chosen.

The AR-models showed no sensitivity to the variation in the number of subapertures on the SH wavefront sensor. These models assume that the temporal evolution of a spatial point in the phase screen is dependent only on its own past values. Increasing the number of subapertures in the SH WFS results in an increase of the spatial resolution. AR models cannot exploit the added spatial information or increased turbulence complexity introduced by higher-resolution sensing. They are dependent only on the atmospheric conditions and sampling frequency.

This analysis also determined that the AR models are only capable of achieving enough wavefront correction to ensure the link for very low turbulent environments, with a high-performance AO system.

While the VAR models demonstrated stable correction capability across different numbers of subapertures and wind speeds, their performance was not entirely invariant. This indicates that these system parameters do influence the quality of the model estimation, leading to slight fluctuations in residual phase variance and SR.

The VAR(2) model exhibits significantly lower variability in performance across parameter changes. This is attributed to its ability to capture more spatio-temporal information through the inclusion of two past states, making it inherently more robust. In contrast, VAR(1) is more sensitive to disturbances or variations in the system configuration.

Additionally, a jitter-like fluctuation was observed in the performance metrics of both models, with VAR(2) showing oscillations at approximately twice the frequency of VAR(1). This behavior likely stems from the model order, and it is presented in Section 4.3.1.

Finally, among all parameters tested within the boundary ranges defined in Table 5.3 and Table 5.5, only the sampling frequency — limited by the hardware — and Fried's parameter r_0 showed significant variations in the effectiveness of the wavefront corrected with VAR models, even compromising the establishment of the link. This justifies the need to utilize high-frequency equipment.

Regarding r_0, it is determined for a specific geographical location and time, and it also varies with elevation, with higher values for lower elevations. The results show that it has a severe impact on the ability of the AO system to correct the wavefront. However, the predictive models under analysis showed complete robustness to this parameter, implying that regardless of its value, they consistently outperformed the no-prediction baseline.

The robustness analyses presented in this chapter highlight the performance of predictive models under variations in wind speed, wind direction, and turbulence strength r_0. Point-wise AR models proved inherently robust, showing no sensitivity to any of these mismatches, as they rely solely on the temporal evolution at each spatial point independently. In contrast, VAR models, which explicitly encode spatial correlations through wind-driven shifts, exhibited a trade-off between accuracy and robustness: while higher-order models such as VAR(2) can achieve lower temporal lag error when the atmospheric parameters are perfectly known, they become more sensitive to wind-direction mismatches, with moderate deviations potentially degrading performance to the level of no-prediction. Across all models, variations in r_0 had negligible effect on temporal lag error, indicating that the predictor design effectively cancels out the influence of turbulence strength. Overall, these results emphasize that model order and the type of correlations exploited dictate the balance between achievable accuracy and robustness to parameter uncertainties.

Chapter 6

Conclusion

The work presented in this thesis focused on the capability of improving wavefront correction and mitigating the effects of atmospheric turbulence in the case of LEO satellite-to-ground FSOC, within the LQG framework.

In this work, all models were estimated through the Yule-Walker equations, merging the fact that it has the same results as those of the MMSE model estimation. When deriving the equations, they have the same formulation, so in this study, a single model for estimation was used. This approach not only simplifies the estimation process but also ensures consistency and reliability across all predictive models.

Regarding model order, the results showed that increasing it does not significantly improve wavefront correction. As discussed in Section 4.3.1, raising the order causes the oscillation of variance to occur more frequently. For instance, in the VAR(2) model, this oscillation appears twice as often as in VAR(1), and, in general, for a model of order p, it occurs p times more frequently. These oscillations take place within different ranges of residual phase variance (or SR) values, and in higher-order VAR models, their amplitude is partially mitigated. This is the main benefit of increasing model order: achieving a more robust identification. Robustness tests with respect to atmospheric parameters showed that VAR models can account for large variations while still achieving lower temporal lag errors. In particular, the VAR(2) model was more sensitive to a mismatch in wind direction; however, the mismatch had to be very large for its error to exceed that of the AR(2) Yule-Walker or uncorrected phase models. Regarding wind speed, both models required a very large mismatch factor to produce a significant increase in error. Nevertheless, to balance robustness with sensitivity and to limit computational cost, the order was fixed at $p = 2$.

The single-layer case studies demonstrated that, to maintain a stable optical link between a LEO satellite and a ground station, high-performance AO is essential. Case 3 highlighted that, in FSOC, the AO loop frequency must be higher, even when predictive control is applied. The parameter sensitivity analysis supported this conclusion by showing that increasing the AO loop frequency — the hardware parameter with the strongest impact — significantly enhances wavefront correction. This, in turn, leads to substantial improvements in the received optical signal, since the SR and fiber coupling efficiency are closely related.

The other hardware parameters did not show significant variation of the residual phase variance; thus, in the design of an AO system for FSOC, any values ranging between those of Table 5.3 would be a feasible option.

Within the range of atmospheric variations considered, the VAR models proved capable of withstanding these changes while maintaining performance.

It is important to note that this study employs a simplified atmospheric model, accounting only for phase disturbances and neglecting other effects such as amplitude fluctuations or multi-layer turbulence. Despite these simplifications, the results provide valuable insights into the relative impact of model order, AO hardware parameters, and atmospheric variations on FSOC performance. From these findings, it can be concluded that, in more accurate or site-specific atmospheric models, similar trends are expected to hold, but additional considerations may be required to fully optimize wavefront correction and maintain stable optical links.

6.1 Limitations and Future Work

This section presents recommendations based on the results of this thesis and their limitations:

1. This study served as a baseline, thus a single-layer model was used; however to better represent the effects of atmospheric turbulence, a multi-layer model should be studied since it reflects a closer to real-life scenario.

2. In the sensitivity analysis, when studying the wind speed, the r_0 was kept constant, and vice versa. This does not represent how they vary simultaneously, since they both depend on the satellite's elevation. Thus, the residual phase variance should be studied as a function of elevation instead.

3. This study limited the testing to the wavefront's phase distortions. Amplitude variations, induced by strong turbulence, should also be accounted in the controllers capacity to correct the wavefront.

4. The evaluation of the wavefront correction, in this work, was done through the SR. The flux coupling efficiency should be analysed to assess the quality of the received signal.

5. The prediction models used in this thesis is based on the theoretical spatial covariance of atmospheric turbulence, under the frozen flow hypothesis. Although this simplification has great value, a method based on Monte Carlo simulation could provide deeper insights by quantifying the variability of the parameters and validating the robustness of the spatio-temporal statistical identification.

References

Anderson, Brian DO, and John B Moore. 2007. *Optimal control: linear quadratic methods.* Courier Corporation. (Cited on page 39).

Andrews, Larry C. 2019. *Field guide to atmospheric optics.* (Cited on page 13).

Andrews, Larry C, and Melissa K Beason. 2023. *Laser beam propagation in random media: new and advanced topics.* (Cited on page 13).

Assémat, François, Richard W Wilson, and Eric Gendron. 2006. "Method for simulating infinitely long and non stationary phase screens with optimized memory storage." *Optics express* 14 (3): 988–999. https://doi.org/10.1364/OE.14.000988. (Cited on pages 8, 19).

Babcock, Horace W. 1953. "The possibility of compensating astronomical seeing." *Publications of the Astronomical Society of the Pacific* 65 (386): 229–236. https://doi.org/10.1086/126606. (Cited on page 2).

Bera, Binoy, and Madhumita Das Sarkar. 2016. "Piezoelectric effect, piezotronics and piezophototronics: a review." *Imperial Journal of Interdisciplinary Research (IJIR)* 2 (11): 1407–1410. (Cited on page 29).

Bufton, Jack L. 1973. "Comparison of vertical profile turbulence structure with stellar observations." *Applied optics* 12 (8): 1785–1793. https://doi.org/10.1364/AO.12.001785. (Cited on page 16).

Cakaj, Shkelzen. 2021. "The parameters comparison of the "Starlink" LEO satellites constellation for different orbital shells." *Frontiers in Communications and Networks* 2:643095. https://doi.org/10.3389/frcmn.2021.643095. (Cited on page 34).

Canuet, Lucien, Nicolas Védrenne, Jean-Marc Conan, Cyril Petit, Geraldine Artaud, Angelique Rissons, and Jerome Lacan. 2017. "Statistical properties of single-mode fiber coupling of satellite-to-ground laser links partially corrected by adaptive optics." *Journal of the Optical Society of America A* 35 (1): 148–162. https://doi.org/10.1364/JOSAA.35.000148. (Cited on page 40).

Christou, Julian C., Benoit Neichelb, François Rigautb, Michael Sheehana, Richard M. McDermida, Gelys Tranchob, Chadwick Trujilloa, and Brian Walls. 2010. "ALTAIR performance and updates at Gemini North." In *Adaptive Optics Systems II, Proc. SPIE,* vol. 7736. https://doi.org/10.1117/12.856776. (Cited on page 51).

Conan, Jean-Marc, Cyril Petit, Pablo Robles, and Perrine Lognoné. 2023. "Turbulence Temporal Prediction Performance Assessment for Adaptive Optics: Application to Observation of, and Space–Ground Optical Links with, LEO Satellites." Manuscript in preparation, 2023. (Cited on page 47).

Conan, R., and C. Correia. 2014. "Object-Oriented Matlab Adaptive Optics Toolbox (OOMAO)." In *Proceedings of the SPIE, Adaptive Optics Systems IV,* 9148:91486C. SPIE. https://doi.org/10.1117/12.2054470. (Cited on pages 3, 50).

Cyril, Petit, Bonnefois Aurélie, Conan Jean-Marc, Durecu Anne, Gustave François, Lim Caroline, Montri Joseph, et al. 2022. "FEELINGS: The ONERA's optical ground station for Geo Feeder links demonstration." In *2022 IEEE International Conference on Space Optical Systems and Applications (ICSOS),* 255–260. Kyoto City, Japan: IEEE. https://doi.org/10.1109/ICSOS53063.2022.9749705. (Cited on pages 4, 6, 11, 51).

Dam, Marcos A. van, David Le Mignant, and Bruce A. Macintosh. 2004. "Performance of the Keck Observatory adaptive-optics system." *Applied Optics* 43 (29): 5458–5470. https://doi.org/10.1364/AO.43.005458. (Cited on page 51).

De Karman, Theodore, and Leslie Howarth. 1938. "On the statistical theory of isotropic turbulence." *Proceedings of the Royal Society of London. Series A-Mathematical and Physical Sciences* 164 (917): 192–215. https://doi.org/Onthestatisticaltheoryofisotropicturbu-lence. (Cited on page 8).

Dessenne, Caroline, Pierre-Yves Madec, and Gérard Rousset. 1998. "Optimization of a predictive controller for closed-loop adaptive optics." *Appl. Opt.* 37, no. 21 (July): 4623–4633. https://doi.org/10.1364/AO.37.004623. (Cited on pages 7, 36).

Dray, Jonathan, Baptiste Sinquin, Morgan Gray, Benoit Neichel, Cédric Taıssir Héritier, Carlos M Correia, Raissa Camelo, Jalo Nousiainen, Thierry Fusco, Cyril Petit, et al. 2024. "Comparison of predictive control laws in adaptive optics for free-space optical communications." In *Adaptive Optics Systems IX,* 13097:1862–1868. SPIE. https://doi.org/10.1117/12.3019728. (Cited on page 36).

ESA. 2025. *ESA wraps up 300-million-kilometre optical communication campaign.* https://www.esa.int/Enabling_Support/Operations/ESA_wraps_up_300-million-kilometre_optical_communication_campaign. (Cited on page 1).

European Space Agency (ESA). 2020. *Low Earth orbit,* March. https://www.esa.int/ESA_Multimedia/Images/2020/03/Low_Earth_orbit. (Cited on page 35).

Fried, David L. 1982. "Anisoplanatism in adaptive optics." *Journal of the Optical Society of America* 72 (1): 52–61. https://doi.org/10.1364/JOSA.72.000052. (Cited on page 14).

Gendron, Eric, and Pierre Lena. 1994. "Astronomical adaptive optics. 1: Modal control optimization." *Astronomy and Astrophysics* 291:337–347. (Cited on pages 36, 49).

Giggenbach, Dirk, Christian Fuchs, Christopher Schmidt, Benjamin Rödiger, Steffen Gaißer, Sabine Klinkner, Duy-Ha Phung, et al. 2022. "Downlink communication experiments with OSIRISv1 laser terminal onboard Flying Laptop satellite." *Applied Optics* 61:1938–1946. https://doi.org/10.1364/AO.446771. (Cited on pages 4, 11, 51).

Goncalves Teixeira, Mafalda, Julio Ramirez Molina, and Vasco NGJ Soares. 2021. "Review on free-space optical communications for delay and disruption tolerant networks." *Electronics* 10 (13): 1607. https://doi.org/10.3390/electronics10131607. (Cited on page 9).

Gracheva, ME, and AS Gurvich. 1965. "Strong fluctuations in the intensity of light propagated through the atmosphere close to the earth." *Soviet Radiophysics* 8 (4): 511–515. (Cited on page 23).

Herrmann, Jan. 1992. “Phase variance and Strehl ratio in adaptive optics.” *Journal of the Optical Society of America A* 9 (12): 2257–2258. https://doi.org/10.1364/JOSAA.9.002257. (Cited on page 40).

Jackson, Kate, Carlos Correia, Olivier Lardière, Dave Andersen, and Colin Bradley. 2015. “Linear prediction of atmospheric wave-fronts for tomographic adaptive optics systems: modelling and robustness assessment.” *Optics letters* 40 (2): 143–146. https://doi.org/10.1364/OL.40.000143. (Cited on pages 22, 41, 42, 47, 48, 49).

Jahid, Abu, Mohammed H Alsharif, and Trevor J Hall. 2022. “A contemporary survey on free space optical communication: Potentials, technical challenges, recent advances and research direction.” *Journal of network and computer applications* 200:103311. https://doi.org/10.1016/j.jnca.2021.103311. (Cited on page 9).

Jasim, Sara Usama, and Raaid Nawfee Hassan. 2023. “Investigation of numerical simulation for adaptive optics system.” *Iraqi Journal of Physics* 21 (3): 9–23. https://doi.org/10.30723/ijp.v21i3.1122. (Cited on page 34).

Jiang, Ruixian, Kexin Wang, Xinke Tang, and Xu Wang. 2023. “Investigation of Oceanic Turbulence Random Phase Screen Generation Methods for UWOC.” *Photonics* 10 (7). ISSN: 2304-6732. https://doi.org/10.3390/photonics10070832. (Cited on page 15).

Jovanovic, N, Frantz Martinache, Olivier Guyon, Christophe Clergeon, Garima Singh, Tomoyuki Kudo, Vincent Garrel, Kevin Newman, D Doughty, Julien Lozi, et al. 2015. “The Subaru coronagraphic extreme adaptive optics system: enabling high-contrast imaging on solar-system scales.” *Publications of the Astronomical Society of the Pacific* 127 (955): 890. https://doi.org/10.1086/682989. (Cited on page 51).

Kaushal, Hemani, V.K. Jain, and Subrat Kar. 2017. *Free Space Optical Communication.* Springer India. (Cited on pages 1, 7, 10).

Kaushal, Hemani, and Georges Kaddoum. 2015. “Free space optical communication: challenges and mitigation techniques.” *arXiv preprint arXiv:1506.04836,* https://doi.org/10.48550/arXiv.1506.04836. (Cited on page 6).

Kolmogorov, Andrei Nikolaevich. 1991. “The local structure of turbulence in incompressible viscous fluid for very large Reynolds numbers.” *Proceedings of the Royal Society of London. Series A: Mathematical and Physical Sciences* 434 (1890): 9–13. https://doi.org/10.1098/rspa.1991.0075. (Cited on pages 8, 12).

Kulcsár, Caroline, Henri-François Raynaud, Cyril Petit, and Jean-Marc Conan. 2012. “Minimum variance prediction and control for adaptive optics.” *automatica* 48 (9): 1939–1954. https://doi.org/10.1016/j.automatica.2012.03.030. (Cited on page 40).

Kulcsár, Caroline, Henri-François Raynaud, Cyril Petit, Jean-Marc Conan, and Patrick Viaris de Lesegno. 2006. “Optimal control, observers and integrators in adaptive optics.” *Optics express* 14 (17): 7464–7476. https://doi.org/10.1364/OE.14.007464. (Cited on pages 36, 39, 40, 41).

Liu, Xuewen, Tim Morris, Chris Saunter, Francisco Javier de Cos Juez, Carlos González-Gutiérrez, and Lisa Bardou. 2020. “Wavefront prediction using artificial neural networks for open-loop adaptive optics.” *Monthly Notices of the Royal Astronomical Society* 496, no. 1 (June): 456–464. ISSN: 0035-8711. https://doi.org/10.1093/mnras/staa1558. (Cited on page 36).

Lütkepohl, Helmut. 2005. *New Introduction to Multiple Time Series Analysis.* Berlin, Heidelberg: Springer. ISBN: 978-3-540-40172-8. (Cited on page 45).

Minowa, Yosuke, Yutaka Hayano, Shin Oya, Makoto Watanabe, Masayuki Hattori, Olivier Guyon, Sebastian Egner, Yoshihiko Saito, Meguro Ito, Hideki Takami, et al. 2010. "Performance of Subaru adaptive optics system AO188." 7736:1302–1308. https://doi.org/10.1117/12.857818. (Cited on page 51).

NASA. 2023. *Optical Communications Overview.* https://www.nasa.gov/technology/space-comms/optical-communications-overview/. Accessed: 2025-09-04; Last updated: September 29, 2023. (Cited on page 1).

ONERA. 2024. *World premiere: ONERA establishes an adaptive-optics corrected laser link with the geostationary orbit on the 60 cm diameter full-aperture of the FEELINGS optical ground station.* https://www.onera.fr/en/press/world-premiere-onera-establishes-an-adaptive-optics-corrected-laser-link-with-the-geostationary-orbit-on-the-60cm-diameter-full-aperture-of-the-FEELING-optical-ground-station. Online; published 11 July 2024 :contentReference[oaicite:0]index=0, July. (Cited on pages 6, 36).

Paschall, Randall N, and David J Anderson. 1993. "Linear quadratic Gaussian control of a deformable mirror adaptive optics system with time-delayed measurements." *Applied optics* 32 (31): 6347–6358. https://doi.org/10.1364/AO.32.006347. (Cited on page 39).

Phung, Duy-Ha, Etienne Samain, Julien Chabé, Clement Courde, Nicolas Maurice, Hervé Mariey, Géraldine Artaud, Aziz Ziad, Christophe Giordano, Eric Aristidi, et al. 2021. "Optical bench development for laser communication OSIRIS mission at Grasse (France) station." In *International Conference on Space Optics—ICSO 2020,* 11852:981–994. SPIE. https://doi.org/10.1117/12.2599371. (Cited on pages 11, 51).

Platt, Ben C, and Roland Shack. 2001. *History and principles of Shack-Hartmann wavefront sensing,* 5. (Cited on pages 27, 28).

Ragazzoni, Roberto. 1996. "Pupil plane wavefront sensing with an oscillating prism." *Journal of modern optics* 43 (2): 289–293. https://doi.org/10.1080/09500349608232742. (Cited on page 29).

Robles, Pablo. 2023. "Optique adaptative pour la communication optique LEO-sol: Modélisation, optimisation et expérimentation." ED352: Physique et sciences de la matière. Laboratoire d'astrophysique de Marseille (LAM) en collaboration avec ONERA et CNES. Thèse de doctorat, Aix-Marseille Université, December. https://nuage.osupytheas.fr/s/ss2tzo2fSjXz5mA/download/RODRIGUEZ%20ROBLES23_OptiqueAdaptativeFSOC127772.pdf. (Cited on pages 2, 11, 16, 24, 35, 37, 41, 49).

Robles, Pablo, Cyril Petit, Jean-Marc Conan, Bouchra Benammar, and Benoit Neichel. 2022. "Predictive adaptive optics for satellite tracking applications: optical communications and satellite observation." In *Adaptive Optics Systems II, Proceedings of SPIE,* vol. 12185. https://doi.org/10.1117/12.2630217. (Cited on page 36).

Roddier, François. 1999. *Adaptive optics in astronomy.* Cambridge university press. (Cited on pages 26, 29).

Roggemann, Michael C, Byron M Welsh, Dennis Montera, and Troy A Rhoadarmer. 1995. "Method for simulating atmospheric turbulence phase effects for multiple time slices and anisoplanatic conditions." *Applied Optics* 34 (20): 4037–4051. https://doi.org/10.1364/AO.34.004037. (Cited on page 14).

Ross, T Sean. 2009. "Limitations and applicability of the Maréchal approximation." *Applied optics* 48 (10): 1812–1818. https://doi.org/10.1364/AO.48.001812. (Cited on page 33).

Simon, Dan. 2006. *Optimal state estimation: Kalman, H infinity, and nonlinear approaches.* John Wiley & Sons. (Cited on page 40).

Sivo, Gaetano, Caroline Kulcsár, Jean-Marc Conan, Henri-François Raynaud, Éric Gendron, Alastair Basden, Fabrice Vidal, Tim Morris, Serge Meimon, Cyril Petit, et al. 2014. "First on-sky SCAO validation of full LQG control with vibration mitigation on the CANARY pathfinder." *Optics express* 22 (19): 23565–23591. https://doi.org/10.1364/OE.22.023565. (Cited on pages 36, 39, 41).

Steinbock, Michael J. 2012. *Implementation of branch-point-tolerant wavefront reconstructor for strong turbulence compensation.* Technical report. (Cited on page 27).

Swanson, Robin, Masen Lamb, Carlos M Correia, Suresh Sivanandam, and Kiriakos Kutulakos. 2021. "Closed loop predictive control of adaptive optics systems with convolutional neural networks." *Monthly Notices of the Royal Astronomical Society* 503 (2): 2944–2954. https://doi.org/10.1093/mnras/stab632. (Cited on page 36).

Taylor, G. I. 1938. "The Spectrum of Turbulence." *Royal Society of London* A164476–490. https://doi.org/10.1098/rspa.1938.0032. (Cited on page 15).

Tyson, Robert K, and Benjamin West Frazier. 2022. *Principles of adaptive optics.* CRC press. (Cited on pages 22, 32, 33).

Wagner, Richard Edward, and Wilfred J Tomlinson. 1982. "Coupling efficiency of optics in single-mode fiber components." *Applied optics* 21 (15): 2671–2688. https://doi.org/10.1364/AO.21.002671. (Cited on page 34).

Walker, Gilbert Thomas. 1931. "On periodicity in series of related terms." *Proceedings of the Royal Society of London. Series A, Containing Papers of a Mathematical and Physical Character* 131 (818): 518–532. https://doi.org/10.1098/rspa.1931.0069. (Cited on page 46).

Wlodarczyk, Krystian, Emma Bryce, Noah Schwartz, Mel Strachan, David Hutson, Robert Maier, David Atkinson, et al. 2014. "Scalable stacked array piezoelectric deformable mirror for astronomy and laser processing applications." *The Review of scientific instruments* 85 (February): 024502. https://doi.org/10.1063/1.4865125. (Cited on page 29).

Yule, George Udny. 1927. "VII. On a method of investigating periodicities disturbed series, with special reference to Wolfer's sunspot numbers." *Philosophical Transactions of the Royal Society of London. Series A, Containing Papers of a Mathematical or Physical Character* 226 (636-646): 267–298. https://doi.org/10.1098/rsta.1927.0007. (Cited on page 46).

Appendix A

Derivation of the Temporal lag Error for AR Models

This appendix presents a detailed derivation of the temporal structure function for first- and second-order AR or VAR models, including all linear algebra steps, transposes, and the role of the wavefront reconstruction operator H_θ.

A.1 Definition of Temporal Lag Error

The temporal structure function is defined as the expected squared error between the true phase and its prediction:

$$D_t(\tau) \triangleq \sigma^2(\tau) = \left\langle \|H_\theta(\phi_{k+1} - \hat{\phi}_{k+1})\|^2 \right\rangle, \tag{A.1}$$

where $\hat{\phi}_{k+1}$ is the predicted phase at step $k+1$ and H_θ is the wavefront reconstruction operator.

The squared norm of a vector $\mathbf{x}$ is:

$$\|\mathbf{x}\|^2 = \mathbf{x}^\top \mathbf{x}, \tag{A.2}$$

So, the expression can be written as:

$$\sigma^2(\tau) = \left\langle \left(H_\theta(\phi_{k+1} - \hat{\phi}_{k+1})\right)^\top \left(H_\theta(\phi_{k+1} - \hat{\phi}_{k+1})\right) \right\rangle. \tag{A.3}$$

The transpose of a matrix product $(AB)^\top$ is equal to the product of the transposes in reverse order, $B^\top A^\top$. The temporal lag error can be simplified to:

$$\sigma^2(\tau) = \left\langle (\phi_{k+1} - \hat{\phi}_{k+1})^\top H_\theta^\top H_\theta (\phi_{k+1} - \hat{\phi}_{k+1}) \right\rangle \tag{A.4}$$

For any vector x and matrix M, $x^\top M x = \text{trace}\{x x^\top M\}$, here $x = (\phi_{k+1} - \hat{\phi}_{k+1})$ and $M = H_\theta^\top H_\theta$

$$\begin{aligned} \sigma^2(\tau) &= \left\langle (\phi_{k+1} - \hat{\phi}_{k+1})^\top H_\theta^\top H_\theta (\phi_{k+1} - \hat{\phi}_{k+1}) \right\rangle \\ &= \text{trace}\left\{ \left\langle (\phi_{k+1} - \hat{\phi}_{k+1})(\phi_{k+1} - \hat{\phi}_{k+1})^\top \right\rangle H_\theta^\top H_\theta \right\} \end{aligned} \tag{A.5}$$

Since $\mathrm{trace}(ABC) = \mathrm{trace}(CBA)$, the expression can be written as:

$$\sigma^2(\tau) = \mathrm{trace}\left\{ H_\theta \left\langle (\phi_{k+1} - \hat{\phi}_{k+1})(\phi_{k+1} - \hat{\phi}_{k+1})^\top \right\rangle H_\theta^\top \right\}. \tag{A.6}$$

Note: H_θ remains outside the expectation because it is a deterministic linear operator.

A.2 First Order Models: AR(1) and VAR(1)

For an AR(1) model:

$$\phi_{k+1} = A\phi_k + \varepsilon_k, \quad \langle \varepsilon_k \rangle = 0, \quad \left\langle \varepsilon_k \varepsilon_k^\top \right\rangle = \Sigma_\varepsilon, \tag{A.7}$$

setting $\hat{\phi}_{k+1} = A\phi_k$, one-step prediction. Then:

$$\phi_{k+1} - \hat{\phi}_{k+1} = \varepsilon_k. \tag{A.8}$$

The covariance of the prediction error is:

$$\left\langle (\phi_{k+1} - \hat{\phi}_{k+1})(\phi_{k+1} - \hat{\phi}_{k+1})^\top \right\rangle = \left\langle \varepsilon_k \varepsilon_k^\top \right\rangle = \Sigma_\varepsilon. \tag{A.9}$$

To obtain the structure function in terms of Σ_ϕ and Σ'_ϕ, let's expand the equation assuming symetry:

$$\begin{aligned}
\Sigma_\varepsilon &= \left\langle (\phi_{k+1} - A\phi_k)(\phi_{k+1} - A\phi_k)^\top \right\rangle = \left\langle (\phi_{k+1} - A\phi_k)(\phi_{k+1}^\top - \phi_k^\top A^\top) \right\rangle \\
&= \left\langle \phi_{k+1}\phi_{k+1}^\top - \phi_{k+1}\phi_k^\top A^\top - A\phi_k\phi_{k+1}^\top + A\phi_k\phi_k^\top A^\top \right\rangle \\
&= \Sigma_\phi + A\Sigma_\phi A^\top - \Sigma'_\phi A^\top - A\Sigma_\phi'^\top \\
&= \Sigma_\phi + A\Sigma_\phi A^\top - 2\Sigma'_\phi A^\top
\end{aligned} \tag{A.10}$$

where $\Sigma_\phi = \langle \phi_k \phi_k^\top \rangle$, $\Sigma'_\phi = \langle \phi_{k+1}\phi_k^\top \rangle$, and $-\Sigma'_\phi A^\top - A(\Sigma'_\phi)^\top \approx -2\Sigma'_\phi A^\top$ its assumed.

The same is applicable to VAR(1) models.

The temporal lag error of a first-order model can be written as:

$$\sigma^2(\tau) = \mathrm{trace}\left\{ H_\theta \left(\Sigma_\phi + A\Sigma_\phi A^\top - 2\Sigma'_\phi A^\top \right) H_\theta^\top \right\} \tag{A.11}$$

A.3 Second Order Models: AR(2) and VAR(2)

For an AR(2) model:

$$\phi_{k+1} = A\phi_k + B\phi_{k-1} + \varepsilon_k, \quad \langle \varepsilon_k \rangle = 0, \quad \left\langle \varepsilon_k \varepsilon_k^\top \right\rangle = \Sigma_\varepsilon, \tag{A.12}$$

setting $\hat{\phi}_{k+1} = A\phi_k + B\phi_{k-1}$ as the two-step prediction. Then:

$$\phi_{k+1} - \hat{\phi}_{k+1} = \varepsilon_k. \tag{A.13}$$

The covariance of the prediction error is:

$$\left\langle (\phi_{k+1} - \hat{\phi}_{k+1})(\phi_{k+1} - \hat{\phi}_{k+1})^\top \right\rangle = \left\langle \varepsilon_k \varepsilon_k^\top \right\rangle = \Sigma_\varepsilon. \tag{A.14}$$

To express the error in terms of Σ_ϕ, Σ'_ϕ, and Σ''_ϕ, expand:

$$\begin{aligned}
\Sigma_\varepsilon &= \left\langle (\phi_{k+1} - A\phi_k - B\phi_{k-1})(\phi_{k+1} - A\phi_k - B\phi_{k-1})^\top \right\rangle \\
&= \left\langle (\phi_{k+1} - A\phi_k - B\phi_{k-1})(\phi_{k+1}^\top - \phi_k^\top A^\top - \phi_{k-1}^\top B^\top) \right\rangle \\
&= \Big\langle \phi_{k+1}\phi_{k+1}^\top - \phi_{k+1}\phi_k^\top A^\top - \phi_{k+1}\phi_{k-1}^\top B^\top - A\phi_k\phi_{k+1}^\top + A\phi_k\phi_k^\top A^\top + A\phi_k\phi_{k-1}^\top B^\top \\
&\quad - B\phi_{k-1}\phi_{k+1}^\top + B\phi_{k-1}\phi_k^\top A^\top + B\phi_{k-1}\phi_{k-1}^\top B^\top \Big\rangle \\
&= \Sigma_\phi + A\Sigma_\phi A^\top + B\Sigma_\phi B^\top + 2A\Sigma'_\phi B^\top - 2A\Sigma'_\phi - 2B\Sigma''_\phi.
\end{aligned} \tag{A.15}$$

Here, $\Sigma_\phi = \langle \phi_k \phi_k^\top \rangle$, $\Sigma'_\phi = \langle \phi_{k+1}\phi_k^\top \rangle$, $\Sigma''_\phi = \langle \phi_{k+1}\phi_{k-1}^\top \rangle$, and the terms $-2A\Sigma'_\phi - 2B\Sigma''_\phi$ assume symmetry as usual.

The temporal lag error of a second-order model — AR or VAR — can be written as:

$$\sigma^2(\tau) = \text{trace}\left\{ H_\theta \left(\Sigma_\phi + A\Sigma_\phi A^\top + B\Sigma_\phi B^\top + 2A\Sigma'_\phi B^\top - 2(A\Sigma'_\phi - B\Sigma''_\phi) \right) H_\theta^\top \right\} \tag{A.16}$$

Appendix B

Derivation of the Temporal Lag Error for the Robustness Tests

This appendix presents a detailed derivation of the temporal lag error formulation of the various AR and VAR models for the robustness analysis of the predictive models to the atmospheric parameters, including the linear algebra steps.

Given the temporal lag error formulations, for a first- and second-order:

$$\begin{aligned}\sigma^2_{p=1}(\tau) &= \text{trace}\{H_\theta(\Sigma_\phi + A\Sigma_\phi A^\top - 2\Sigma'_\phi A^\top)H_\theta^\top\} \\ \sigma^2_{p=2}(\tau) &= \text{trace}\{H_\theta(\Sigma_\phi + A\Sigma_\phi A^\top + B\Sigma_\phi B^\top + 2A\Sigma'_\phi B^\top - 2(A\Sigma'_\phi - B\Sigma''_\phi)H_\theta^\top\}\end{aligned} \tag{B.1}$$

The predictive models estimate the matrices A and B of that formulation; thus, in this analysis, they are the ones to be susceptible to alterations.

B.1 Robustness to Wind Speed

To evaluate the sensitivity of the predictive models to variations in wind speed, we define a robustness factor k_v such that the actual wind speed is:

$$\|v\| = k_v \times \|v_0\| \tag{B.2}$$

where v_0 is the nominal wind speed.

The corresponding spatial displacements over a temporal lag τ are:

$$\Delta x = k_v \Delta x_0, \quad \Delta y = k_v \Delta y_0, \tag{B.3}$$

These displacements propagate into the assumed spatio-temporal covariance matrices Σ'_{ϕ,k_v}, Σ''_{ϕ,k_v}, while the instantaneous spatial covariance Σ_ϕ remains unchanged.

First-Order Model - VAR(1)

The coefficient matrix is computed as

$$A_{k_v} = \Sigma'_{\phi,k_v}\Sigma_{\phi}^{-1}, \tag{B.4}$$

and the covariance of the prediction error is

$$\Sigma_{\varepsilon,k_v} = \Sigma_{\phi} + A_{k_v}\Sigma_{\phi}A_{k_v}^{\top} - 2\Sigma'_{\phi}A_{k_v}^{\top}. \tag{B.5}$$

The temporal lag error is then

$$\sigma^2(k_v,\tau) = \frac{1}{N}\mathrm{trace}(\Sigma_{\varepsilon,k_v}). \tag{B.6}$$

For the uncorrected phase, $A_{k_v} = I$.

Second-Order Model - VAR(2)

The coefficient matrices are obtained as

$$\begin{bmatrix} A_{k_v} B_{k_v} \end{bmatrix} = \begin{bmatrix} \Sigma'_{\phi,k_v}\Sigma''_{\phi,k_v} \end{bmatrix} \begin{bmatrix} \Sigma_{\phi,k_v} & \Sigma'_{\phi,k_v} \\ \Sigma'^{\top}_{\phi,k_v} & \Sigma_{\phi,k_v} \end{bmatrix}^{-1} \tag{B.7}$$

The covariance of the prediction error is

$$\Sigma_{\varepsilon,k_v} = \Sigma_{\phi} + A_{k_v}\Sigma_{\phi}A_{k_v}^{\top} + B_{k_v}\Sigma_{\phi}B_{k_v}^{\top} + 2A_{k_v}\Sigma'_{\phi}B_{k_v}^{\top} - 2(A_{k_v}\Sigma'_{\phi} - B_{k_v}\Sigma''_{\phi}). \tag{B.8}$$

For the AR(2) Yule-Walker model, the matrices reduce to $A_{k_v} = \phi_1 I$ and $B_{k_v} = \phi_2 I$.

B.2 Robustness to Wind Direction

To evaluate the sensitivity of the predictive models to variations in wind direction, we define a robustness factor θ_ε such that the actual wind direction is

$$\theta = \theta_0 + \theta_\varepsilon \tag{B.9}$$

where θ_0 is the nominal wind direction.

The corresponding spatial displacements over a temporal lag τ are

$$\Delta x = \tau v \cos(\theta), \quad \Delta y = \tau v \sin(\theta), \tag{B.10}$$

with v being the wind speed. These displacements propagate into the assumed spatio-temporal covariance matrices $\Sigma'_{\phi,\theta_\varepsilon}$, $\Sigma''_{\phi,\theta_\varepsilon}$, while the instantaneous spatial covariance Σ_ϕ remains unchanged.

First-Order Model - VAR(1)

The coefficient matrix is computed as

$$A_{\theta_\varepsilon} = \Sigma'_{\phi,\theta_\varepsilon} \Sigma_\phi^{-1}, \tag{B.11}$$

and the covariance of the prediction error is

$$\Sigma_{\varepsilon,\theta_\varepsilon} = \Sigma_\phi + A_{\theta_\varepsilon}\Sigma_\phi A_{\theta_\varepsilon}^\top - 2\Sigma'_\phi A_{\theta_\varepsilon}^\top. \tag{B.12}$$

The temporal lag error is then

$$\sigma^2(\theta_\varepsilon, \tau) = \frac{1}{N}\mathrm{trace}(\Sigma_{\varepsilon,\theta_\varepsilon}). \tag{B.13}$$

For the uncorrected phase, $A_{\theta_\varepsilon} = I$.

Second-Order Model - VAR(2)

The coefficient matrices are obtained as

$$\begin{bmatrix} A_{\theta_\varepsilon} B_{\theta_\varepsilon} \end{bmatrix} = \begin{bmatrix} \Sigma'_{\phi,\theta_\varepsilon} \Sigma''_{\phi,\theta_\varepsilon} \end{bmatrix} \begin{bmatrix} \Sigma_{\phi,\theta_\varepsilon} & \Sigma'_{\phi,\theta_\varepsilon} \\ \Sigma'^{\top}_{\phi,\theta_\varepsilon} & \Sigma_{\phi,\theta_\varepsilon} \end{bmatrix}^{-1} \tag{B.14}$$

The covariance of the prediction error is

$$\Sigma_{\varepsilon,\theta_\varepsilon} = \Sigma_\phi + A_{\theta_\varepsilon}\Sigma_\phi A_{\theta_\varepsilon}^\top + B_{\theta_\varepsilon}\Sigma_\phi B_{\theta_\varepsilon}^\top + 2A_{\theta_\varepsilon}\Sigma'_\phi B_{\theta_\varepsilon}^\top - 2(A_{\theta_\varepsilon}\Sigma'_\phi - B_{\theta_\varepsilon}\Sigma''_\phi). \tag{B.15}$$

For the AR(2) Yule-Walker model, the matrices reduce to $A_{\theta_\varepsilon} = \phi_1 I$ and $B_{\theta_\varepsilon} = \phi_2 I$.

B.3 Robustness to Fried Parameter r_0

To assess sensitivity to atmospheric coherence length, we define a robustness factor k_{r_0} such that

$$r'_0 = k_{r_0} r_0 \tag{B.16}$$

The spatial displacements due to wind are unchanged; however, the covariance matrices must be recomputed for each perturbed r_0, they are assumed to be $\Sigma_{\phi,k_{r_0}}$, $\Sigma'_{\phi,k_{r_0}}$, and $\Sigma''_{\phi,k_{r_0}}$.

First-Order Model - VAR(1)

The coefficient matrix and prediction error covariance are

$$A_{k_{r_0}} = \Sigma'_{\phi,k_{r_0}} \Sigma_\phi^{-1}, \quad \Sigma_{\varepsilon,k_{r_0}} = \Sigma_\phi + A_{k_{r_0}}\Sigma_\phi A_{k_{r_0}}^\top - 2\Sigma'_\phi A_{k_{r_0}}^\top, \tag{B.17}$$

with temporal lag error

$$\sigma^2(k_{r_0},\tau) = \frac{1}{N}\mathrm{trace}(\Sigma_{\varepsilon,k_{r_0}}). \tag{B.18}$$

Second-Order Model - VAR(2)

The coefficient matrices are

$$\begin{bmatrix} A_{k_{r_0}} B_{k_{r_0}} \end{bmatrix} = \begin{bmatrix} \Sigma'_{\phi,k_{r_0}} \Sigma''_{\phi,k_{r_0}} \end{bmatrix} \begin{bmatrix} \Sigma_{\phi,k_{r_0}} & \Sigma'_{\phi,k_{r_0}} \\ \Sigma'^{\top}_{\phi,k_{r_0}} & \Sigma_{\phi,k_{r_0}} \end{bmatrix}^{-1} \tag{B.19}$$

with error covariance

$$\Sigma_{\varepsilon,k_{r_0}} = \Sigma_\phi + A_{k_{r_0}}\Sigma_\phi A^\top_{k_{r_0}} + B_{k_{r_0}}\Sigma_\phi B^\top_{k_{r_0}} + 2A_{k_{r_0}}\Sigma'_\phi B^\top_{k_{r_0}} - 2(A_{k_{r_0}}\Sigma'_\phi - B_{k_{r_0}}\Sigma''_\phi). \tag{B.20}$$

For AR(2) Yule-Walker, $A_{k_{r_0}} = \phi_1 I$ and $B_{k_{r_0}} = \phi_2 I$.